UNIVERSIDADE FEDERAL DE PERNAMBUCO
Centro de Ciências Exatas e da Natureza
Departamento de Química Fundamental
Programa de Pós-Graduação em Química

Tese de Doutorado

Computational Investigations of Reactivity and Selectivity of Methylation of Nitronates $[R^1R^2CNO_2]^-$

Ayyaz Mahmood

Recife-PE

2015

Ayyaz Mahmood*

Computational Investigations of Reactivity and Selectivity of Methylation of Nitronates $[R^1R^2CNO_2]^-$

Tese apresentada ao Programa de Pós-Graduação em Química da UFPE, como parte dos requisitos para a obtenção do título de Doutor em Química.

Área de concentração: Físico-Química

Supervisor:

Prof. Dr. Ricardo Luiz Longo

*CNPq Fellow

Recife-PE

2015

AYYAZ MAHMOOD

Computacional Investigations of Reactivity and Selectivity of

Methylation of Nitronates $[R^1R^2CNO_2]^-$

Tese apresentada ao Programa de Pós-Graduação no Departamento de Química Fundamental da Universidade Federal de Pernambuco, como requisito parcial para a obtenção do título de Doutor em Química.

Aprovado em: 27/11/2015

BANCA EXAMINADORA

Prof. Ricardo Luiz Longo (Orientador)
Departamento de Química Fundamental
Universidade Federal de Pernambuco

Prof. Gustavo de Miranda Seabra
Departamento de Química Fundamental
Universidade Federal de Pernambuco

Prof. Rogério Custodio
Instituto de Química
Universidade Estadual de Campinas

Prof. Paulo Henrique Menezes da Silva
Departamento de Química Fundamental
Universidade Federal de Pernambuco

Prof. Silmar Andrade do Monte
Departamento de Química
Universidade Federal da Paraíba

Dedicated to all those, who have realized and appreciated the pleasure of transmitting human knowledge.

Acknowledgements

I witness my urge to acquire knowledge of heaven and earth and all between them. I witness the existence of my creator who created me and made me the best creation. I thank my Allah who bestowed upon me, his blessings, the strength, peace of mind, good health, and competence that made me able to enable wisdom to ponder into diversity of knowledge.

I express my profound and cordial gratitude to my kind supervisor Prof. Ricardo Luiz Longo, who always finds time to listen little problems and to teach me insights and answer my questions. He is always a source of encouragement and inspiration since my first day at UFPE. I consider myself very fortunate for having the opportunity to work and learn great lessons with him. I am obliged to him for his dynamic supervision during the course of my research work. My special thanks to Dr. Erico Souza Teixeira for his helpful and problem solving discussions.

I am thankful to Prof. Ivani Malvestiti, for her valuable help to get me settled here and for her support, encouragement and guidance whenever I needed.

I owe my special regards and heartiest gratitude and cordial prays to my affectionate parents and grandparents who made great devotion to my studies and waited for me all this time. I cannot forget their sacrifices for me. Without their prayers, kindness, everlasting love, guidance and encouragement it would have been just a dream to complete this ambitious work. My brothers and my dear sisters are always a source of inspiration to me. I am extremely thankful to them for their full support, everlasting love, encouragement and sincere prayers for my success.

Finally special acknowledgement to the dynamic personalities for me: my fiancée Edna Barboza, my research fellows; Dr. Marcus Vinicius, Dr. Juliana Angeiras, Dr. Renaldo Júnior, Diego de Paula, Maria Carolina, Yaicel Proenza, Diego Raposo, my friends; Dartagnan Pires, Cristiane Kelly Oliveira, Thiago Muniz and my colleagues whole-heartedly.

Ayyaz Mahmood

بسم الله الرحمن الرحيم

IN THE NAME OF ALLAH

THE MOST GRACIOUS

THE MOST MERCIFUL

Abstract

We performed a mechanistic, selectivity and regioselectivity study of methylation of nitronates $[R^1R^2CNO_2]^-$ by CH_3I in the gas-phase, where $R^1 = R^2 = H$ (**1**), $R^1 = CH_3$ and $R^2 = H$ (**2**), $R^1 = R^2 = CH_3$ (**3**); and $R^1 + R^2 = c\text{-}(CH_2)_2$ (**4**), using *ab initio* MP2/CBS method, ADO and RRKM theories and kinetics simulations. The structures of all stationary points, including transition states, were successfully obtained to provide energies of activation ($\Delta^{\ddagger}E$) and of reaction ($\Delta_r E$) for all reaction pathways. These reactions proceed with the formation of ion-neutral reactant complex (RC@C or RC@O) that is converted into the respective product complex (PC@C and PC@O) through the corresponding transition state (TS@C and TS@O). The rate constants for the conversion of RCs into PCs were calculated with the RRKM theory. Contrary to a previous proposal for the reaction mechanism, the C-methylation is the thermodynamics and kinetics preferred pathway with the following PC@C:PC@O selectivites 89:11 (**1**), 97:03 (**2**-*E*), 97:03 (**2**-*Z*), 100:0 (**3**), and 100:0 (**4**). This is corroborated by the agreement between the calculated and experimental reactivity trend **4** >> **3** > **2** > **1**. The regioselectivity towards the C-alkylation is explained by the much larger exothermicity of this reaction channel compared to the O-alkylation. The increase of reactivity upon the increase of crowdedness of the central carbon atom is explained by differences of sp^3 character at this atom and the decrease of the vibrational frequency associated with pyramidalization around this carbon atom. An assessment of hybrid-DFT functionals and MP2 method for these reactions was performed in order to ascertain the reliability of these methods for similar molecular modeling. The most accurate and robust methods, with the least computational demand, were M06-2X and MP2 with aug-cc-pVTZ-PP basis sets.

In order to reveal the solvent and alkylating agent effects, the methylation reaction $[MeCHNO_2]^-$ (**2**) + Me_3O^+ (oxonium) was studied in the gas-phase and in solution with B2PLYP/6-311+G(d,p) calculations. The results show regioselectivity towards O-methylation in the gas-phase and more significantly in solution (dichloromethane), which is in agreement with the experimental observation. In addition, it shows that the regioselectivity is highly dependent upon the reactivity of the alkylating agent (MeI *vs.* Me_3O^+). This same method was employed for the $[XC_6H_4CHNO_2]^-$ + MeCl (X = H, *p*-MeO, *p*-NO_2) reactions in the gas-phase and in solution (DMF). The results in solution show a slight regioselectivity towards O-methylation; however,

considering that the methylating reagent used in the experiments was methyl *p*-bromobenzenesulfonate (MeOBS), which is much more reactive than MeCl, it should thus be expected an increase of the calculated selectivity.

Keywords: *Nitronates. Mechanism. RRKM theory. S_N2. Hybrid-DFT. Intrinsic reactivity. Solvent effects. Selectivity.*

Estudos Computacionais da Reatividade e Seletividade da Metilação de Nitronatos [R^{1}R^{2}CNO$_2$]$^-$

Resumo

Realizamos estudos do mecanismo, da seletividade e regiosseletividade da metilação de nitronatos [R^{1}R^{2}CNO$_2$]$^-$ com CH$_3$I, em que R^1 = R^2 = H (**1**), R^1 = CH$_3$ e R^2 = H (**2**), R^1 = R^2 = CH$_3$ (**3**); e R^1 + R^2 = c-(CH$_2$)$_2$ (**4**), usando método quântico *ab initio* MP2/CBS método e as teorias ADO e RRKM e simulações numéricas. As estruturas de todos os pontos estacionário no perfil da reação, incluindo os estados de transição, foram obtidas com sucesso e forneceram as energias de ativação ($\Delta^\ddagger E$) e de reacção ($\Delta_r E$) para todos os caminhos reacionais. Estas reações iniciam com a formação de complexo de reagente do tipo íon-molécula (RC@C ou RC@O) que se converte no respectivo complexo de produto (PC@C e PC@O), através do estado de transição (TS@C e TS@O) correspondente. As constantes de velocidade para a conversão do RC ao PC foram calculadas com a teoria RRKM. Ao contrário da proposta da literatura para o mecanismo de reação, a C-metilação é a via termodinâmica e cinética preferencial, com as seguintes seletividades: PC@C:PC@O = 89:11 (**1**), 97:03 (**2**-*E*), 97:03 (**2**-*Z*), 100:0 (**3**) e 100:0 (**4**). Isto é corroborado pela concordância qualitativa e quantitativa entre a ordem da reatividade calculada e experimental: **4** $\gg$ **3** > **2** > **1**. A regiosseletividade para a C-alquilação é explicada pela maior exotermicidade desse canal de reação em comparação com a O-alquilação. O aumento da reatividade com o aumento do impedimento estérico ao redor do carbono central é explicado pelas diferenças de carácter sp^3 deste átomo e pela diminuição da frequência vibracional associada à piramidalização ao redor deste átomo de carbono. Uma avaliação de funcionais híbridos- e duplo-híbrido DFT e do método MP2 para estas reações foi realizada a fim de verificar a confiabilidade e precisão destes métodos e sua utilização em modelagens similares. Os métodos mais precisos e robustos, que apresentam menor demanda computacional, foram M06-2X and MP2 com as funções de base aug-cc-pVTZ-PP.

A fim de revelar os efeitos solvente e do agente alquilante, a metilação do nitronato [MeCHNO$_2$]$^-$ (**2**) com Me$_3$O$^+$ (oxônio) foi estudada em fase gás e em solução com o método B2PLYP/6-311+G(d,p). Os resultados mostraram regiosseletividade para a O-metilação em fase gás e principalmente em solução (diclorometano), o que concorda com os dados experimentais.

Além disso, eles mostram que a regiosseletividade é fortemente dependente do agente alquilante (MeI *vs*. Me_3O^+). Este mesmo método foi utilizado para as reações $[XC_6H_4CHNO_2]^- + MeCl$ (X = H, *p*-MeO, *p*-NO$_2$) em fase gás e em solução (DMF). Os resultados em solução mostram uma pequena seletividade favorável à O-metilação, contudo, considerando que o agente metilante usado experimentalmente era o metil-*p*-bromobenzenossulfonato (MeOBS), o qual é muito mais reativo que o MeCl, é esperado que a utilização do MeOBS nas modelagens moleculares deva aumentar esta regiosseletividade para a O-metilação.

Palavras-chave: Nitronates. Mecanismo de reação. Teoria RRKM. S_N2. Híbrido-DFT. Reatividade intrínseca. Efeitos do solvente. Eeletividade.

List of Abbreviation

α	Polarizability
Å	Ångström (10^{-10} m)
A*	Energized molecule
$A^{\ddagger}$	Activated molecule
ADO	Average dipole orientation
CBS	Complete basis set
$\Delta^{\ddagger}E$	Energy of activation
$\Delta^{\ddagger}H$	Enthalpy of reaction
$\Delta^{\ddagger}S$	Entropy of reaction
$\Delta_r E$	Energy of reaction
DFT	Density functional theory
$E_r^{\ddagger}$	Rotational energy of the activated complex
$G^{\ddagger}(E - E_0)$	Sum of the states in the transition state at energy $E - E_0$
h	Planck constant
H	Hamiltonian
IRC	Intrinsic reaction coordinate
IVR	Intramolecular vibrational energy redistribution
k	Rate constant
$k^{\ddagger}$	Rate constant for the formation of activated complex
k_B	Boltzmann constant
m/e	Mass to charge ratio
MP2	Møller-Plesset perturbation theory through second order
μ	Reduced mass

$N(E)$	Density of state
$N^{\ddagger}(E)$	Density of states of the transition state
ν	Frequency
PC@C	Product complex at carbon
PC@O	Product complex at oxygen
PES	Potential energy surface
Q	Partition function
R	General gas constant
RC@C	Reactant complex at carbon
RC@O	Reactant complex at oxygen
RRK	Rice, Ramsperger and Kassel theory
RRKM	Rice, Ramsperger, Kassel and Marcus theory
S_N1	Unimolecular nucleophilic substitution
S_N2	Bimolecular nucleophilic substitution
TS@C	Transition state at carbon
TS@O	Transition state at oxygen
TST	Transition state theory
ZPE	Zero point energy
DMF	Dimethylformamide
DMSO	Dimethylsulfoxide
MeOBS	methyl *p*-bromobenzenesulfonate

Contents

« The underlying physical laws necessary for the mathematical theory of a large part of physics and the whole of chemistry are thus completely known, and the difficulty is only that the exact application of these laws leads to equations much too complicated to be soluble »

Dirac's quote (1929)

Chapter 1

Introduction

1.1 Introduction

The study of trends in chemical reactivity and its correlation with the molecular parameters is one of the fundamental goals of most chemists. An impressive amount of data has been accumulated over the years to provide the experimental support to the proposed mechanisms. On the other hand, theoretical methods have been developed to relate chemical reactivity and selectivity with molecular properties, which allows for the dynamic interplay between the theory and experiment.

The detailed study of mechanism of reactions is important because it can provide, for instance, insights, understanding and control of the chemical reactions. There are many reactions of commercial importance that can proceed through more than one pathway. Thus, the knowledge of the mechanism of a chemical reaction may help to choose appropriate reaction conditions to maximize the desired product and minimize by-products. Moreover, it sometimes makes possible to establish a correlation between the different systems involved in the chemical reaction based on information obtained from the study of reaction mechanism. Such correlation may help to discover new reactions and to unify and understand the processes that are difficult to correlate otherwise.

Moreover, most of the biochemical reactions in living systems involve the cleavage and formation of covalent bonds as well as electron transfer. The preparation of materials such as plastics, synthetics fibers, dyes and pharmaceutical agents also involve the cleavage and forming of covalent bonds. For chemists, it is, therefore, of great interest to have the understanding of such reactions. There are a number of techniques that can be used to study such reactions.

Ions are largely used as reactants, important intermediates and catalysts in organic reactions because of their reactivity. They have solvation energies often hundreds of kilo joules per mole, so the differences in the solvation energies of reactants, transition state and products can hinder the study of intrinsic reactivity. The rates and mechanisms of reactions are then influenced by the solvent medium and, because syntheses are performed in a solvent, theoretical modeling has to take these effects into account for a proper description. The ideal would, therefore, be to study

separated models (with and without the environment effects) of these reactions. In many aspects, the gas phase provides an ideal environment to study reactions because of possible stereocontrol and correlation to intrinsic reactivity. Thus, the study of ionic reactions in gas phase may provide insights about intrinsic reactivity and thereby expose the role of solvent. The study of intrinsic behavior is particularly important for the reactions involving ionic species because they have strong electrostatic interactions with the solvent.

Recent advances in the experimental techniques have provided results and insights into many ionic reactions in the gas-phase. The initial work of Bohme and co-workers [1–4] and by the group of Brauman [5–7] in the early 1970´s, showed large variations in the rates of nucleophilic substitution reactions. One direct method to study the collision dynamics is to observe the scattering of colliding particles. There are three basic techniques and variations that have been largely used to study the chemical dynamics of gas-phase reactions. They are: flowing afterglow [8, 9], Fourier transform ion cyclotron resonance (FT-ICR) [10–12] and static high pressure cells [13–15].

The essential feature of these techniques is that the amount of ions produced under (quasi-) vacuum is monitored as a function of time while changing the relative kinetic energy, temperature and other reaction parameters. The flowing afterglow can be used for a variety of reactants, including ions and neutral molecules, for which the rate constants can be calculated at thermal energies. Fourier transform ion cyclotron resonance is a mass spectrometric method in which the ions are detected according to their mass-to-charge (m/e) ratio in an applied uniform magnetic field. The m/e ratio is experimentally characterized as a frequency, so it can be measured more accurately than other experimental parameters. The FT-ICR method, therefore, offers higher resolution than other mass spectrometric methods.

The use of pulsed electron beam high-pressure mass spectrometer is another experimental technique known to operate in the Torr pressure range (<10 Torr) and at temperatures from -20–600 °C. The first experiment using this spectrometer had been reported by Arshadi et al. [16, 17]. In the recent years, the direct determination of gas-phase ion-neutral binding energies by measuring the critical energy of activation has become possible, for unimolecular dissociation

processes. The guided ion beam that has been developed to calculate the binding energies of transition metal complexes has recently been applied to anions [18]. Finally, the thermal infrared radiation is an interesting alternative to calculate the binding energies of weakly bonded atoms [19, 20].

On the other hand, molecular reaction dynamics (state-to-state chemistry) is very important and helpful to probe the reaction dynamics and reactivity. This provides detailed results and insights into chemical reactions and their stereodynamics. Usually, the complete interpretation of the results and mechanism requires computational modeling and preferably theoretical dynamics simulations. It is possible to study theoretically the molecular collision and obtain a detailed understanding of molecular interaction using quantum chemical computational methods. Chemical Dynamics is the study of mechanism of elementary chemical and physical processes at molecular level. It also deals with the quantum states of the reactants and the products. One tries to understand what actually happens at molecular level when a change, physical or chemical, takes place. As an example, when molecular chlorine gas reacts with bromine vapors, a chemical reaction takes place. The reaction is observed to show second order kinetics, that is, the rate of disappearance of Cl_2 and Br_2 is first order for each reactant. Yet, at the molecular level, the elementary reaction does not take place. The two molecules strike and bounce back of each other without exchanging the reacting atoms. This fact has been demonstrated experimentally [21]. Also, a simple collision may not be fruitful for a chemical reaction to occur, there comes other requirement which need to meet. The two reacting species need to collide in specific orientations (steric demand) and they have to collide with enough energy to rearrange (cleavage and formation) the chemical bonds. Chemical dynamics study explores such insight of the reaction.

A simple approach is to calculate the potential energy surface (PES), with the help of which rate constant and details of intermediates may be obtained. The PES is obtained by solving the time-independent Schrödinger equation using the Born-Oppenheimer approximation that separates the nuclear and electronic motions. The nuclear motion on the potential energy can then be described by either classical or quantum mechanics. The classical mechanics uses Newtonian mechanics to deal the equation of motion on PES giving a classical trajectory that describes the movement in space of the atoms being observed. A trajectory is a mathematical or diagrammatic description of

motion of a reacting system on the potential energy surface. Using different initial conditions (relative energies, orientations, etc.) many trajectories are generated, which can then be analyzed to provide details of the reactive encounters that convert the reactants into products. The quantum mechanics approach describes the motion of the nuclei by the time-dependent Schrödinger equation using mainly wave packets to simulate the nuclei and their interactions, including interferences. In both the cases, the objective is to establish a relationship between the microscopic properties and the macroscopic phenomena, that is, one of the major goals of chemical kinetics and dynamics.

Dynamics is frequently used for probing, understanding and controlling not only the neutral reagents and products but also the charged species (cations and anions), whether in bare state or solvated. It is also becoming relevant in the fields other than chemistry.

Another advantage of studying the reactions in the gas-phase is that they can be studied reliably using computational methods. Both ab initio and density functional theory (DFT) methods have been proved very useful for our understanding in this area of chemistry. For smaller systems, correlated ab initio quantum chemical methods have been proved to give very accurate results, close to that of experimental. For instance, the investigation of potential energy surfaces (PES) for a number of nucleophilic substitution reactions in the gas-phase have been the subject of many theoretical studies [22–26].

1.2 Mechanism of reactions: Macroscopic and microscopic kinetics

A reaction mechanism is the sequence of elementary processes that leads to the observed rate and explains how the overall reaction proceeds. An elementary reaction takes place in a single reactive encounter between the reactants involved. These elementary events cannot be further subdivided into processes of lesser complexity and they are the building blocks of any reaction. A reaction mechanism is therefore our best guess about the progress of reaction, that is, how a reaction proceeds. However, the fact that the mechanism agrees with the experimental results, is not a proof that the mechanism is correct. In addition to the observed reaction, the mechanism

has also to explain the selectivity, substituent, isotopic and solvent effects, amongst other kinetics properties.

An elementary reaction can be either unimolecular or bimolecular, because they are either collisional or decay processes, and only a few trimolecular reactions are known due to the vanishing probability of collisions between three or more bodies [27, 28]. For example, the reaction $2NO + X_2 \rightarrow 2NOX$, where $X = O_2$, Cl_2 and Br_2.

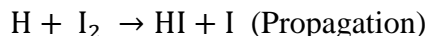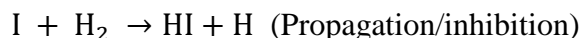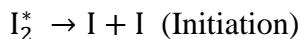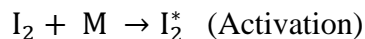Since the mechanism of a reaction involves elementary steps, it describes the transition states of each step, which are related to the regions around the saddle points in the potential energy surface. Reaction intermediates are stable species that do not appear in the experimental reaction rate because they are formed and consumed during the reaction. A mechanism must also account for the order as the bonds are broken and formed. The slowest step among all the elementary steps is the rate determining step because the reaction cannot proceed faster than the slowest step. Therefore, the slowest step establishes the overall rate of the reaction. The rate of the overall reaction is, therefore, the macroscopic kinetics study, while the description of a reaction at the elementary level, that is, as a sequence of elementary steps, is the microscopic kinetics or the dynamics of a reaction. Many reactions that are written as a single reaction equation actually consist of a series of elementary steps. As an example, let us take the reaction of hydrogen with iodine in the gas-phase:

$$H_2(g) + I_2(g) \rightarrow 2HI(g)$$
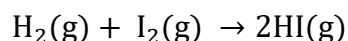
The reaction is known as second order giving the rate as $v = k[H_2][I_2]$. But the complexity underlying the above reaction is shown below as a sequence of elementary steps.

$$I_2 + M \rightarrow I_2^* \quad \text{(Activation)}$$

$$I_2^* \rightarrow I + I \quad \text{(Initiation)}$$

$$I + H_2 \rightarrow HI + H \quad \text{(Propagation/inhibition)}$$

$$H + I_2 \rightarrow HI + I \quad \text{(Propagation)}$$

where M is any gas-phase species or the recipient walls.

The reaction rate can be written in the form of rate of change of I concentration [I] or H concentration [H]. However, the rate law does not generally follow the overall reaction equation because the overall reaction equation is the net result (macroscopic description) of all the elementary reactions in the mechanism (microscopic description). Hence, the proper elementary steps (mechanism) should provide the observed rate law obtained, for instance, from the slowest step among all the elementary steps or from applying approximations such as steady-state as in the case presented above for the $H_2(g) + I_2(g) \rightarrow 2HI(g)$ reaction [29].

1.2.1 Order and molecularity of a reaction

Order of a reaction is the sum of the power coefficients (exponents) of concentration terms in the rate law. Because the rate law may be obtained from the slowest step in a series of elementary steps involved in the reaction mechanism or from approximations to the kinetic equations (e.g., steady-state), the order of a reaction can, therefore, only be determined by performing kinetics experiments. It cannot simply be deduced from the stoichiometric equation of the reaction, but we have to determine the dependence of the reaction rate on the concentration of each species involved in the reaction, including products, solvent and pH. As an example, the reaction between 2-bromo-2-methylpropane and hydroxide ions can be written as

$$(CH_3)_3CBr + OH^- \rightarrow (CH_3)_3COH + Br^-$$
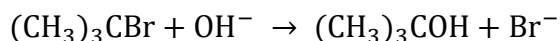
This is the overall reaction where the hydroxide ion replaces the bromine atom. However, at the molecular level, the reaction occurs in two steps. The first step is the dissociation of the C–Br bond to form a carbocation and bromide, followed by the second step that involves the addition of OH^- to the central carbon atom of the carbocation, as illustrated bellow:
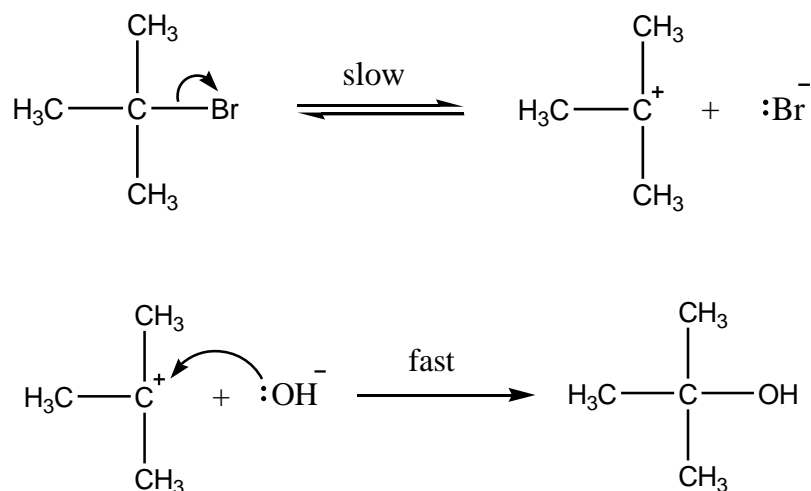
Indeed, the experiments show that the formation of the carbocation is the slowest step among the two steps. So the rate law for the above reaction can be written as

$$\text{rate} = k\,[(CH_3)_3CBr]$$

From the rate law, it can be seen that the reaction is first order with respect to the 2-bromo-2-methylpropane and zero order with respect to the hydroxide ion. This means the concentration of the hydroxide ion has no effect on the overall rate of the reaction. Although an increase in concentration of the hydroxide ions will speed up the second step of the reaction, the overall rate of the reaction will not be affected because it is governed by the first (slowest) step. However, if we decrease the concentration of the hydroxide ions to a point where both the steps have similar rates, then the concentration of the hydroxide ions becomes to affect the reaction rate.

Molecularity of the reaction is simply the number of species (molecules, atoms or ions) taking part in each elementary step. Thus, when writing the mechanism of a reaction as a sequence of elementary steps, each of the elementary steps has molecularity. In the above example, the first step of the reaction has a molecularity of 1, that is, unimolecular, because it involves only one species. While the second step involves two species so it has a molecularity of 2 and hence it is a bimolecular reaction.

Despite the large number of possible reactions and their mechanisms, they have been cleverly grouped into general patterns that can be used to describe many important reactions. We do not intend to include the details of each kind of reaction mechanism, rather shall continue with nucleophilic displacement (or substitution) reactions.

1.2.2 Nucleophilic substitution reactions

Nucleophilic substitution reactions have been first studied by Huges, Ingold and co-workers in 1930´s [30]. They discovered that some of the nucleophilic reactions are first order, that is, the rate depends only on the concentration of substrate and does not depend on the concentration of nucleophile, while in other reactions the rate depends on the concentration of both the substrate and nucleophile. Based on this, they proposed two common types of substitution reaction; substitutions that proceed by a bimolecular rate-determining step, denoted as S_N2 and those proceed by a unimolecular rate determining step, referred as S_N1. The main difference between these mechanisms is the timing associated with the bond formation of the nucleophile (a species with lone electron pair) and the bond cleaving of the leaving group (nucleofuge); in other words, the order in which these events occur during the reaction. In S_N2 reactions, the addition of nucleophile and the elimination of leaving group occur simultaneously, while S_N1 reactions involve two steps. In S_N1 reactions, the first step is the elimination of leaving group to form a stable carbocation, which then reacts with nucleophile to form the product. The formation of carbocation is the slowest and thus the rate-determining step. They generally show first order kinetics. The two mechanisms compete each other. S_N2 mechanism dominates where the central carbon atom is easily accessible for the nucleophilic attack. On the other hand, S_N1 reaction is preferred where the central carbon atom is attached to bulky groups. This is because the bulky groups sterically hinder the nucleophilic approach to the central carbon and provide stabilization of the carbocation.

Another difference between the two mechanisms is determined from the factors affecting the rate of two reactions. In S_N1 reaction, the rate depends on the carbon skeleton and the leaving group but not the nucleophile. This is because the departure of leaving group is the slowest step. For a

S_N1 mechanism, the leaving group must be good enough to depart easily to form the carbocation. After the formation of carbocation, the process of the nucleophilic attack is very fast so it is not the rate-determining. However, S_N2 reactions are influenced by the carbon skeleton, leaving group and the nucleophile. This is because the S_N2 reactions are concerted, that is, the attack of nucleophile and the departure of leaving group occur simultaneously in single step. Stereochemistry also makes a difference between the two reaction pathways: S_N2 reactions give inversion of configuration, if there exists a stereo-center, because it proceeds through backside attack while S_N1 reactions give a mixture of retention and inversion, because the nucleophile can attack from either side of the flat carbocation.

1.2.3 Bimolecular nucleophilic displacement reactions (S_N2 or A_ND_N)

Bimolecular nucleophilic substitution (S_N2) reactions have been one of the favorites of physical organic chemists for many years and they are one of the most widely studied families of reactions in chemistry. Bimolecular nucleophilic substitution (or displacement) reactions are one step process. This means the process whereby the attack of the nucleophile and the departure of the leaving group occur at the same time in a single step.

The only step involved in the S_N2 reactions must then be the rate determining step. S_N2 reactions are also named as associative substitutions. This terminology is used for the reactions of coordination and organometallic compounds, but they resemble the S_N2 mechanism in organic chemistry. Associative substitution describes a mechanism by which the compounds interchange the ligands. The opposite pathway is dissociative mechanism, analogous to S_N1 mechanism.
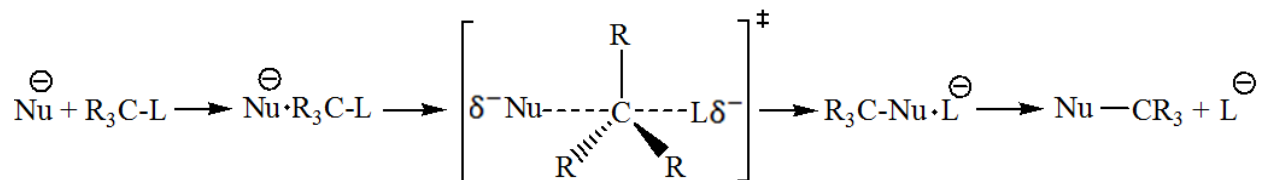
Scheme 1.1 An example of S_N2 reaction in the gas-phase.

An example of the S_N2 reaction in the gas-phase is shown in scheme 1.1. The reaction started with the initial formation of the reactant complex due the presence of ion-dipole interactions. The attack of the nucleophile (Nu^-) then occurs on the backside of substrate (R_3C-L) directly opposite to the leaving group (L^-). The resulting change in the configuration of the substrate can be described by the turning inside out of an umbrella. As the nucleophile approaches the substrate, the orbital that contain electron pair begins to overlap the empty anti-bonding orbital of carbon atom bearing the leaving group [31], so the new bond starts to form and the bonding character of the C–L orbital changes. The transition state structure resembles a (distorted) trigonal bipyramid with the substituents being in a trigonal plane perpendicular to the bonds being formed (Nu–C) and cleaved (C–L). This is called in-line mechanism, because the Nu–C–L species are (nearly) linear. Both the substrate and nucleophile are involved in the transition state, so S_N2 are bimolecular reactions and because they are elementary reactions their kinetics is second order, that is, the rate depends on the concentration of both the substrate and nucleophile species. The number of molecules involved in the reaction is the molecularity and the order of the reaction relates to the dependence of the rate of reaction.

To emphasize the relevance of experimental and computational dynamical studies, a new reaction pathway has been observed by Mikosch and co-workers for the S_N2 reaction $CH_3I + Cl^-$ in the gas-phase [32]. They mapped the product velocities from the collisions between crossed beams of methyl iodide with chloride ion to produce a bimolecular nucleophilic reaction. In this new mechanism observed at collision energies higher than 1.9 eV, called roundabout mechanism, the chloride ion strikes the methyl group and induces a rotation of methyl iodide by 360° before the iodide displacement occurs. This rotation scrambles the velocity vector of the outgoing product fragments that are measured and mapped. At lower collision energies, the traditional in-line S_N2 mechanism is observed. Drahl [33] reported a similar mechanism. They imaged the S_N2 reaction at different collision energies and observed that at higher collision energies, some iodide ions (leaving group) are found with much slower velocity. Because the energy and momenta are conserved and are guided by computational dynamics simulations these studies concluded that the energy missing from the iodide ions or the backward mapped velocity is due to methylchloride rotational excitation, which favors the proposed roundabout mechanism [32, 34].

More recently, this mechanism was observed for lighter atoms and thermal collision energies during the dynamical studies of the OH^- attack on CH_3ONO_2 substrate [35].

1.2.4 Steric and electronic effects

In S_N2 reactions, the nucleophile approaches the substrate carbon atom from the opposite side to the leaving group (backside attack), which results in the inversion of the configuration. This inversion through a (distorted) trigonal bipyramid structure (transition state) is highly sensitive to the size of the substituents attached to the reaction center. Bulky groups sterically hinder the approach of the nucleophile and interact strongly with the other groups, mainly the nucleophile and the leaving group, thus raising the energy barrier that slows the rate of the reaction. That is the main reason for the rate of S_N2 reactions proceeds from primary (fastest) > secondary >> tertiary (slowest). Likewise, the size and nature of nucleophile also affects the nucleophilic strength, for instance, methoxide anion is a strong nucleophile than a *tert*-butoxide ion. The strong nucleophiles tend to give higher reaction rates. The reaction of methoxide anion with methyl iodide gives a faster rate than the reaction of *tert*-butoxide ion with methyl iodide.

The nucleophilicity is affected by the electronic properties, such as, charge density and electronegativity. Nucleophilicity increases with the increase of negative charge and decrease of electronegativity. For example, in polar aprotic solvents, negatively charged OH^- is stronger nucleophile than neutral water and I^- is a better nucleophile than Br^- (I^- is less electronegative than Br^- and have bigger size as well). For the latter example, the solvent effects might have an important role because, usually, I^- is less solvated than Br^- so it can attack more easily the carbon center.

1.2.5 Dynamical features of gas-phase nucleophilic substitution reactions

While studying a reaction mechanism it is important to consider the energy requirements of the reactions. The energy differences (or relative energies) are key to understand the mechanism of reaction. Most of the relevant reactions are activated processes, i.e. processes in which the

reactants absorb energy (collisions, radiation) that is redistributed to convert them into a transition state (or activated complex). This activated complex then proceed to be converted into products without any further input of energy, rather with a release of energy that it has absorbed during the initial step of its formation. S_N2 reactions in the gas-phase are characterized by a double-well potential energy diagram. The reactants form a reactant ion-dipole complex that is a minimum in the energy profile and characterizes the first well. After the energy barrier, the ion-molecule also form a complex, called product complex, that generates the second well in the energy profile, prior to the dissociation into the products. The rate constant for the formation of these ion-dipole complexes can be calculated, for instance, by the parameterized Average Dipole Orientation (ADO) theory [36, 37]. This theory uses statistical methods for the calculation the average orientation of polar molecules in an ion field and then a Langevin procedure to determine the capture rate constant.

The formation of activated complex and its decomposition into products can be dealt by statistical theories such as transition state and RRKM. According to the transition state theory, the reaction rate increases exponentially as the Gibbs energy difference between the transition state and the reactants decreases. Indeed, this theory has been the workhorse of the chemical kinetics, mainly because of its simplicity and impressive results. For instance, it can rationalize and even predict selectivities, yields and catalytic effects on a wide range of bimolecular reactions. This theory is based on the assumption that the reaction follows the minimum energy pathway and that the states of the reactants and transition state are in (quasi-)equilibrium. Therefore, it is a statistical theory that uses limited information about the potential energy surface, namely, the reactants and transition state structures. For unimolecular reactions, the equivalent theory is the RRKM formulation, which together with the transition state theory forms the foundation to understand reaction mechanism and chemical kinetics of elementary reactions. The transition state and RRKM theories assume that the reaction coordinate can be separated from other degrees of freedom. For unimolecular reactions, it is assumed that the initially prepared state relaxes via intramolecular vibrational energy redistribution (IVR), which leads to equally probable internal degrees of freedom populations. Hence, it is the statistical assumption. Similarly, in the transition state theory the reactants and the activated complex are in equilibrium

and a (pseudo-)equilibrium constant can be invoked. From a dynamical point of view, this equilibrium assumption is equivalent to the no-recrossing assumption, that is, once the activated complex is reached it does not return (recross) to the reactants.

Applications of these theories led to the usual picture of chemical reactions represented in Figure 1.2 as energy profiles. The vertical axis is the free energy of the system and the horizontal axis represents the reaction coordinate. Both the starting and ending point of the curve are minima and represent reactants, intermediates, or products. In the case depicted in Figure 1.2, the reaction is exergonic as the Gibbs energy of the products is lower than that of reactants.
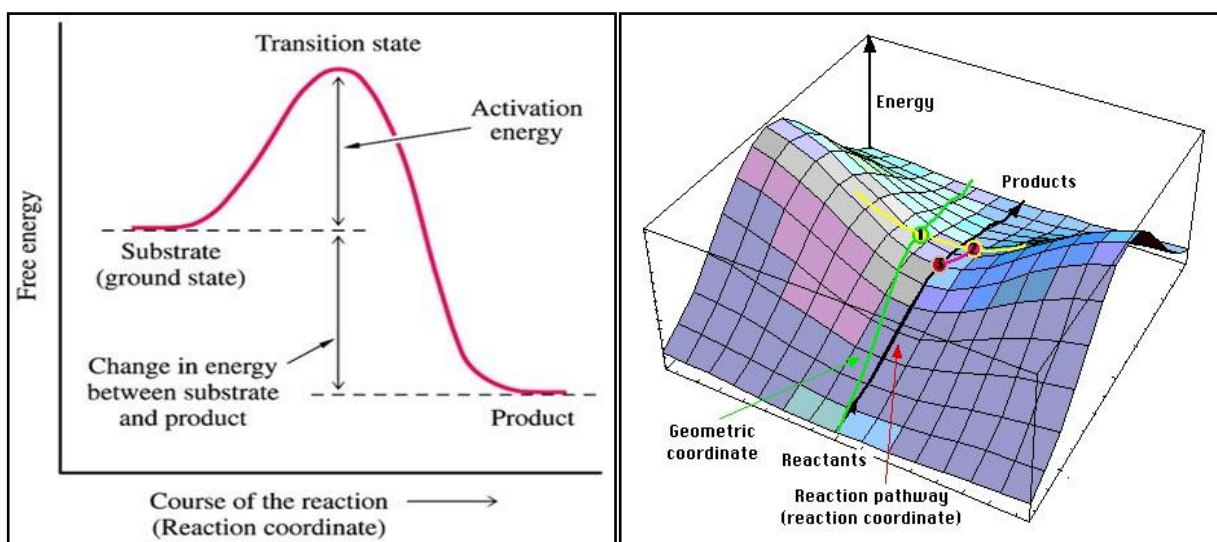
Figure 1.2 Reaction energy profile (left) and a three-dimensional representation of the potential energy surface (right).

Figure 1.1 Reaction energy profile (left) and a three-dimensional representation of the potential energy surface (right).

Each critical point on the potential energy surface is characterized by zero first-derivatives of the energy (or gradient) with respect to all (3N – 6) internal coordinates,

$$\frac{\partial E}{\partial R_i} = 0 \quad i = 1, 2, 3, \dots, 3N - 6$$

where E is the total energy and R_i is the i-th internal coordinate, so that critical points are also known as stationary points (on the potential energy surface). The chemical nature of a critical

point is obtained from the signs of the second derivatives of the energy with respect to all $(3N - 6)$ internal coordinates, namely, the Hessian matrix. For stable structures, such as, reactants, products and intermediates their corresponding stationary points on the potential energy surface have all positive second derivatives. Transition state structures or first-order saddle points are also critical points and are characterized by all but one positive second derivatives of the energy with respect to the coordinates. Higher-order saddle points, which have no chemical analog, have more than one negative second derivative. Another relevant concept when applying computational chemistry to elementary reactions is the intrinsic reaction coordinate (IRC), which is the minimum energy path that connects a given reactant (or intermediate) to a given product (or intermediate) through a corresponding transition structure. One of the main assumptions of the statistical theories is that the reaction should proceed along the IRC, which then defines the reaction path.

From the concepts of reaction energy profiles, critical points and IRC, many kinetics results can be explained and rationalized. The first step to rationalize these results is to define if the reaction is controlled by thermodynamics or by kinetics.

1.2.6 Thermodynamics control versus kinetics control

Some reactions provide a given distribution of products under a set of conditions, while they yield a different distribution of product upon changing the reaction conditions, that is, the pathways of the reactions are controlled by these conditions. This is because there are two kinds of factors that control the mechanism of the reactions: thermodynamics control and kinetics control. This also provides explanations for some reactions requiring heat for many hours, while others are performed in ice-cold or dry-ice temperature. This behavior can be explained by the unifying concept of reaction energy profiles.

Consider an example of a reaction, whose energy profile is show in Figure 1.3. The relative Gibbs energies (or Gibbs energy differences) are key to understand the mechanism of reaction.
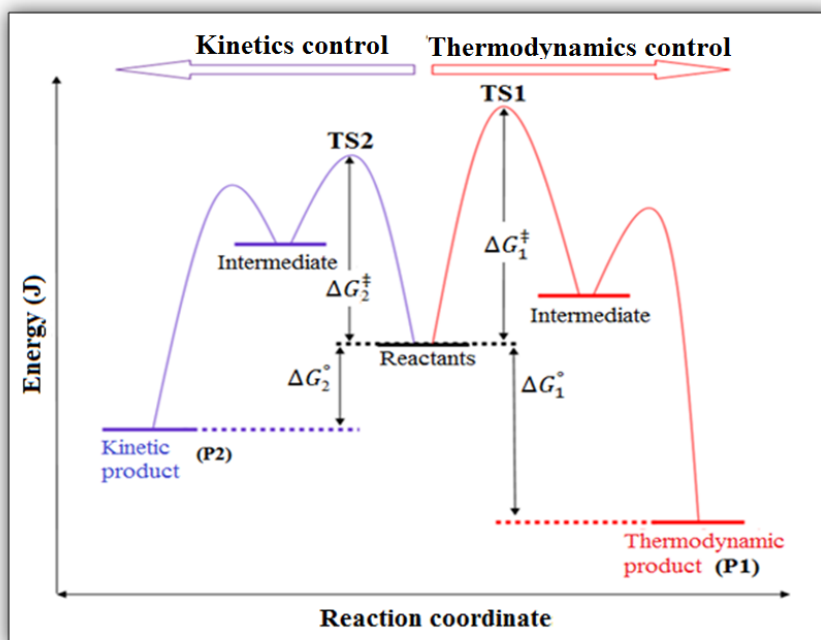
Figure 1.3 Gibbs energy diagram (or profile) representing the formation of thermodynamics or kinetics product.

In this example, the reaction can proceed via two pathways, giving two different products. By looking at the reaction coordinate, we would expect the left hand reaction to be favored kinetically, because $G_2^{\ddagger}$, the activation energy required to pass through TS2 is smaller than the activation energy $G_1^{\ddagger}$ required to pass through TS1. However, we know that thermodynamically more stable products tend to be formed in greater amounts so the product P1, which is thermodynamically more stable, will be formed in greater amount than P2. In this case, one product (P2) is favored kinetically, while other product (P1) is favored thermodynamically. In such a situation, the preferred reaction pathway will depend upon the reaction conditions, such as temperature, time, pressure, solvent, etc. For example, the kinetics product can be favored by short reaction times because the reaction has not reached chemical equilibrium. Alternatively, long reaction times favor the thermodynamically product P1 because the less stable P2 molecules have enough time to react again and go back all the way to the reactants and yield the more stable product P1.

The other way to bias the conditions is to lower the temperature because low temperatures offer little energy to P2 to return over TS2, passing through TS1 and eventually convert to P1. Low temperatures make the reversible reaction essentially negligible. To favor the thermodynamics product we use longer reaction times or higher temperatures. The idea is similar here, as the high temperature provides the great deal of energy to all the reactants and products, thus reactants can easily cross over energy barriers. Thus, overall equilibrium over both transition states leads automatically the kinetically favored molecules to the more stable thermodynamic product, given enough time. In general, reactions in gas-phase do not reach chemical equilibrium, so they are essentially controlled by the kinetics. Hence, the reaction rate theories become relevant to explain and predict reaction yields and selectivities in the gas-phase.

Despite the successes of both transition state and RRKM theories in treating uni- and bimolecular reactions, there have been reported several examples, in the last few years, where these statistical theories fail to properly describe the reactions, mostly in gas-phase. Some of these failures are related to:

1. Post-transition state bifurcation of the potential energy surface. A single transition state may lead to more than one product if there exists a path bifurcation after the transition state on the potential energy surface. On a two-dimensional potential energy surface, two transition states are apparently separated by a minima. However, this is not true in all the cases because linear molecules with N atoms have $3N - 5$ dimensions and on a multi-dimensional potential energy surface, the two transition states are not necessarily separated by a valley. Examples of such reaction involving bifurcation are isomerizations and rearrangements [38]. For instance, the addition of HF to ethane $H_2C=CH_2$ can yield two equivalent rotamers of fluroethane [39]. However, the question: what controls the product selectivity on a bifurcating PES, still remain largely unanswered. The answer to this question requires the experimental mechanistic studies, for instance, kinetics, kinetic isotopic effect, analysis of product scope etc., and computational methods, that is, molecular dynamics and electronic structure calculations. The topology study of the bifurcating PES may help to understand the product selectivity.

2. The mechanism is controlled by the dynamics, such as, conservation of momentum and long range electrostatic interactions. The distribution of products is determined by the ratio of

number of microscopic pathways in each direction and these pathways are influenced by the conservation of angular momentum [40] or the initial configurations of the reactants and their interactions. Long range interactions have also been observed to influence the selectivity of the products [35]

3. Non-statistical behavior [41]. The non-statistical behavior is observed when there is a bottleneck in the phase space that prevents the full microcanonical equilibrium and when the transition between different regions of phase space is less probable than the transition through the barrier. In other words, the dissociation is faster than the intramolecular vibrational energy redistribution (IVR). This is also called a non-RRKM behavior. Examples of non-RRKM behavior have been reported for some reactions [42, 43]. Another example of non-statistical behavior is related to recrossings through the dividing plane between reactants and products. For instance, in S_N2 reactions it has been shown that a single dynamics trajectory can recross many times before leading to the products [44]. For example, the S_N2 reaction $Cl^- + CH_3Cl$ presents a weak coupling between the CH_3Cl intramolecular mode and $Cl^-\cdots CH_3Cl$ (reactant complex) intermolecular modes causes the central barrier recrossing, resulting in the non-RRKM behavior of the $Cl^-\cdots CH_3Cl$ reactant complex [45]. Proton abstraction of the CH_3ONO_2 substrate by OH^- also presents several recrossings, that is, the proton is abstracted to form H_2O then it returns to the $[CH_2ONO_2]^-$ substrate and so on [35].

4. Reaction pathways that do not follow the intrinsic reaction coordinate (IRC). Most commonly it is observed that the reactants in their way to products follow a pathway of minimum energy that may involve reaction intermediates [46]. These intermediates reside in potential energy wells for a period of time long enough to redistribute the energy among the vibrational modes via IVR [47]. However, the case of $OH^- + CH_3F \rightarrow CH_3OH + F^-$ is quite different. The computational dynamics of the reaction shows a deep potential energy minimum on the product side corresponding to the $CH_3OH\cdots F^-$ product complex which have energy redistributed among its vibrational states [48–50]. However, out of the 31 trajectory calculations, 27 (90%) followed the path of direct dissociation of the transition state into the separated products and avoid the minimum on the potential energy surface [51]. Another example of reactions following non-IRC path is the reaction $F^- + CH_3OOH$. Much surprisingly, the reaction did not yield the most

exothermic products predicted by IRC, that is, $HF + CH_2(OH)O^-$, rather a higher energy non-IRC products $HF + CH_2O + OH^-$ are formed [52].

As a result, when applying quantum chemical methods to chemical kinetics it is important to verify if these statistical theories based on limited information of the potential energy surface are applicable. Usually this verification is performed by comparing the calculated results with the experimental data. In fact, this is the main goal of the present work, namely, to investigate the reaction mechanism of the nucleophilic displacement at iodomethane (CH_3I) by deprotonated nitroalkane $[R^1R^2CNO_2]^-$ (or nitronate) nucleophiles. In particular, this nucleophilic displacement can occur either through the carbon atom or through the oxygen atom, leading to different products: C-alkylation and O-alkylation.

The deprotonated nitroalkane (or nitronate) acts as a nucleophile to proceed with an S_N2 displacement of the iodide in CH_3I. On the other hand, the negative charge of nitronates $[R^1R^2CNO_2]^-$ may be delocalized at the oxygen atoms of the nitro group and at the central carbon atom. Thus, the S_N2 displacement may occur through the carbon atom ($S_N2@C$ pathway leading to C-alkylation) or either of the oxygen atoms ($S_N2@O$ pathway leading to O-alkylation) of the nitro group. In addition, for asymmetric nitronates, such as, $[CH_3CHNO_2]^-$, both *syn* and *anti* displacements are possible, leading to O-alkylation products with *E* and *Z* stereochemistry.

The calculated reaction profiles for $[R^1R^2CNO_2]^- + CH_3I$ have the usual double-well potential found in S_N2 reactions in the gas-phase. That is, the reactants form ion-dipole complexes (RC@C and RC@O) that yield the product complexes (PC@C and PC@O) passing through the corresponding transition states (TS@C and TS@O).

Interestingly, it has been observed experimentally that when the environment of the central carbon atom becomes more crowded the reaction rate increases. Thus, in order to understand this apparent contradiction, it is necessary to explore the critical points of the potential energy surface, to apply statistical theories, and to verify if they are able to explain the experimental observations. If they are not, then it might be necessary to perform dynamics studies to understand these reactions.

1.3 Methylation of Nitronates [R^{1}R^{2}CNO$_2$]$^-$ by CH$_3$I in the Gas-Phase

Deprotonation of nitroalkanes, R^{1}R^{2}CHNO$_2$, can be achieved in the gas-phase and in solution under mild and controlled conditions [53–56]. These generated anions, [R^{1}R^{2}CNO$_2$]$^-$ known as nitronates or azinates, are useful synthetic reactive intermediates because they can form C–C and/or C–O bonds [53–60]. For instance, the Henry (or nitro-aldol) reaction between nitronates and aldehydes or ketones is a classic carbon–carbon bond formation reaction [53–61]. Alkylations of nitronates are also quite useful reactions; however, the ambient nature of these anions [62] may lead to C-alkylation and O-alkylation [53–56, 61, 63]. Thus, determining the origin of the regioselectivity in alkylations of nitronates is important to broaden the scope of these reactions. For instance, only O-alkylated products were obtained in the reaction of ring-substituted phenylnitromethanes with MeOBs in several protic and aprotic solvents, where the stereoselectivity in X-Ph-CH=N(O)OMe always favored the *Z* isomer, however the ratio *Z:E* was dependent on the solvent [63]. B3LYP/6-31+G* calculations for these reactions suggested a kinetics preference for O-methylations because they presented lower barriers than the respective C-methylations [63]. Noteworthy that these and many other experimental studies were performed in solution, where the solvent can have significant effects that mask the intrinsic reactivity and selectivity [64]. In fact, the energy profile of S$_N$2 reactions in the gas-phase are quite different from those in solution [64, 65], which leads, for instance, to large differences between reaction rate constants [66, 67]. In addition, there have been reports of reversal of ordering of acidities and basicities in solution compared the gas-phase, and significant nucleophilicity differences of polarizable nucleophiles in solution and the gas-phase [68–70]. Thus, studying reactions in the gas-phase is relevant to determine the intrinsic reactivity and selectivity, which by comparisons with solution studies can be used to ascertain and, possibly, quantify the solvent effects. Indeed, reactions of alkyl-nitronates [R^{1}R^{2}CNO$_2$]$^-$, where R^1 = R^2 = H (**1**), R^1 = CH$_3$ and R^2 = H (**2**), R^1 = R^2 = CH$_3$ (**3**); and R^1 + R^2 = c-(CH$_2$)$_2$ (**4**), with iodomethane (CH$_3$I), depicted in Scheme 1, were studied in the gas-phase using the flowing afterglow technique and the reaction rates were measured [71]. The reaction with asymmetric nitronates, such as [CH$_3$CHNO$_2$]$^-$, can yield *Z* and *E* stereoisomers. The rate coefficient values are presented in Table 1.1.

Table 1.1 Rate coefficients for the S_N2 reaction $X^- + CH_3I \rightarrow CH_3X + I^-$.

X^-	$\Delta_{acid}H_{298}$ (HX) (kJ/mol)[a]	k_{obs} [71] $(10^{-10}cm^3s^{-1})$[b]	Reaction efficiency[c]
$[CH_2NO_2]^-$	1491	1.05	7%
$[CH_3CHNO_2]^-$	1489	1.50	10%
$[(CH_3)_2NO_2]^-$	1490	1.77	13%
$[c\text{-}(CH_2)_2NO_2]^-$	1534	5.02	35%

[a] Enthalpy of deprotonation for the conjugate acid HX at 298 K [72]. [b] Ref. [71], within an error of ±25%. [c] Reaction efficiency = k_{obs}/k_{col}, where the collision rate (k_{col}) is calculated using parametrized trajectory collision rate theory [36, 37].

It can be observed from Table 1.1 that as the central carbon of the nitronate $[R^1R^2CNO_2]^-$ becomes more substituted (crowed), the rate constant (k_{obs}) and the reaction efficiency increases. Because the negative charge of the nucleophile may be localized over the central carbon atom as well as the oxygen atoms of the nitro group, Kato et al. [71] proposed that the reaction can proceed via two pathways: $S_N2@C$ and $S_N2@O$ as illustrated in Scheme 1.2.
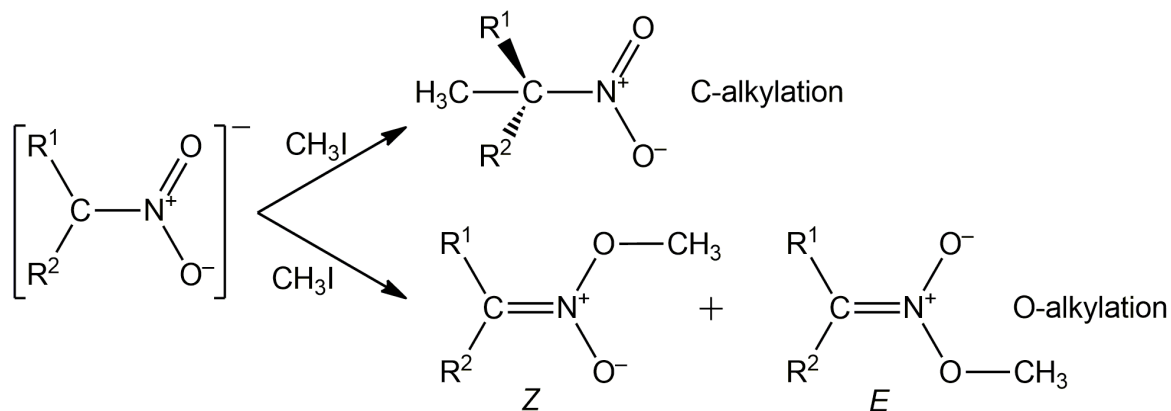
Scheme 1.2 Reactions of alkyl-nitronates $[R^1R^2CNO_2]^-$, where $R^1 = R^2 = H$ (**1**), $R^1 = CH_3$ and $R^2 = H$ (**2**), $R^1 = R^2 = CH_3$ (**3**); and $R^1 + R^2 = $ c-$(CH_2)_2$ (**4**), with iodomethane (CH_3I). For asymmetric nitronates such as **2**, the O-alkylation yields Z and E stereoisomers.

Based on the results in Table 1.1 and the fact that nitronic esters, $[R^1R^2CN(O)OR]$, are the primary products in solution for the reaction of nitronates, $[R^1R^2CNO_2]^-$, and trialkyloxonium tetrafluoroborates, $[R_3O]^+[BF_4]^-$, Kato et al. [71] proposed that O-methylation should be preferred because the steric effects would be insignificant in this pathway. However, because the neutral products could not be detected and characterized in these experiments, this suggestion about the C/O selectivity of this reaction could not be ascertained. As a result, our main goal consists in studying these reactions in the gas-phase with *ab initio* quantum chemical methods in order to determine the reaction mechanism and to explain its selectivity and reactivity. In fact, we intend to show that the C-methylation is thermodynamically and kinetically preferred, thus contradicting the proposed selectivity. In addition, the reactivity may be explained by different sp^3 character of the carbanion in the nucleophile (nitronate) and by the vibrational frequencies associated with the pyramidalization of this carbon atom.

1.4 Solvent Effects on S_N2 Reactions

The solvent effects on the thermodynamics, kinetics and spectroscopic properties of chemical and biological processes have been and continued to be an important aspect of study of such processes. This is mainly because the ions behave quite differently in the gas-phase than the same ions in solutions. The evidence comes from the large difference between rate constants of the identical reaction in the gas-phase and in solution [73, 74], the increased nucleophilicity of polarizable nucleophiles in solutions than in gas phase [75], and the different order of basicities and acidities in the two phases [76, 69]. Indeed, S_N2 reactions are affected by the presence of solvents, because they can cause hindrance by surrounding the nucleophile as well as the substrate. Polar aprotic solvents such as THF (tetrahydrofuran) are better reaction medium than

polar protic solvents because the latter solvent makes hydrogen bonds with the nucleophile thus hindering its approach to the substrate and thus reducing its reactivity. Thus, in order for a nucleophile to react, it has to (partially) desolvate, and possibly the substrate also has to (partially) desolvate. This effect is particularly important for small, negatively charged nucleophiles, because it can perform strong hydrogen bonds with protic solvents. Larger nucleophiles have their charges more diffused and delocalized which reduces the interaction with the solvent molecules. Thus, polar aprotic solvents such as DMSO, DMF, and CH_3CN tend to accelerate the substitution with negatively charged nucleophiles. In polar aprotic solvents, nucleophilicity mirrors basicity. Whereas, nonpolar solvents do not have any favorable interaction with the nucleophile and its nucleophilicity would be large; however, its solubility becomes a major issue.

As an example, the rate constant for the nucleophilic displacement reaction between CH_3Br and hydroxide ion at various degrees of hydration in gas-phase are given in Table 1.2 [73, 74, 77].

Table 1.2 Rate constant for the nucleophilic substitution reaction $CH_3Br + OH^- \cdot (H_2O)_n$ in gas-phase and aqueous solution.

Nucleophile	Rate constant [73, 74, 77] $(cm^3 \ molecule^{-1} \ s^{-1})$
OH^-	1×10^{-9}
$OH^- \cdot H_2O$	6.3×10^{-10}
$OH^- \cdot (H_2O)_2$	2.0×10^{-12}
$OH^- \cdot (H_2O)_3$	$\leq 2.0 \times 10^{-13}$
$OH^- (aq)$	2.3×10^{-25}

It can be seen from Table 1.2 that the reaction rate decreases significantly with the increase of degree of hydration in the nucleophile.

Figure 1.4 shows an example of energy profile for S_N2 reactions in the gas-phase has a double-well, separated by a central barrier, in contrast to the situation in solution phase that does not present the double-well [78–82].
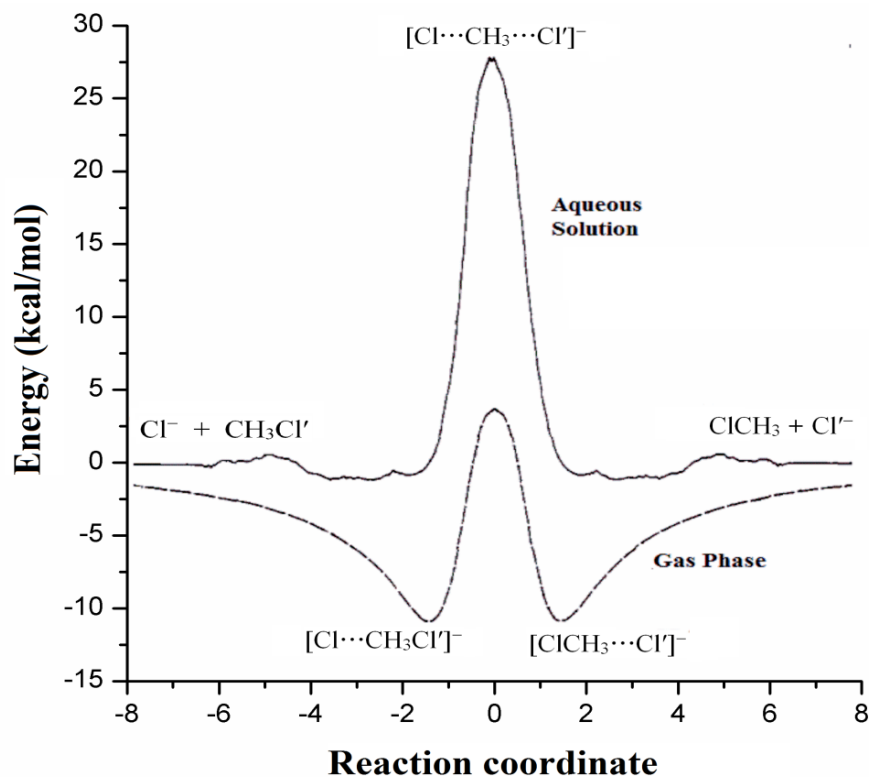
Figure 1.4. Energy profile for a S_N2 reaction between methyl chloride (CH$_3$Cl′) and chloride ion (Cl$^-$) in the gas-phase and aqueous solution determined by Monte Carlo simulations and ab initio quantum chemical calculations. Figure adapted from reference [83].

Figure 1.4 shows the energy profile a S_N2 reaction in the gas-phase and in aqueous solution. In the gas-phase, the reactants, Cl$^-$ + CH$_3$Cl′, interact attractively and form an ion-dipole complex [Cl⋯CH$_3$Cl′]$^-$ that is a minimum on the potential energy surface. This complex goes through a (distorted) trigonal bipyramid transition state [Cl⋯CH$_3$⋯Cl′]$^-$. The energy (~5–20 kcal mol^{-1}) [84] released in the formation of the ion-dipole reactant complex is converted into internal energy, so the initially formed reactant complex has sufficient energy to overcome the energy barrier associated with the transition state [Cl⋯CH$_3$⋯Cl′]$^-$ to form the product ion-dipole complex [ClCH$_3$⋯Cl′]$^-$, which dissociates to give separated products ClCH$_3$ + Cl′$^-$. When the reactants and the products are placed in aqueous solution, considerable amounts of energy are involved in the solvation of the charge localized on the ions and of the polar substrates. Thus, the

ion-dipole complex (either reactant or product) are not formed or form with a little driving energy and its equilibrium constant is usually ignored. Therefore, the reaction profile no longer presents the double-well. In addition, the charge is delocalized in the transition state and the solvation energy becomes smaller, which makes the energy barrier in solution phase higher than in the gas-phase [83, 85].

Therefore, the study of reactions in the gas-phase and solution reveals the role of the solvent in the chemical reactivity and allows for the quantification of the intrinsic reactivity. Theoretical models have proven to be successful to estimate the solute-solvent interaction and predicting the structures, spectroscopic properties and the reactivity of the reactions in solutions [86]. Solvent effects can be modelled by means of adding the solvent molecules explicitly in the surrounding. The other way is the use of continuum which is particularly preferred over other methods because of its cost-effective approach as compared to other methods. The continuum model divides the system into a solute part lying inside the cavity surrounded by a solvent part which is characterized as a structureless material, represented by its dielectric constant and other related parameters.

Chapter 2

Hypotheses, Thesis, Tests and Strategies

Hypotheses

The main hypotheses are that the reaction energy profiles as well as dynamics effects determine the selectivity of several reactions in the gas-phase, including alkylation of nitronates. The experimental increase of the rate constant of methylation of nitronates with the increase of steric hindrance round the central carbon is not due to the O-methylation being more favorable, but because of details in the reaction profiles and dynamics effects. These details of the reaction profiles are dictated by the electronic and molecular structure of the nitronate as well as the nature of the alkylating agent. For these reactions in solution, the solvent effects are important and are probably the determining reason for selectivity. However, the nature of the nitronate and of the alkylating agent can be very relevant and be used to control the regioselectivity of these reactions.

Thesis

Selectivity of the gas-phase reactions of nitronates with methyl iodide is controlled by the reaction profiles and dynamics effects, whereas in solution the solvent effects and the alkylating agent are determinant.

Test

Comparison of experimental and calculated rate constant using RRKM theory. A good agreement between the two rates will support the validity of the RRKM theory; otherwise, dynamics effects are significant. Validation of the quantum chemical methods by benchmark calculations with CCSD(T) and basis set extrapolation procedures. Comparison of rate constants, reactivity and selectivity of reactions in gas-phase and in solutions.

Strategies

Investigation of electronic and structural properties of nitronates using quantum chemical methods. Calculation of vibrational frequencies, thermochemical properties (free energy of the reactions, relative energies of reactants and products), kinetics properties (energies of activation, rate constant, kinetics equations for the reactions), and selectivities.

Calculation of rate constants for the formation of ion-dipole complex using Average-Dipole-Orientation (ADO) theory.

Determination of rate constant for the conversion of reactant complex into product complex passing through the transition state using RRKM theory.

Assessment and benchmarks of the methylation reactions between alkyl-nitronates and iodomethane.

Calculations of solvent effects using polarizable dielectric continuum (PCM) models for reactions of alkyl- and aryl-nitronates with different alkylating agents.

Chapter 3

Methodology

Reaction mechanisms are described basically by unimolecular or bimolecular elementary steps that are treated by the RRKM theory and the transition state theory (TST), respectively [87–92]. Most gas phase ion-neutral reactions are unimolecular because they form an intermediate reactant complex (charge-dipole), which can be treated by the RRKM theory assuming that the intermediate has a lifetime sufficiently long to redistribute the internal energy among all the degrees of freedom via intramolecular vibrational energy redistribution (IVR). The rate constant for the ion-dipole complex formation can be calculated by semiclassical models of dipole capture such as the ADO (Average Dipole Orientation) theory [36, 37]. If the intermediate reactant complex is not formed then the reaction rate can be calculated by the conventional TST or its variants such as variational TST. Indeed, both TST and RRKM theories have been used to study the dynamics of nucleophilic reactions in the gas phase [87–92]. A large number of theoretical studies on the usage and suitability of these statistical theories have been published by Hase and his colleagues [93–108] and D. G. Truhlar [109–114].

3.1 Transition state theory

Transition state theory (TST) assumes that there exists an activated complex or transition state (TS) between the reactants and products in a chemical reaction. The theory provides a simple expression for the rate constant that can be used for qualitative interpretations and/or quantitative calculations when the potential energy surface (PES) regions around the reactants and activated complex are known. Because of its easiness of interpretation and quantitative application, the TST has become the workhorse of the chemical kinetics [115]. From an interpretative point of view, the reaction rate can be calculated from the standard Gibbs free energy of activation $(\Delta^{\ddagger}G^0)$, which can be expressed in terms of enthalpy $(\Delta^{\ddagger}H^0)$ and entropy $(\Delta^{\ddagger}S^0)$ of activation. Transition state theory is also quoted as activated complex theory, absolute rate theory and the theory of absolute reaction rate. Collectively these theories are also classified as bimolecular theories of reaction rates. The transition state theory was developed at the same time in 1935 by Henry Eyring, and by Meredith Gwynne Evans and Michael Polanyi [116, 117].

The basic assumptions of the theory are as follows:

1. There exist a very short lived, unstable activated complex (transition state) between the reactants and products, which on the potential energy surface, lie near the saddle point.

2. The reactant molecules are distributed among their states according the Boltzmann distribution (thermal equilibrium).

3. The activated complex is in quasi-equilibrium with the reactant molecules [118], namely, their states are described by the Boltzmann distribution.

4. One internal degree of freedom of the transition state is converted into a translational degree of freedom along the reaction coordinate. Hence, this translational degree of freedom can be separated from other degrees of freedom.

5. The transition state defines a unique dividing surface for the reaction that acts as a point of no return and once the transition state is formed it proceeds to the products. The concentration of activated complex (TS) can be used to calculate the rate of this conversion into products.

3.1.1 Quasi-equilibrium derivation of transition state theory

Consider the following elementary reaction

$$A + B \rightleftharpoons [AB]^{\ddagger} \rightarrow C + D \tag{3.1}$$

where $[AB]^{\ddagger}$ is the activated complex. The pre-equilibrium step between reactants and activated complex is the quasi-equilibrium assumption of the transition state theory.

It is also assumed that the rate of formation of activated complex $[AB]^{\ddagger}$ is much faster than its dissociation into the product, so this latter step does not affect the pre-equilibrium and an equilibrium constant $K^{\ddagger}$ for the transition state and the reactants can be defined in the molarity (mol L^{-1}) concentration scale,

$$K^{\ddagger} = \frac{[AB]^{\ddagger}}{[A][B]}$$

So the molar concentration of activated complex $[AB]^{\ddagger}$ is

$$[AB]^{\ddagger} = K^{\ddagger}[A][B] \tag{3.2}$$

Because the rate of dissociation of the activated complex into the products, that is, the rate of the reaction depends on the concentration of the activated complex and the frequency at which it crosses the barrier, namely, the frequency of the decomposition of the activated complex into the product, the rate equation for the reaction can be written as

$$\text{Rate} = [AB]^{\ddagger} \times \text{frequency} = v \, K^{\ddagger}[A][B] \tag{3.3}$$

This frequency v is the number of times the transition state species evolves along the reaction coordinate, per time unit. This movement relates to the conversion of an internal degree of freedom into a translational degree of freedom and it corresponds to a very loose vibration that is responsible for the dissociation of the activated complex into products. Therefore, this vibrational degree of freedom vanishes during the dissociation of activated complex. The vibrational degrees of freedom of a nonlinear activated complex are, therefore, $3(N_A + N_B) - 7$; one less than that of a normal (stable) nonlinear molecule. The imaginary frequency related to the saddle point in the potential energy surface is then transformed into a translational degree of freedom when the transition state goes to the products [29, 119]. Namely, taking the limit of the harmonic oscillator contribution to the partition function for $hv << k_{\mathrm{B}}T$ (vibration to translation transformation), we obtain

$$K^{\ddagger} = q^{\ddagger}vK_{\ddagger} \cong \frac{k_{\mathrm{B}}T}{hv}K_{\ddagger} \tag{3.4}$$

where k_B and h are the Boltzmann and the Planck constants, respectively and $q^{\ddagger}$ is the vibrational partition function of the normal mode related to the reaction coordinate. Substituting equation 3.4 in equation 3.3, we get

$$\text{Rate of reaction} = \frac{k_B T}{h} K_{\ddagger} [A][B] \tag{3.5}$$

Now if k is the rate constant for a given elementary reaction $A + B \xrightarrow{k} Products$, then experimentally the rate of the reaction can be written as

$$\text{Rate of reaction} = k[A][B] \tag{3.6}$$

Comparing equations 3.5 and 3.6, we get

$$k_{TS} = \frac{k_B T}{h} K_{\ddagger} \tag{3.7}$$

Equation 3.7 is the equation for the rate constant in terms of quasi-equilibrium constant for formation of activated complex ($K_{\ddagger}$) that can be expressed in terms of either partition functions or thermodynamic functions [119–123].

3.1.2 Thermodynamic approach

The quasi-equilibrium constant $K_{\ddagger}$ for the formation of activated complex is related to the free energy change $\Delta^{\ddagger} G^0$ and can be expressed by a well known equation of thermodynamics.

$$\Delta^{\ddagger} G^0 = -RT \ln K_{\ddagger}$$

$$\ln K_{\ddagger} = -\frac{\Delta^{\ddagger} G^0}{RT} \Leftrightarrow K_{\ddagger} = e^{-\Delta^{\ddagger} G^0 / RT}$$

where R is the gas constant.

We can substitute the expression for $K_{\ddagger}$ in equation 3.7 to yield

$$k_{\text{TS}} = \frac{k_{\text{B}}T}{h} e^{-\Delta^{\ddagger}G^0/RT} \tag{3.8}$$

where $\Delta^{\ddagger}G^0$ is standard Gibbs energy change for the formation of the transition state from reactants and is called Gibbs energy of activation.

However, from the Gibbs-Helmholtz relation

$$\Delta G = \Delta H - T\Delta S,$$

equation 3.8 can be rewritten yet again into the following form

$$k_{\text{TS}} = \frac{k_{\text{B}}T}{h} e^{-(\Delta^{\ddagger}H^0 - T\Delta^{\ddagger}S^0)/RT} = \frac{k_{\text{B}}T}{h} e^{\Delta^{\ddagger}S^0/R} e^{-\Delta^{\ddagger}H^0/RT} \tag{3.9}$$

where $\Delta^{\ddagger}H^0$ and $\Delta^{\ddagger}S^0$ are the enthalpy and entropy of the activation, respectively. Equations 3.8 and 3.9 show that the rate constant is determined from the free energy of activation ($\Delta^{\ddagger}G^0$) or from the enthalpy ($\Delta^{\ddagger}H^0$) and entropy ($\Delta^{\ddagger}S^0$) of the activation associated only with the reactants and the transition state (activated complex) in their standard form [119–123].

3.1.3 Partition function approach

The equilibrium constant can also be written in terms of partition function [119–121] and the concentration of activated complex can be expressed as

$$[AB]^{\ddagger} = \frac{Q_{[AB]^{\ddagger}}}{Q_A Q_B} e^{-\Delta E_0/RT}[A][B] \tag{3.10}$$

where $Q_{[AB]^{\ddagger}}$, Q_A and Q_B are the transition state, reactant A and reactant B partition functions, excluding the electronic degrees of freedom and the zero-point energy, which are incorporated into ΔE_0 that is the electronic energy difference between the zero-point energies (ZPEs) of the reactants and transition state. ΔE_0 is the amount of energy required by the reactants to reach the transition state at 0 K. The imaginary frequency associated with the transition state can be separated from its partition function and treated as a vanishing vibration [119–123], namely,

$$q = \lim_{h\nu \ll k_{\mathrm{B}}T} \frac{1}{1 - e^{-h\nu/k_{\mathrm{B}}T}} = \lim_{h\nu \ll k_{\mathrm{B}}T} \frac{1}{1 - \left(1 - \frac{h\nu}{k_{\mathrm{B}}T} + \cdots\right)} \cong \frac{k_{\mathrm{B}}T}{h\nu}$$

Thus, equation 3.10 can be rewritten as

$$[\mathrm{AB}]^{\ddagger} = \frac{k_{\mathrm{B}}T}{h\nu} \frac{Q^{\ddagger}}{Q_{\mathrm{A}}Q_{\mathrm{B}}} e^{-\Delta E_0/RT}[\mathrm{A}][\mathrm{B}]$$

where $Q^{\ddagger}$ is the transition state partition function excluding the imaginary frequency. Because the rate of the reaction from transition state theory is given by the equation 3.3, that is,

$$\text{Rate of the reaction} = \nu\,[\mathrm{AB}]^{\ddagger} \tag{3.11}$$

we obtain

$$\text{Rate of reaction} = \frac{k_{\mathrm{B}}T}{h} \frac{Q^{\ddagger}}{Q_{\mathrm{A}}Q_{\mathrm{B}}} e^{-\Delta E_0/RT}[\mathrm{A}][\mathrm{B}]$$

Now referring to equation 3.6, the experimental rate of the elementary reaction is $k[\mathrm{A}][\mathrm{B}]$. Thus, the rate constant in terms of partition function is given by

$$k_{\mathrm{TS}} = \frac{k_{\mathrm{B}}T}{h} \frac{Q^{\ddagger}}{Q_{\mathrm{A}}Q_{\mathrm{B}}} e^{-\Delta E_0/RT} \tag{3.12}$$

where $Q^{\ddagger}$ has $3(N_{\mathrm{A}} + N_{\mathrm{B}}) - 7$ vibrational modes if it is non-linear and $3(N_{\mathrm{A}} + N_{\mathrm{B}}) - 6$ if linear.

3.1.4 Translation partition function

As discussed above, one of the vibrational degrees of freedom in the transition state is of different character and is responsible for the dissociation for activated complex into the products. This vibrational degree of freedom becomes a translation along the reaction coordinate. That is the reason the transition state has one vibration degree of freedom less than that of a normal (stable) species.

Now instead of using vibrational partition function, we can also use translational partition function to illustrate the motion of activated complex over the barrier of activation energy.

Considering that the activated complexes lie within an interval Δx of the barrier (Figure 3.1), the frequency of the conversion of the transition state species into the products can be calculated by the velocity of the crossing the transition state over the length Δx at the top of the barrier [120–124].
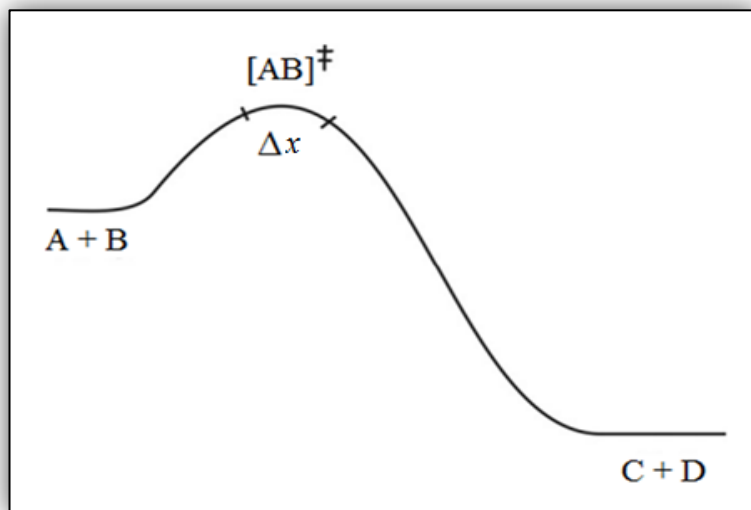
Figure 3.1 Potential energy curve for a reaction passing through a transition state $[AB]^{\ddagger}$ contained in a fictitious box Δx.

The translational partition function for the particle of mass m in the box of length Δx can be written as

$$q = \frac{(2\pi m k_B T)^{1/2}}{h} \Delta x \tag{3.13}$$

giving the rate constant

$$k = \nu^{\ddagger} \frac{(2\pi m k_B T)^{1/2} \Delta x}{h} \frac{Q_{[AB]^{\ddagger}}}{Q_A Q_B} e^{-\Delta E_0/RT} \tag{3.14}$$

It is assumed that the dynamics of the reaction coordinates are always in the direction of the product side once the activated complex has been formed, because recrossing, that is, the motion

backwards to the reactant side is assumed to be negligible in the theory. The average velocity of the motion of the particles from left to right over the barrier is given by kinetic theory as

$$V^{\ddagger} = \sqrt{\frac{k_B T}{2\pi m}} \tag{3.15}$$

Thus, frequency of the passage of the activated complexes over the barrier, $v^{\ddagger}$, is given by

$$v^{\ddagger} = \frac{V^{\ddagger}}{\Delta x} = \frac{1}{\Delta x}\sqrt{\frac{k_B T}{2\pi m}} \tag{3.16}$$

Substituting this expression into the equation 3.14 for rate constant gives the same equation 3.12.

$$k_{TS} = \frac{k_B T}{h}\frac{Q^{\ddagger}}{Q_A Q_B}e^{-\Delta E_0/RT} \tag{3.17}$$

which is known as the Erying equation. The relevance of this derivation is because it provides an alternative interpretation to the quasi-equilibrium assumption, namely, that it is equivalent to the non-recrossing assumption. The recrossing is a dynamics concepts that is usually incorporate ad hoc into the transition state theory by a transmission coefficient κ [122–123].

3.1.5 Limitations of transition state theory

Transition state theory is widely used to understand the mechanism and selectivity of chemical reactions, but there are some limitations of the theory. For example, when applied to the multi-step reactions; the theory assumes that each intermediate is long-lived enough to reach the Boltzmann distribution of energy before it proceeds to the next step. However, when intermediates are very short-lived, the TST fails to explain those reactions. In this case, the mechanism and selectivity of the reaction may be driven by dynamics effects during the conversion of reactants into products. For light atom transfers, especially hydrogen, the tunneling effects have to be included in the TST because it might be relevant for the reaction rate. Tunneling and non-classical reflection corrections are incorporated into the calculations using the zero curvature tunneling method. The tunneling probability largely depends on the reaction path

curvature. A functional form of one-dimensional potential barrier, $V(R)$, is substituted in the one-dimensional Schrödinger equation and then the equation is solved at a point to the left of the barrier, inside the barrier where the kinetic energy is negative and to the right of the barrier where is kinetic energy is positive. Thus, the tunneling probability can be calculated for any potential function [125–127].

The assumption that the transition state is a diving surface on the reaction path that acts as a point of no return implies that the rate of the reaction can be calculated by counting the trajectories crossing this diving surface in the direction of product. This assumption causes the overestimation in the rate because some trajectories do recross the dividing surface. Such trajectories are counted more than once and hence lead to an overestimation of the rate constant. Therefore, recrossings need to be taken into account by variational approaches to TST. Variational transition state theory suggests that instead of calculating the rate of the crossings at the top of the barrier (transition state), we can consider the dividing surface at various positions along the reaction path. The rate of crossing at these dividing surfaces can then be calculated and the lowest calculated rate would be closest to the true rate of the reaction [126, 128–131].

3.2 Theories of unimolecular reaction rates

Usually, the ionic reactants in gas-phase reactions form an ion-dipole complex before they pass through the transition state, in contrast to reactions in solutions. This ion-dipole complex is a stationary point on the potential energy surface and is considered as a single stable species because the two reactants are bound together due to the strong intermolecular forces. This reactant complex then gives a product complex after through the transition state. The mechanism of this conversion of reactant complex into the product complex through the transition state structure can be described using unimolecular theories of reaction. A unimolecular reaction in gas-phase is the simplest kind of reaction that involves the decomposition of a single reactant. The unimolecular reactions have been the subject of great interest for more than a century. Different theories have been proposed to explain the mechanism of these reactions [132].

3.2.1 Lindemann-Hinshelwood theory

Lindemann in 1922 [132] showed that the reaction kinetics can be unimolecular if the rate of activation and deactivation of the molecules is large as compared to the overall rate of the reaction, irrespective of the order of the activation process. This theory forms the basis of all the theories of unimolecular reactions.

During collisions the molecules transfer energy and become activated (A^*). The activated molecules have higher translational and internal (vibrational and rotational) energy that might be sufficient to undergo a reaction. The activated molecules might also be deactivated through collisions with other molecules and the container walls, represented generically by M. The rate of activation and deactivation depends of the collision number.

$$A + M \; \underset{k_{-1}}{\overset{k_1}{\rightleftharpoons}} \; A^* + M$$
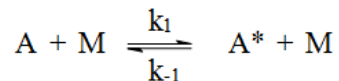
The activated molecules that have increased internal (vibrational and rotational) energy then dissociate into product $A^* \rightarrow P$ with a rate constant (k_2) that is assumed to be independent of the energy content. This unimolecular step is the rate-determining step at high pressure, though the process of producing A^* is bimolecular. Because A^* is an activated molecule and reactive intermediate, the steady-state approximation can be applied, that is, the concentration of the energized (activated) molecules can be considered as constant during the progress of the reaction, it gives

$$[A^*] = \frac{k_1[A][M]}{k_{-1}[M] + k_2} \tag{3.18}$$

So the overall rate is

$$\frac{d[P]}{dt} = k_2[A^*] = \frac{k_1 k_2[A][M]}{k_{-1}[M] + k_2} = k_{eff}[A] \tag{3.19}$$

where $k_{eff} = \frac{k_1 k_2[M]}{k_{-1}[M] + k_2}$ is the effective first order rate constant and is a function of pressure. At high pressure, the rate of collisional deactivation of A^* is more than its decomposition into products, so the decomposition step is the rate-determining step and the reaction is first order. At low pressure, the bimolecular activation of the molecules is the rate-determining step. Once A^* is formed, it is more likely to react than to be deactivated due to a collisions with other reactant molecules.

There are two major failures of the theory:

- The bimolecular step does not consider the energy dependence of the activation and the internal degrees of freedom of the molecules are completely neglected. The theory underestimates the rate of activation, especially for large molecules.

- The theory fails to explain the unimolecular reactions involving one specific form of molecular motion, e.g. rotation around the double bond in *cis-trans* isomerization.

To correct these failures, Hinshelwood in 1926 [133], accounted for internal degrees of freedom during the activation process of the molecules. He proposed that, in addition to the relative motion (translation energy), the internal degrees of freedom can contribute to the threshold energy, E_0, needed in the activation step (k_1). The probability that a molecule contains energy greater than E_0 increases with number of internal degrees of freedom. Thus, the activation rate constant k_1 is larger for a complex molecule than simple one.

3.2.2 RRK theory

In 1927–1928, Rice and Ramsperger [134, 135] and independently Kassel [128, 129, 136, 137] recognized that the rate of a unimolecular reaction should depend on the vibrational energy of the activated molecules, given origin to the RRK theory. They presented the idea that there must be

some minimum of energy localized in specific mode(s) in order for the dissociation step to take place.

The theory assumes a free flow of energy among the vibrational modes within the molecule because the molecular vibrations are highly anharmonic at high energies and they can be considered as strongly coupled. The probability that a molecule of s classical oscillators with total energy E has energy greater than or equal to E_0 in one chosen oscillator, which the critical mode leading to the reaction, is

$$P_{E_0}^E = \left(\frac{E - E_0}{E}\right)^{s-1} \tag{3.20}$$

The expression for classical RRK rate constant is simply the product of this probability and the vibrational frequency of the critical oscillator (ν), i.e., can then be written as

$$k_{RRK}^{classical}(E) = \nu \left(\frac{E - E_0}{E}\right)^{s-1} \tag{3.21}$$

The quantum version of the RRK rate constant is

$$k_{RRK}^{quantum}(E = jh\nu) = \nu \frac{(j - m + s - 1)!\, j!}{(j - m)!\, (j + s - 1)!} \tag{3.22}$$

which in the classical limit, where $j \gg s$ and $j - m \gg s$, becomes,

$$k_{RRK}^{j \gg s;\, j-m \gg s}(E = jh\nu) = \nu \left(\frac{j - m}{j}\right)^{s-1} \tag{3.23}$$

If both the numerator and denominator are multiplied by $(h\nu)^{s-1}$, this equation becomes the classical RRK rate constant.

This expression has two important features. It predicts that the rates are strongly dependent on the number of vibrational oscillators s (figure 3.2) and that the rate increases as the total energy E increases, because at high energy, every energized molecule A* is an activated molecule and therefore, can be converted immediately into the product.
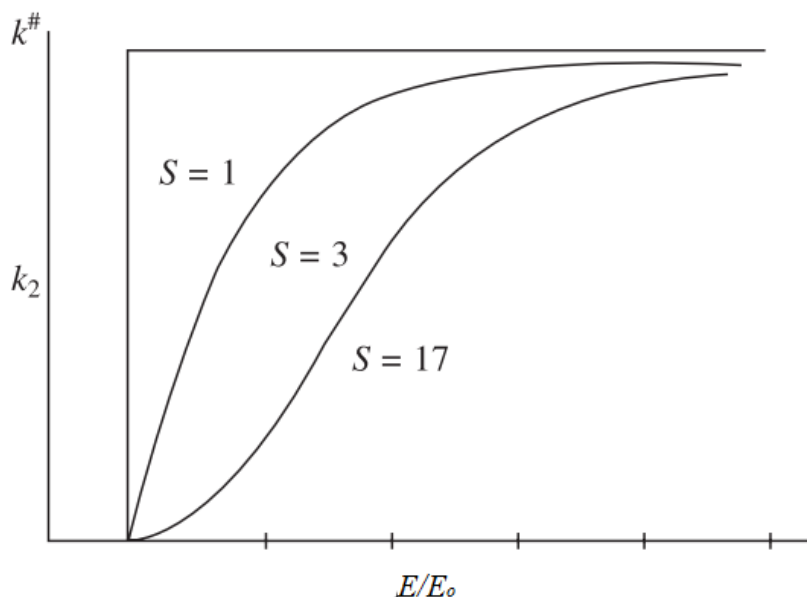
Figure 3.2 Variation of rate constant k_2 with E/E_o according to RRK theory for a molecule having s vibrational modes. Figure adapted from reference [138].

Although the general predictions of the RRK theory are correct, it was unable to give the quantitative rate constants due to several reasons. One of the main deficiencies is the neglect of the zero-point energy effects.

In 1952, Marcus extended the RRK theory to consider explicitly vibrational and rotational states and to include zero-point energy effects, giving origin to the RRKM theory [139, 140].

3.2.3 RRKM theory

The development of RRKM theory is a great achievement of theoretical chemists [141–144]. The theory takes into account the temperature and pressure dependence of the rate of activation and unimolecular dissociation. It merges RRK theory with the quantum transition state theory to provide a better modeling to reproduce a wide variety of experimental results [145, 146].

The RRKM is actually the transition state theory applied to the unimolecular reactions. It describes the energy dependence of unimolecular dissociation reactions. Thus, the focus is the activated complex.

$$A^* \rightarrow A^{\ddagger} \rightarrow \text{Product} \qquad (3.24)$$

The formation and dissociation of the activated complex is very relevant in the reaction coordinate. The activation energy barrier is determined from the potential energy surface at the position of activated complex.

3.2.3.1 Microcanonical RRKM theory

From equation 3.24, we can say that the rate of the reaction depends on rate of disappearance of A. Alternatively, it is proportional to the rate at which the activated complex $A^{\ddagger}$ passes over the barrier. The major assumptions of the RRKM theory are same as that of transition state theory. The two main assumption used in the derivation are

➢ The total internal energy has equal probability to be distributed among the internal degrees of freedom of the activated complex and the translational energy of the reaction coordinate. This implies a fast and complete randomization of the available energy among all active modes, that is, the total phase space is populated statistically. This means that the population density is uniform over the whole phase space. It is recognized that there is some part of the energy that is assigned to a particular mode and hence not distributable. For example, the zero-point energy of the vibrations and a fraction of rotational energy that is bound to the rotational modes due to the conservation of angular momentum. Therefore, the energy that can be distributed freely is the vibrational energy and, to some extent, rotational energy [138, 139].

➢ A transition state is defined as a dividing surface between the reactants and products. The theory assumes that once having crossed the dividing surface, activated complex will move in the forward direction towards the product side and cannot recross back to

reactants, that is, there is no recrossing at this point. These recorssings would reduce the rate and hence RRKM theory would overestimate the rate constant [138, 139].

A unimolecular reaction can be described as a reaction flux in phase space. Any microcanonical system (constant energy) has total energy that can be described by Hamiltonian as $H = E$. Now, if the total energy is greater than the critical energy, E_0, the molecule has a probability to reach the critical surface (transition state) that divides the reactants and the products. At this critical surface, the molecules dissociate along the reaction coordinate, which is the minimum energy path. It is assumed that at this critical point (the saddle-point region), the reaction coordinate is separable from all the other coordinates because this particular reaction coordinate is perpendicular to all the other coordinates.

Thus for any microcanonical system whose reaction coordinate have values ranging from $q_1^\ddagger$ to $q_1^\ddagger + dq_1^\ddagger$ and $p_1^\ddagger$ to $p_1^\ddagger + dp_1^\ddagger$, the Hamiltonian can be written as

$$H = H_{trans}^\ddagger + H^\ddagger \tag{3.25}$$

where

$$H_{trans}^\ddagger = \frac{(p_1^\ddagger)^2}{2\mu_1^\ddagger} = E_1^\ddagger \tag{3.26}$$

with $E_1^\ddagger$ being the energy at the reaction coordinate having position $q_1^\ddagger$ and the momentum $p_1^\ddagger$, which is separable from other degrees of freedom and $\mu_1^\ddagger$ is reduced mass of the molecule passing through the barrier. Taking the derivative of the above equation, we get

$$dE_1^\ddagger = \frac{p_1^\ddagger}{\mu_1^\ddagger} dp_1^\ddagger \tag{3.27}$$

The fraction of the molecules in the transition state with a particular energy between the internal degrees of freedom of the activated complex and the translational energy related to the reaction coordinate can be obtained by dividing the phase space at the diving surface (transition state) by

the total phase space. In other words, it is the ratio of number of states in the transition state, $dN^{\ddagger}(q_1^{\ddagger},\ p_1^{\ddagger})$, to the total number of states in the reactants, $N(E)$,

$$\frac{dN^{\ddagger}(q_1^{\ddagger},\ p_1^{\ddagger})}{N(E)} \qquad (3.28)$$

In classical mechanics, the total number of states $N(E)$ is denoted as density of state. If we consider a reaction coordinate at position $q_1^{\ddagger}$ and the momentum $p_1^{\ddagger}$ with a particular energy $E_1^{\ddagger}$ in the reaction coordinate, the number of states in the reaction coordinate can be written as

$$\frac{dq_1^{\ddagger}dp_1^{\ddagger}}{h}$$

In any microcanonical system, the activation energy E_0 and the translational energy $E_1^{\ddagger}$ at the saddle point region is not available to be distributed among the internal modes. Therefore, both of these energies must be subtracted from the total energy. The measured energy at the transition state is then $E^{'} = E - E_1^{\ddagger} - E_0$. The fraction of the molecules in the transition state can then be written as

$$\frac{dN^{\ddagger}(q_1^{\ddagger},p_1^{\ddagger})}{N(E)} = \frac{(dq_1^{\ddagger}dp_1^{\ddagger}/h)\ N^{\ddagger}(E - E_1^{\ddagger} - E_0)}{N(E)} \qquad (3.29)$$

where $N(E)$ is the density of state of the reactant and $N^{\ddagger}(E)$ is the density of states of the transition state.

The number of activated complexes passing over the barrier per unit time can be written in the form of Hamilton equations of motion

$$\frac{dq_1^{\ddagger}}{dt} = \frac{\partial H_{trans}^{\ddagger}}{\partial p_1^{\ddagger}} = \frac{p_1^{\ddagger}}{\mu_1^{\ddagger}} \qquad (3.30)$$

or

$$dq_1^{\ddagger} = \left(p_1^{\ddagger}/\mu_1^{\ddagger}\right)dt \tag{3.31}$$

If we substitute equation 3.31 in equation 3.29, we get the following equation

$$\frac{dN^{\ddagger}(q_1^{\ddagger}, p_1^{\ddagger})}{N(E)} = dt \left(\frac{p_1^{\ddagger}}{\mu_1^{\ddagger}}\right) \frac{dp_1^{\ddagger}}{h} \frac{N^{\ddagger}(E - E_1^{\ddagger} - E_0)}{N(E)} \tag{3.32}$$

Now by substituting $dE_1^{\ddagger} = p_1^{\ddagger}dp_1^{\ddagger}/\mu_1^{\ddagger}$ from equation 3.27, and rearranging, the above equation can be rewritten in the following form

$$\frac{dN^{\ddagger}(q_1^{\ddagger}, p_1^{\ddagger})}{dt} = \frac{dE_1^{\ddagger}N^{\ddagger}(E - E_1^{\ddagger} - E_0)}{hN(E)} N(E) \tag{3.33}$$

The theory assumes the configuration of no return, which in the context of dynamics implies that it is not necessary to follow the trajectories all the way from reactants to the products rather it is sufficient to count the rate at which molecules pass through the top of the barrier.

Finally, to calculate the total number of activated complexes passing through the barrier per unit time, that is, the total rate of dissociation, we must integrate the equation 3.33 over $E_1^{\ddagger}$ within limits from 0 to $E - E_0$.

$$\frac{dN^{\ddagger}(q_1^{\ddagger}, p_1^{\ddagger})}{dt} = \left[\frac{\int_0^{E-E_0} dE_1^{\ddagger} \ N^{\ddagger}(E - E_1^{\ddagger} - E_0)}{hN(E)}\right] N(E) \tag{3.34}$$

We have used the first assumption in this step, that is, we have considered that there is equal probability of all the possible ways of partitioning of a given total energy between internal degree of freedom of activated complex and the translational energy of reaction coordinates.

Equation 3.34 can be rearranged to give

$$k_{\text{RRKM}}(E) = \frac{\int_0^{E-E_0} dE_1^\ddagger \, N^\ddagger\big([E - E_0] - E_1^\ddagger\big)}{hN(E)} \equiv \frac{G^\ddagger(E - E_0)}{hN(E)} \tag{3.35}$$

where $G^\ddagger(E - E_o)$ is the sum of the states in the transition state at energy $E - E_o$. $N(E)$ is the density of states of the reactant. Neglecting the rotations, the equation 3.35 is the expression for the standard RRKM.

Until now, we have ignored the rotational motion while deriving the expression for rate constant. The rotational energy is not active, for it to be considered in overcoming the energy threshold, therefore we subtract the rotational energy from the total energy in above equation. The activated complex is usually larger in size than the reactants, so it has larger moment of inertia. Therefore, total rotational energy of the complex $E_r^\ddagger$ is less than the total rotational energy of the reactants E_r. The difference in the rotational energy is distributed among the vibrational degrees of freedom of the activated complex as the total energy is conserved for any system. Therefore, we subtract the rotational energies of reactants and activated complex from the overall rotational energy.

$$k_{\text{RRKM}}(E) = \frac{G^\ddagger\big(E - E_0 - E_r^\ddagger\big)}{hN(E - E_r)} \tag{3.36}$$

where E is the sum of vibrational and rotational energy and $E - E_0 = E^\ddagger + E_r^\ddagger$ with $E^\ddagger$ being the available energy in the complex minus the rotational energy. The rate constant has a proper unit of unimolecular rate constant, that is, $[\text{time}]^{-1}$.

The reaction coordinate was treated according to classical mechanics, whereas the sum and density of states should be treated according to quantum mechanics. Because $N^\ddagger(E)$ is not a continuous function due to the quantization of the energy; the integral in equation 3.35 should be replaced by a sum, that is, sum of states should be calculated by the direct sum of number of states, i.e.,

$$G^\ddagger(E)^\ddagger = \sum_i \Theta\,(E^\ddagger - E_i^\ddagger) \tag{3.37}$$

Thus, the RRKM theory states that the rate constant increases with the internal energy, but in a stepwise manner as shown in the figure 3.3. This trend has been confirmed experimentally [145, 146].
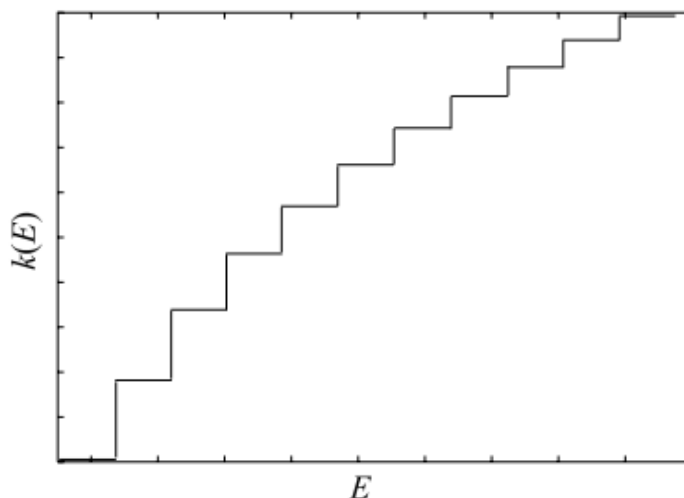
Figure 3.3 Stepwise increase in the rate constant according to the RRKM theory. Figure adapted from reference [138].

In the derivation of the RRKM equation, we have chosen to ignore the symmetry numbers in the calculation of sum and density of states of the reactant and the transition state. To count their effect, the sum of states of the activated complex and the density of states of the reactant should be divided by their symmetry numbers $\sigma^{\ddagger}$ and σ_r, respectively. The equation 3.36 can then be written as

$$k_{\text{RRKM}}(E) = \sigma \frac{G^{\ddagger}(E - E_0 - E_r^{\ddagger})}{hN(E - E_r)} \qquad (3.38)$$

where σ is the degeneracy of the reaction. It is the ratio of symmetry numbers of the reactants and the transition state, that is, $\sigma = \sigma_r/\sigma^{\ddagger}$.

To calculate the sum and density of states, we need the barrier heights corrected for zero-point energies E_0 and geometry and vibrational frequency of activated complex and the reactants. The

moment of inertia can be calculated from the geometry of the system. All these properties can be determined from potential energy surface. Modern electronic structure methods can then be employed to calculate the PES with high accuracy. If, for example, there exist a saddle point, these methods can calculate the properties of the activated complex, but if the saddle point does not exist on the potential energy surface, that is, no barrier on the potential energy surface, then we have to introduce the concept of the variational transition-state theory, which is based on the variational theorem [138, 141].

We have to recall the notion that the saddle point is a point on the potential energy surface, where we have least rate of transformation of reactants into products. This can be seen from equation 3.43, where it can be observed that the sum of states changes as the reaction proceeds and at the top of the barrier there is smallest number of states of the activated complex $G^{\ddagger}(E^{\ddagger})$, because at this point the energy available to the activated complex is minimum as shown in figure 3.4.
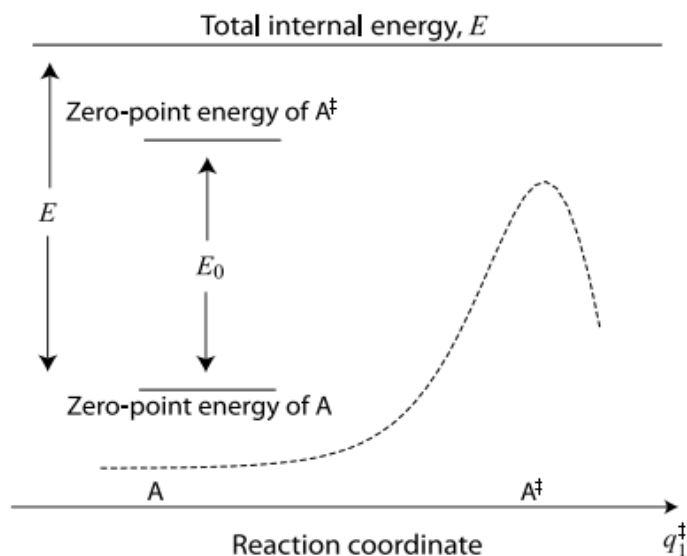
Figure 3.4 Schematics of the reaction energy profile and the relative energies and positions.

The presence or absence of saddle point is an important feature in the implementation of RRKM theory. With a well-defined saddle point, the variational effects are relatively minor; however, an appropriate treatment of tunneling may be required to get adequate results. Whereas in the absence of saddle point, variational effects can be of key importance.

In case of absence of the saddle point, we have to search directly for the geometric configuration corresponding to minimum in sum of states. This minimum flux configuration arises because as the reaction proceeds, the potential energy increases constantly and the vibrational frequencies decrease as they are evolving into product rotations and the translations. The sum of states decreases with the reduction in the available energy and increases with the decrease of vibrational frequencies. The minimum flux configuration (having minimum density of states) arises as a result of these two opposing factors at a point along the reaction coordinate, say $R^{\ddagger}$. The transition state located at $R^{\ddagger}$ is referred as entropic bottleneck, which in variational TST, corresponds to the minimum in the free energy. Thus, according to variational transition state theory, the rate constant is the function of reaction coordinate, and that the minimum corresponds to the activated complex [138, 141].

3.2.3.2 Canonical RRKM theory

The expression for temperature dependent rate constant $k(T)$ can be obtained by calculating an average of the distribution of internal energies at some temperature T. This distribution can be obtained from the Boltzmann distribution of energy, which is given by the equation as

$$P(E,T) = \frac{N(E)e^{-E/k_{\mathrm{B}}T}}{Q(T)} \qquad (3.39)$$

where $Q(T)$ is the partition function for the system at some temperature T. The rate constant can then be calculated using following integration

$$k(T) = \int_{E_0}^{\infty} k(E)P(E,T)\mathrm{d}E \qquad (3.40)$$

Substituting the values of $k(E)$ and $P(E,T)$ from equations 3.35 and 3.39 in equation 3.40, with total energy given as $E = E^{\ddagger} + E_0$, we get

$$k(T) = \int_{E_0}^{\infty} \frac{G^{\ddagger}(E - E_0)e^{-E/k_{\mathrm{B}}T}}{hQ(T)}\mathrm{d}E$$

or

$$k(T) = \frac{1}{hQ(T)} \int_{E_0}^{\infty} G^{\ddagger}(E - E_0) e^{-E/k_B T} dE$$

$$= \frac{e^{-E_0/k_B T}}{hQ(T)} \int_0^{\infty} G^{\ddagger}(E^{\ddagger}) e^{-E^{\ddagger}/k_B T} dE^{\ddagger}$$

$$= -k_B T \frac{e^{-E_0/k_B T}}{hQ(T)} \int_0^{\infty} G^{\ddagger}(E^{\ddagger}) \left[\frac{d}{dE^{\ddagger}} e^{-E^{\ddagger}/k_B T} \right] dE^{\ddagger}$$

Integration by parts yields

$$k(T) = -k_B T \frac{e^{-E_0/k_B T}}{hQ(T)} \left\{ \left[G^{\ddagger}(E^{\ddagger}) e^{-E^{\ddagger}/k_B T} \right]_0^{\infty} - \int_0^{\infty} \frac{dG^{\ddagger}(E^{\ddagger})}{dE^{\ddagger}} e^{-E^{\ddagger}/k_B T} dE^{\ddagger} \right\}$$

or

$$k(T) = \frac{k_B T}{h} \frac{\int_0^{\infty} N^{\ddagger}(E^{\ddagger}) e^{-E^{\ddagger}/k_B T} dE^{\ddagger}}{Q(T)} e^{-E_0/k_B T} \tag{3.41}$$

because $G^{\ddagger}(E^{\ddagger} = 0) = 0$ and $e^{-E^{\ddagger}/k_B T} \to 0$ as $E^{\ddagger} \to \infty$, as well as, $N^{\ddagger}(E^{\ddagger}) = dG^{\ddagger}(E^{\ddagger})/dE^{\ddagger}$.

The integral in equation 3.41 can be written as $Q^{\ddagger}(T)$, so we get the following equation

$$k_{RRKM}(T) = \frac{k_B T}{h} \frac{Q^{\ddagger}(T)}{Q(T)} e^{-E_0/k_B T} \tag{3.42}$$

where $Q^{\ddagger}$ and Q are the vibrational-rotational partition functions of the activated complex and reactants, respectively. Equation 3.42 is the expression for the high-pressure canonical rate constant for a unimolecular reaction, which is the same as obtained from transition state theory. This demonstrates the fact that the RRKM theory is actually the canonical version of TST when

Boltzmann distribution of energy is used. Therefore, the RRKM theory is also termed as microcanonical version of canonical rate constant [138].

In the recent years, the applications of the theory have been extended from primary empirical models for interpreting, interpolating and extrapolating the experiment data, to make *a priori* predictions. These transformations are a result of the continuous advances in the quantum chemistry. The theory has been tested widely for a number of inventive theoretical and experimental studies [147]; though, there are some limitations in its applicability, for example to timescale for picoseconds, the non-RRKM behavior and presence of recrossings. Nonetheless, the primary conclusion about the RRKM theory is that it is valid for the vast majority of unimolecular reactions.

3.3 Average Dipole Orientation (ADO) theory

We discussed that as the nucleophile collides with a substrate, an ion-dipole reactant complex is formed, which is more stable than the separated reactants. The complex formation step can be described by different methods such as Langevin-Gioumousis-Stevenson ion-molecule collision theory [148, 149] or the trajectory calculation-parameterized method given by Su and co-workers [36, 37, 149–152].

The ADO theory uses some statistical methods to calculate the average interaction energy between the ion and dipole and then a Langevin procedure to calculate the rate constant. The theory has been shown to predict the correct dependence of capture rate constant on the dipole moment of the substrate molecule [153, 154] and to predict quite accurately the absolute capture rate constants [154, 155].

We have used the parameterized ADO theory to predict the capture rate constants for the ionic systems: $[CH_2NO_2]^-$, $[CH_3CHNO_2]^-$, $[(CH_3)_2CNO_2]^-$ and $[c-(CH_2)_2CHNO_2]^-$. For the ADO theory to predict the rates accurately, the reactant ions must react with the same type of the substrate, which in our case is CH_3I.

The capture or association rate constant given by parameterized ADO theory is

$$k_c = \left(\frac{2\pi q}{\sqrt{\mu}}\right)\left[\sqrt{\alpha} + c\mu_D\sqrt{\frac{2}{\pi k_B T}}\right] \qquad (3.43)$$

where q is the charge on the ionic reactant in units statcoulomb (statC), μ is the reduced mass of the nucleophile, μ_D and α are the dipole moment and polarizability of the neutral substrate, respectively, and c is the dipole locking factor that has values between 0 and 1. All units in equation 3.43 are CGS. At constant temperature, the value of c depends on the values of dipole moment and polarizability of the substrate. In fact, it is a function of $\mu_D/\alpha^{1/2}$, which has been calculated and tabulated. The ADO theory has been used to predict the dipole dependence of charge transfer [153, 156], proton transfer [157–160], and momentum transfer [161, 162] collisions and proton transfer rate constant [157–160].

The calculated rate constants are found to agree with the experimental rate constant values within 20%. The inclusion of conservation of angular momentum, further bring the calculated rate constants closer to the experimental values [163].

3.4 Electronic structure methods: WF and DFT

Electronic structure methods are approximations to the electronic Schrödinger equation, which is obtained by applying the Born-Oppenheimer approximation and neglecting the mass-polarization term [164]. These methods describe the electronic structure of atoms or molecule and allows for the calculations of energies, structures, and many important molecular properties. Usually, these approximated methods are based on wavefunction (WF) formalisms or on the density functional theory (DFT). When applied to reacting species, electronic structure methods can also provide information about the likely pathways, intermediates and transition states of the reaction. To do this, electronic structure methods take the advantage of the link between the molecular structure

and potential energy surface with statistical theories such as TST and RRKM, or are applied in direct dynamics approaches.

For the electronic structure methods based on WF, the most common approaches start from the molecular orbital (MO) approximation, where the electronic wavefunction is written as a (Slater) determinant of one-electron functions (molecular orbitals) [122, 164].

By applying the variational principle to a trial determinantal wavefunction we obtain a set of N-equations (for a system with N electrons) of effective one-electron known as canonical Hartree-Fock (HF) equations. These integral-differential equations are very difficult to implement in computer programs. Thus, an expansion of the molecular orbitals (one-electron functions) is performed with a known basis sets that leads to the so-called linear combination of atomic orbitals (LCAO) approximation. Again, from the variational principle, a matrix equation (Hartree-Fock-Roothaan-Hall) is obtained that can be promptly solved by computer programs. This is commonly denoted as the Hartree-Fock method (HF). Because of the large computational demand for employing the HF method for large molecular systems, approximations to this method have been proposed and to improve these approximations, parametrizations using known experimental data are performed leading to semiempirical methods.

3.4.1 Semiempirical methods

Semiempirical methods [122, 123, 165–168] (e.g. AM1, PM3, INDO-S) use experimental data such as geometry, enthalpy of formation, dipole moment, ionization energy, excitation energy, oscillator strength, etc. to improve simplifications performed in the HF method. Some common simplifications are: treatment of only the valence electrons with minimal basis sets, zero-differential overlap (ZDO) in many integrals, simplification of electronic integrals by parametrized analytical functions, neglect of the overlap matrix in the HF equations. The various semiempirical methods differ in the ways to approximate and simplify the HF method and the values included in their parameter sets. For instance, AM1 and RM1 methods use the same approximation but they differ in their parameterization, whereas AM1 and PM3 differ in their approximations and parametrization. Semiempirical methods have relatively low computational

demands for a quantum description and they provide a good description of molecular properties at equilibrium geometries. However, they are usually not satisfactory for thermochemical and kinetics calculations and for the conformational analysis [122, 123, 165–168].

3.4.2 HF and MP2

The Hartree-Fock model imposes a separation of the many-electron Schrödinger equation into one-electron equations. Each of these effective one-electron equations can be solved to give molecular orbitals and their corresponding orbital energies. These orbitals describe the behavior of an electron in the average field of the remaining electrons.

The wavefunction of a many-electron system is the function of the positions of all electrons and their spins, namely,

$$\Psi(\vec{r}_1\sigma_1, \vec{r}_2\sigma_2, \cdots, \vec{r}_N\sigma_N)$$

where $(\vec{r}_1, \vec{r}_2, \cdots, \vec{r}_N)$ are the spatial coordinates and $(\sigma_1, \sigma_2, \cdots, \sigma_N)$ are the spin coordinates. This electronic wavefunction must be antisymmetric with respect to the permutations of the electron coordinates.

Now, considering that electron 1 (with spin α) is described by the function (orbital) ψ_a and electron 2 occupies the same orbital ψ_a with spin β and so on, the many-electron wavefunction can be approximated by a Slater determinant,

$$\Psi_{\text{HF}} = \frac{1}{\sqrt{N!}} \begin{vmatrix} \psi_a^\alpha(1) & \psi_a^\beta(1) & \cdots & \cdots & \psi_z^\beta(1) \\ \psi_a^\alpha(2) & \psi_a^\beta(2) & \cdots & \cdots & \psi_z^\beta(2) \\ \vdots & \vdots & & & \vdots \\ \vdots & \vdots & & & \vdots \\ \psi_a^\alpha(N) & \psi_a^\beta(N) & \cdots & \cdots & \psi_z^\beta(N) \end{vmatrix} = \frac{1}{\sqrt{N!}} \left| \psi_a^\alpha(1)\psi_a^\beta(2) \cdots \psi_z^\beta(N) \right|$$

where $1/\sqrt{N!}$ is the normalization factor. This determinantal form of the electronic wavefunction satisfies the antisymmetric properties and the Pauli exclusion principle.

The variational principle states that the energy obtained from a trial (approximated) wavefunction, such as Ψ_{HF}, is stationary with respect all variational parameters, namely, the functions ψ's. In addition, it is imposed that these functions ψ's being orthonormal. Using differential and functional calculus the following set of one-electron equations is obtained by employing the variational principle and orthonormal functions,

$$\hat{f}_i\,\psi_a(i) = \varepsilon_a\,\psi_a(i) \tag{3.45}$$

where $\hat{f}_i$ is the Fock operator. The solutions of the above equations yield ψ_a and ε_a. The Fock operator $\hat{f}_i$ has the following terms,

$$\hat{f}_i = \hat{h}_1 + \hat{V}_{Coulomb} + \hat{V}_{Exchange} \tag{3.46}$$

where $\hat{h}_1$ is the one-electron core Hamiltonian that includes the kinetic energy and the electron-nuclei attraction, $\hat{V}_{Coulomb}$ is the repulsion between electron 1 and the average density of the remaining electrons, and $\hat{V}_{Exchange}$ represents the contribution from the permutations of the electron coordinates. More specifically,

$$\hat{f}_1\,\psi_a(1) = \hat{h}_1\,\psi_a(1) + \sum_{m\,\in\,occ}\{2\hat{J}_m(1) - \hat{K}_m(1)\}\,\psi_a(1) = \varepsilon_a\psi_a(1) \tag{3.47}$$

where the sum spans all the occupied orbitals. This equation reveals the main interpretation of the Hartree-Fock method, that is, the electronic density due to electron 1, $|\psi_a(1)|^2$, is independent of the positions of the remaining electrons. In other words, the electron repulsion is described by interactions between average electronic densities. This is represented by the operators $\hat{J}_m(1)$. The indistinguishability and antisymmetry of the electrons is taken into consideration in the $\hat{K}_m(1)$ operators and thus are a purely quantum effect. Operators $\hat{J}_m(1)$ and $\hat{K}_m(1)$ depend on ψ_i's, the these effective one-electron equations are non-linear and are usually solved iteratively. That is, an initial guess for the orbitals functions $\{\psi_i^{(0)}\}$ is provided and used to build the Fock operator, which after solving the Hartree-Fock equations leads to a new set of orbitals $\{\psi_i^{(1)}\}$ and energies

$\{\varepsilon_i^{(1)}\}$. This process continues until the total energy and the electronic density remain unchanged within threshold values and the self-consistent-field procedure (SCF) is converged [169].

The simplest and least computationally demanding approach to include electron correlation is the Møller-Plesset perturbation theory through second order (MP2) [170]. This method is, in fact, a subset within the many-body perturbation theory (MBPT) formalism as well as the Coupled-Cluster (CC) theory [171]. Another well-known approach is the configuration interaction (CI) method that uses the variational method to determine the best trial wavefunction including excited configurations from a reference state [122, 168]. Second-order Møller-Plesset (MP2) model [172] is the simplest and most widely employed model among the class of Møller-Plesset model (higher-order MP3, MP4 and MP5) and the correlated methods. Møller-Plesset methods are size-extensive, but are not variational. Therefore, it is generally preferred over truncated CI models, which are variational, but not size-extensive, to study chemical reactions. MP2 models generally provide excellent results when employed to investigate the equilibrium and transition state structures, conformations and thermochemistry of reactions [122].

Higher order Møller-Plesset models MP3, MP4 and MP5 and CC methods such as CCSD, CCSD(T), CCSDTQ have been developed [173–176], but are limited to very small systems due to their high computational costs. Moreover, first and second analytical derivatives may be not available for these high correlated methods, which hinder their application. The accuracy of various computational methods in combination with the basis sets is illustrated in Figure 3.5 for the calculations of bond distances.

It can be seen from the figure 3.5 that the HF model underestimate the bond distances and have a broader distribution away from the origin even at higher levels of basis set. The Møller-Plesset models, in contrast, present sharper distributions closer to the origin. The MP2 performs better than MP3 and MP4 for medium size basis sets. The improvement of basis sets improves the performance of MP4 model, but considering the cost of MP4 model the improvement in the performance is rather unsatisfactory. The CCSD and CISD distributions are well away from the origin and improving basis sets does not improve the performance significantly. Therefore, CCSD and CISD models are not well suited for the bond length calculations.

However, the inclusion of perturbative triples to the CCSD, that is, CCSD(T), yields excellent results with cc-pVTZ and cc-pVQZ basis sets. The model performs extremely well with sharp distributions close to the origin at higher levels of the basis sets [164] and are considered as the state-of-art in electronic structure calculations.
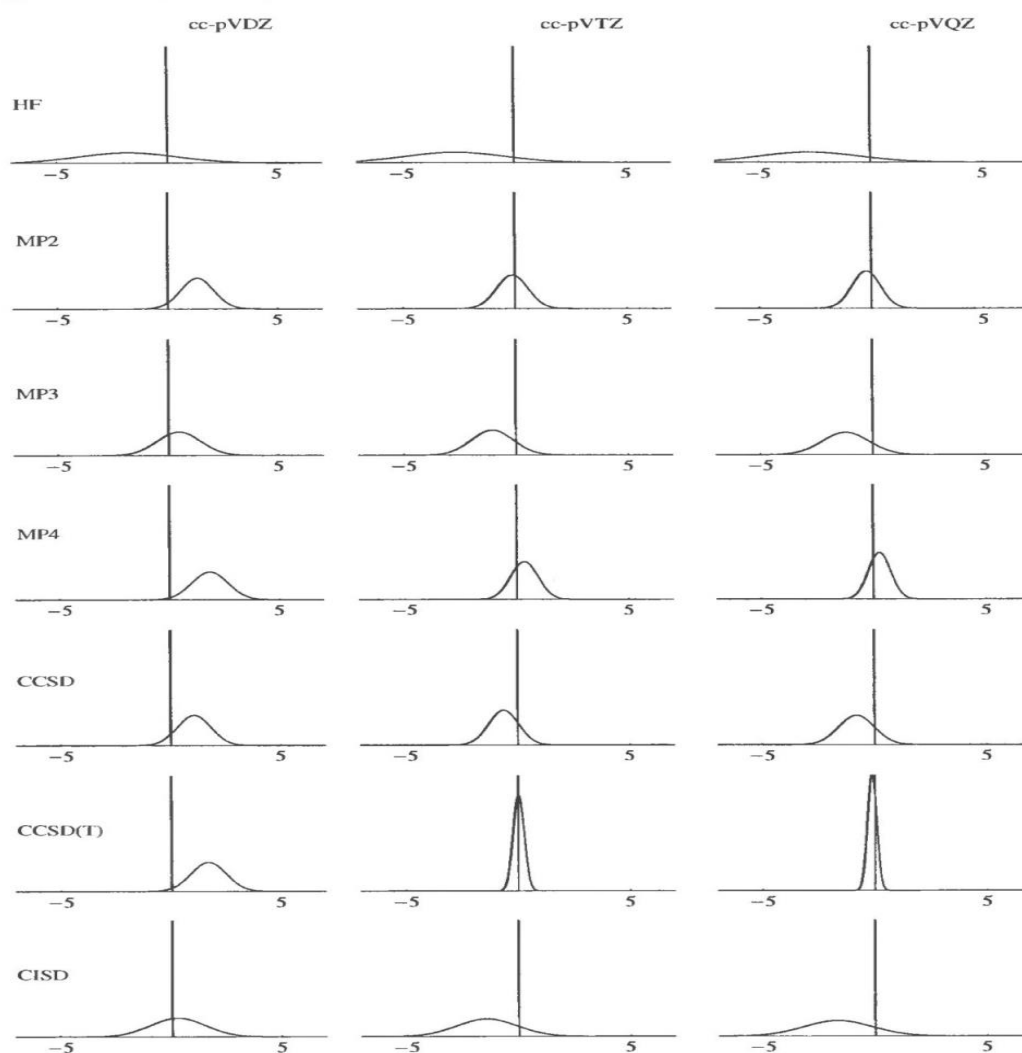

Figure 3.5 Normal distribution of errors in the calculated bond distances (pm). All the distributions have been normalized to one and plotted against the same horizontal and vertical axis. Figure adapted from reference [164].

There have been formulations of MP2 models based on localized orbitals instead of the canonical molecular orbitals, which allows for treatment of larger molecular systems. They are useful for

large systems as they reduce the number of integrals needed to be calculated and processed. This reduces the computational demand in terms of memory and CPU requirements.

The performance of the different quantum chemical methods also depends on the basis sets used. Basis sets are mathematical descriptions of atomic orbitals, often called basis functions. Molecular orbitals are approximated as linear combinations of atomic orbitals (basis functions) and are referred as linear combination of atomic orbitals (LCAO). These basis functions describe the shape of electron density in the atoms and when combined they describe the electron distribution in the molecule as a whole. Thus, these basis functions have to be flexible to also describe the electron densities between atoms that give rise to chemical bonds and their changes. Now, basis functions can be any set of atomic orbitals and they can be manipulated to represent the molecular orbitals in a useful way. Most implementations of quantum chemical methods use Gaussian-type functions because they provide closed forms for the molecular integrals [177, 178]. The different combinations of basis sets and the methods lead to different results. Figure 3.6 represents a two-dimensional diagram illustrating the performance of different combinations of basis sets and theoretical models.
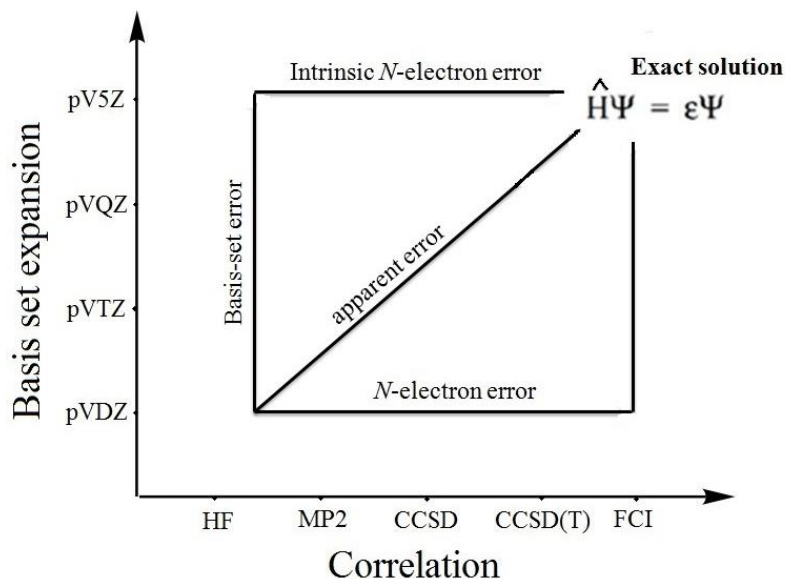
Figure 3.6 The performance of different combinations of basis sets and theoretical models. Figure adapted from reference [164], with some modification.

The horizontal axis represents the extent of correlation among electron in a many-electron system. The correlation increases as we move from the HF models at extreme left to the full configuration interaction (FCI) models that provide the exact electronic energy for a given basis set on the extreme right. The correlated models of most practical use lie somewhere in between. The vertical axis represents the completeness of the basis sets. The exact solution of Schrödinger equation lies at the top right corner, namely, a combination of a fully correlated model and a complete basis set. However, because these exact solutions are unattainable for most molecular systems, the convergence of the properties of interest with the level of correlation and the basis sets is important. Benchmark studies and statistical analysis help to guide the choice of the adequate electronic structure method based on wavefunction formalism. This characterizes another requirement for a method to be called ab initio.

Alternative approaches to the wavefunction based methods are approximations to the density functional theory (DFT) mostly based on the Kohn-Sham formulation.

3.4.3 Density functional theory based methods

Correlated wavefunction based models employ virtual (unoccupied) molecular orbitals that leads to very demanding and cumbersome methods. The construction of the Hamiltonian operator depends on the position and total number of electron in a system. The dependence of the Hamiltonian on the total number of electrons suggests that the electron density can be a useful observable which when integrated over all the space gives the total number of electrons N, that is,

$$N = \int \rho(\boldsymbol{r})\mathrm{d}\boldsymbol{r}$$

Thus, density functional methods use electron density function rather than wave function. Unlike the wave function, the electron density is a measureable feature, e.g. by X-ray or electron diffraction. The electron density is a function of position only, that is, it depend only on three variables, x, y, z, no matter how large is the molecule, while the wave function of N electrons is a function of $4N$ or $3N$ variables if we do or do not include the spin coordinates [179]. Therefore,

density functional theory is conceptually different from the wavefunction based techniques as it uses the electron density instead of wave function to describe the electron distribution. The theory is based on the Hohenberg-Kohn theorem [180], which states that the ground state energies can be determined from the electron density, $\rho(\boldsymbol{r})$, where $\boldsymbol{r}$ represents the position vector in space.

Kohn and Sham in 1965 introduced a fictitious system of N independent electrons that has the same density as the real system [181]. For an independent electron system, the electronic kinetic energy, the average electronic repulsion (Coulomb) energy, and the electron-nuclei attraction energy can be calculated exactly. The remaining terms of the exact energy of a real electronic system, namely, the kinetic energy correction for non-independent electrons, electronic exchange and correlation effects, are included in the so-called exchange-correlation contribution. Thus, in the Kohn-Sham formulation the ground state energy, $E[\rho(\boldsymbol{r})]$, is expressed as a sum of the kinetic energy of independent electrons, $E_{\mathrm{k}}[\rho(\boldsymbol{r})]$, the electron-nuclear attraction energy, $E_{\mathrm{ne}}[\rho(\boldsymbol{r})]$, the average (Coulomb) electron-electron repulsion, $E_{ee}[\rho(\boldsymbol{r})]$, and the exchange-correlation energy, $E_{XC}[\rho(\boldsymbol{r})]$:

$$E[\rho(\boldsymbol{r})] = E_{\mathrm{ni}}[\rho(\boldsymbol{r})] + E_{\mathrm{ne}}[\rho(\boldsymbol{r})] + E_{ee}[\rho(\boldsymbol{r})] + E_{XC}[\rho(\boldsymbol{r})] \tag{3.48}$$

As a result of the independent electron treatment, the electron density can be written in terms of the occupied Kohn-Sham orbitals, $\phi_i(\boldsymbol{r})$, as,

$$\rho(\boldsymbol{r}) = \sum_i^N |\phi_i(\boldsymbol{r})|^2$$

Writing the functional in terms of the density built from the Kohn-Sham orbitals and applying the variational theorem to the equation 3.48, the Kohn-Sham equations are obtained

$$\left[-\frac{1}{2}\nabla_i^2 + \sum_{k=1}^{N_{nuclei}} \frac{Z_k}{|\boldsymbol{r}_i - \boldsymbol{r}_k|} + \int \frac{\rho(\boldsymbol{r}')}{|\boldsymbol{r}_i - \boldsymbol{r}'|}\,\mathrm{d}\boldsymbol{r}' + V_{XC}(\boldsymbol{r}) \right]\phi_i(\boldsymbol{r}) = \varepsilon_i\phi_i(\boldsymbol{r}) \tag{3.49}$$

$$V_{XC}(\boldsymbol{r}) = \frac{\delta E_{XC}(\rho)}{\delta \rho} \qquad (3.50)$$

The potential $V_{XC}(\boldsymbol{r})$ is the functional derivative of the exchange-correlation energy. Thus, solution of Kohn-Sham equation requires an exchange-correlation energy functional, whose exact form is unknown. Therefore, approximate functionals are used given rise to density functional approximations or DFAs [182]. Indeed, a continuous progress of DFA has been achieved and is based on the efforts to improve the approximation to $E_{XC}(\rho)$. Different functionals have been developed over time based on different approximations that include the local density approximation (LDA), the generalized gradient approximation (GGA), shape-corrected pure functional such as SAOP [183], amongst others.

Thus, DFT is a high-level technique that accounts for a large part of the correlation energy [184] without incorporating configuration interaction (CI) expansion. Density functional methods are, therefore, faster and computationally less expensive than wavefunction based *ab initio* methods. They are proven to be successful for determination of geometries and conformations of both the equilibrium and excited states. It is also easier to include the solvent effects [185]. They are (nearly) as successful as MP2 models for establishing the thermochemistry of reactions where single bonds are broken or formed. Density functional models, like the Hartree-Fock method, are applicable to molecules of moderate size and they are not significantly more costly than Hartree-Fock.

The adiabatic connection method formalized the inclusion of (partial) exchange energy from Hartree-Fock into the exchange functional leading to highly improved global hybrid density functional models such as the most widely used B3LYP functional [178]. Using the same approach for the correction energy, double-hybrid functionals, which include (partial) MP2 correlation energy, have developed and are shown to be highly successful, despite the larger computational demand.

3.5 Models and Treatments of Solvent Effects

Quantum chemical calculations of the free-energy of a system containing a solute and a number of solvent molecules large enough to simulate the solvent effects require the statistical treatment of many millions of configurations of this system that makes impractical the full quantum mechanical treatment of such large systems. One therefore would seek, in general, the use of model systems referred as solvation models, that is, the simplified expressions describing the relevant interactions allowing easy derivations of molecular distribution functions or statistical simulations [186, 187].

An ideal model is, therefore, the one that describes as accurate as possible solute-solvent and solvent-solvent interactions. Such models provide much better predictions and understanding of chemical processes occurring in solutions. Every solvent model has several advantages and limitations. They can broadly be divided into three classes: explicit or discrete models, that is, those describing the individual solvent molecules explicitly in the system, implicit or continuum models that treat the solvent as a (polarizable) continuum dielectrics, and discrete-continuum models that describe the solute and a few solvent molecules explicitly, which is embedded into a (polarizable) continuum dielectrics. In addition, discrete models can be described by hybrid or mixed quantum mechanics and molecular mechanics (QM/MM) treatments [188].

3.5.1 Explicit Models

A rigorously correct way to simulate the solvent effects would be to add all the solvent molecules explicitly in the surrounding of the solute and then perform statistical mechanics computational simulations with e.g. Monte Carlo or molecular dynamics techniques using molecular mechanics force fields or quantum potentials. However, this is nontrivial and requires large computational resources. In explicit solvent models, the solute-solvent and solvent-solvent interactions need to be averaged over relatively long times or very many configurations in order to provide meaningful results. Currently, there are not sufficient computational resources to compute the quantum dynamics studies of systems of interest in solutions. There have been a few studies conducted in an effort to reduce the computational cost where a smaller numbers of optimized

solvent molecules each starting from a different geometry were added in the surrounding. The obtained results can then be weighted by Boltzmann distribution. This requires less computation time, but the accuracy of the results may also be affected. Some new generation of polarizable force fields are being developed that can account to changes in the molecular charge distribution and charge anisotropy the molecule [122, 187, 189]. Although, the discrete models are computationally expensive, there are many cases where a detailed description of the specific solute-solvent interactions is important and thus the explicit representation of solvent molecules is required. For instance, systems containing hydrogen bonds probably cannot be properly described by implicit solvent models because they do not account for the specific solute-solvent hydrogen bonding.

An important treatment using discrete models is based on hybrid or combined quantum chemical and molecular mechanics force field methods, namely, QM/MM approach. More specifically, one can set up computationally efficient approaches by limiting the quantum mechanical (QM) treatment to the solute and a few solvent molecules. The remaining solvent molecules describing properly the macroscopic behavior are treated by molecular mechanics (MM) using some classical force-fields. Alternatively, these MM solvent molecules can be limited to a few solvation shells and the discrete QM/MM system embedded into a (polarizable) continuum medium [190]. The computations of statistical average can then be performed, for instance, by Monte Carlo or molecular dynamics methods. The hybrid QM/MM approach [188] allows the study of chemical processes in solutions and in proteins by combining the strengths of QM (accuracy) and MM (efficiency) approaches. The Hamiltonian can be written as

$$H_{\text{QM/MM}}^{\text{sol}} = H_{\text{QM}} + H_{\text{MM}} + H_{\text{QM/MM}}$$

where H_{QM} is the quantum Hamiltonian for the solute; H_{MM} is the classical Hamiltonian for solvent molecules, and $H_{\text{QM/MM}}$ describes to the interaction energy term between the quantum solute and the classical solvent molecules. This interaction Hamiltonian, $H_{\text{QM/MM}}$, is not uniquely defined and usually it involves a sum of the van der Waals interaction energies among the quantum solute atoms and the classical solvent atoms, of the long-range electrostatic interactions,

of the electron distribution, of the nuclei of the solute and of possible presence of hydrogen bonds.

QM/MM solvation approaches provide results with a good level of accuracy and they are currently widely used to refine and to study the molecular structure and reactivity in solutions and in enzymes [191]. They are, however, difficult to apply efficiently to describe the reactivity in the systems where one or more solvent molecule are directly involved in the reaction mechanism [192]. One solution to this problem is to choose the unique solvent molecule that will react with the solute among all the other solvent molecules [193, 194].

3.5.2 Implicit Models

In implicit models, one assumes that the explicit solvent molecules can be replaced by a (polarizable) continuum medium described by its dielectric constant surrounding the solute contained in a cavity [195]. In another words, the solute placed in a cavity, which is embedded in a (polarizable) continuum describing the solvent, where the solute charge distribution interacts with the continuous dielectric field at the surface of cavity, which causes a change in the polarization of the solute called reaction field. Mathematically, the free-energy of solvation ($\Delta_{\mathrm{sol}}G$) described by implicit models can be written as,

$$\Delta_{\mathrm{sol}}G = \Delta_{\mathrm{pol}}G + \Delta_{\mathrm{cav}}G + \Delta_{\mathrm{vdW}}G$$

where, $\Delta_{\mathrm{pol}}G$ is the free-energy contribution of the solute-solvent electrostatic polarization, $\Delta_{\mathrm{cav}}G$ is the free-energy term related to the formation of a cavity within the solvent, and $\Delta_{\mathrm{vdW}}G$ is the solute-solvent van der Waals (or dispersion) interactions. The implicit models are computationally less demanding as the number of degrees of freedom is reduced to roughly one order of the magnitude that reduces the computational time [196]. The most widely used implicit model is the polarizable continuum model (PCM) [186], which is available for calculations of energy, gradient and Hessian with Hartree-Fock and DFT methods in several quantum chemical packages such as Gaussian and GAMESS. There are various types of implicit models such as accessible surface areas (ASA), which are historically the first continuum models [197]. In ASA models the solvation energy is calculated as a linear relationship between the surface area of the

solute molecules and the Gibbs free energy of transfer. The other major types of implicit models are the Poisson-Boltzmann [198] and generalized Born approximation model [199]. The former is based on the exact self-consistent treatment of electrostatic interaction in the continuous solvent medium. The generalized Born approximation method is based on the Poisson-Boltzmann equation, where the consistent solution to the electrostatic potential is replaced by an approximate calculation of the solvent-induced reaction field energy.

The most relevant property of the PCM models is the cavity of the solute. There are several approaches to construct the cavity that will contain the solute molecule such as the atomic radii of atoms and/or groups constituting the solute or the electronic density isosurface of the solute. The most commonly used approaches that parametrize the atomic radii to reproduce solvation energies are the UAO, UAHF, UAKS, UFF, Pauling and Bondi cavities. The UAO cavity is built up using the united atom topological model (UATM) [200] applied on the atomic radii of universal force field (UFF). The UAO model is implemented as default in the Gaussian 03 program, whereas the Gaussian 09 program uses by default the radii from UFF force field scaled by 1.1. The UAHF and UAKS [201] cavities use the UATM model [200] with radii optimized from HF/6-31G* and PBE0/6-31* calculations, respectively, to reproduce experimental solvation energies. In the Pauling and Bondi cavity approaches, each solute atom or group of atoms is assigned van der Waals values provided by Pauling [202] and Bondi atomic radii [203].

UAHF and UAKS have been shown to provide solvation energies with good accuracy, but have not yet reached the accuracy of experimental data for neutral molecules and ions [204–206]. Whereas the Pauling cavity approach has been shown to provide solvation energies comparable to experiments for the anions, but yielded worse results for neutral molecules [207].

Another relevant technical aspect of the PCM models is the discretization of the cavity surface to generate the apparent charges representing the polarization of the dielectric medium. These charges are generally obtained by solving the integral equation describing the boundary of the cavity which hosts the solute molecules. The solution to these equations requires the discretization of the molecule-solvent boundary to a finite number of small elements. The

solution to these equations is an evaluation of various contributing quantities such as cavitation, electrostatic, repulsion and dispersion, determining the solvent reaction field [208].

3.6 Computational Procedures

All electronic structure calculations were performed with the Gaussian 09 program [209] using its default criteria. Molecular structures were determined without symmetry constrains with the MP2 [178, 210] method using aug-cc-pVDZ-PP and aug-cc-pVTZ-PP basis sets [211–214]. The extrapolation to the complete basis set (CBS) limit was performed from MP2/aug-cc-pVXZ-PP (X = D, T, and Q) energy calculations [215, 216].

All equilibrium structures were obtained without constraints, except relax scans of reaction coordinates. The nature of the stationary points on the potential energy surface were characterized by their force constants, where all positive force constants corresponds to minimum and all but one positive force constants represents saddle points. The transition states have also been ascertained by intrinsic reaction coordinate (IRC) calculations, which connect the transition state to the reactant(s) and the product(s) through the minimum energy path.

All the stationary points have been characterized by vibrational analysis. Once a stationary point is found, it is necessary to check whether it is a minimum, a transition state (first-order saddle point) or a higher-order saddle point. This can be done by calculating the force constant of each $3N - 6$ vibrational mode for nonlinear molecules and the corresponding vibrational frequency under the harmonic approximation,

$$k_\alpha = \frac{\partial^2 E}{\partial Q_\alpha^2} \quad \text{and} \quad \nu_\alpha = \frac{1}{2\pi}\sqrt{\frac{k_\alpha}{m_\alpha}} \tag{4.1}$$

where for the α-mode, k_α is the force constant, E the total energy, Q_α the normal mode, ν_α the frequency, and m_α the reduced mass.

Thermochemical properties were calculated within the rigid-rotor and harmonic oscillator approximations for ideal gas using standard pressure at 298 K [217]. The equilibrium structures were visualized and analyzed with the GaussView [218] and Chemcraft [219] programs.

The capture rate constant for the formation of ion-dipole complex, k_{ADO}, has been calculated using the ADO theory [36, 37]. The theory uses the dipole moment and polarizability of the neutral reactant, that is, CH_3I in our case, and charge and reduced mass of the ionic reactant (nuleophile). The capture rate constant is given by

$$k_{\text{ADO}} = \frac{2\pi q}{\sqrt{\mu}}\left[\sqrt{\alpha} + c\mu_D\sqrt{\frac{2}{\pi k_{\text{B}}T}}\right]$$

where q and μ are the charge in units statcoulomb (statC) and the reduced mass of the nucleophile, respectively, μ_D and α are the dipole moment and polarizability of the neutral substrate, that is, CH_3I, c is the dipole locking factor that has values between 0 and 1 and it is a function of $\mu_D/\alpha^{1/2}$. Thus, it may be obtained from tables or plots of c and $\mu_D/\alpha^{1/2}$.

The unimolecular reaction rates from the reactant complexes to the product complexes were calculated with the RRKM theory [132, 133, 138, 220] using the superRRKM [221] program for energy values E from E_0 to $E_0 + E_{\text{thermal}}$ (at 298 K). The initial value E_0 was taken as the complexation energy of reactant complex. The RRKM rate constants $k_a(E)$ were weighted by a Boltzmann distribution and integrated from E_0 to $E_0 + E_{\text{thermal}}$ to yield the canonical rate constant at 298 K [138]. The program uses the Beyer-Swinehart (BS) algorithm [222, 223] to calculate the density of state $N(E)$ and the sum of state $G^{\ddagger}(E - E_0)$ by *directly counting* all states. The algorithm uses the vibrational frequencies, rotational partition functions of the reactants and the transition state, zero-point energy of the transition state and total zero-point energy available to the reactants. The calculations of the rate constant have been carried out over the range of the energy from E_0 (zero-point energy of the transition state) to the total available

zero-point energy for the reactants plus the thermal energy. The RRKM rate constant is calculated as

$$k_{\mathrm{RRKM}}(E) = \sigma \frac{G^{\ddagger}(E - E_0)}{hN(E)}$$

where σ is the reaction degeneracy which has value 1 and 2 for $S_N2@C$ and $S_N2@O$ (for symmetric nucleophiles), respectively. $G^{\ddagger}(E - E_0)$ represents the number of states available at transition state from 0 to $E - E_0$ and $N(E)$ is the density of states of the reactants at total internal energy E. E_0 is the zero-point activation energy, that is, the minimum energy value at which the rate constant has minimum nonzero value.

The rate equations for the complete chemical kinetics scheme were solved numerically by a fourth-order Runge-Kutta method with an adaptive integration step [224]. The concentrations of each species are provided by these calculations starting with a concentration for the reactants (organic substrate and nucleophile) compatible with the experimental setup and null concentrations for the remaining components.

Solvent effects were simulated with the standard Polarizable Continuum Model (PCM) [186] and radii derived from the UFF approach employing the CPCM implementation in the Gaussian 09 program. The solute cavity was determined using UFF radii approach implemented as default in the Gaussian 09 program. The method places the spheres around each solute atom with a radii scaled by a factor of 1.1 to determine the solute cavity.

The dielectric constant 8.93 and 37.219 were used for solvent dichloromethane (DCM) and N,N-dimethylformamide (DMF) , respectively, to simulate the solvent environment.

Chapter 4

Alkylation of nitronates in the gas-phase

4.1 General results

Gas-phase S_N2 reactions have been widely explored by computational methods and benchmark assessment studies have shown that the MP2 method with large basis set is the most suitable for kinetics simulations [225–233], whereas DFT-based methods have performances that may depend upon the particular system [35, 233]. Calculations of the enthalpies of deprotonation of nitroalkanes [71] and the vibrational frequencies of CH_3NO_2 were compared with the experimental values [234, 235] to ascertain the reliability of MP2 and DFT methods (Tables A1 and A2 in Appendix). Indeed, the overall results provided by the MP2 method with medium to large basis sets are in excellent agreement with the experiment. However, systematic calculations (Tables 4.1 and 4.2) of the activation energies of $[R^1R^2CNO_2]^- + CH_3I$ reactions, especially the difference between the nucleophilic replacement through the carbon and the oxygen atoms, showed a strong dependence with the basis set employed. Thus, the energies of the stationary structures of the reaction profiles were extrapolated to the complete basis set limit (CBS) to provide accurate results for kinetics calculations using the RRKM theory. We have also provided comparisons with selected DFT functionals.

The deprotonation of nitroalkane results in a negative charge on the carbon atom, which acts as a nucleophile to proceed through a S_N2 reaction mechanism, denoted as $S_N2@C$ (C-methylation). On the other hand, because of deprotonation, the nitroalkane flattens into a classic sp^2 hybridized system that allows the delocalization of the negative charge on the oxygen atoms of the nitro group as illustrated in Figure 4.1 through the resonance hybrids (I), (II) and (III).
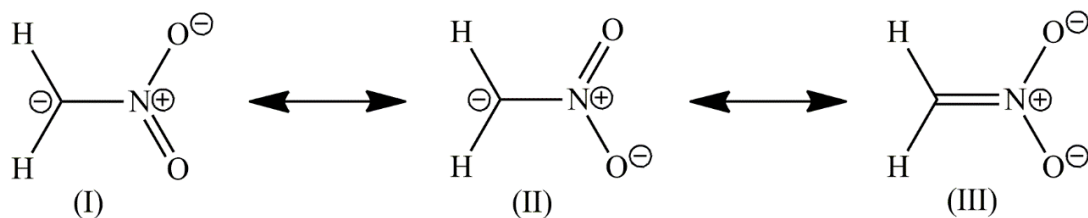
Figure 4.1. Resonance structures of the deprotonated nitromethane, the possible nucleophiles.

Both oxygen atoms of the nitro group may act as a nucleophile to give a S_N2 mechanism, denoted as $S_N2@O$ (O-methylation). For asymmetric nitroalkanes, such as nitroethane (**2**), the displacement may be through the oxygen atom in *syn* or *anti* relative position to the asymmetric group of substituted nitroalkanes. The double bond between carbon and nitrogen in (III) ensures that the internal rotation around the C–N bond is restricted. The bimolecular displacements at iodomethane or methyl iodide (CH_3I) were studied with the following deprotonated nitroalkanes: nitromethane $[H_2CNO_2]^-$ (**1**), nitroethane $[(CH_3)HCNO_2]^-$ (**2**), 2-nitropropane $[(CH_3)_2CNO_2]^-$ (**3**), and nitrocyclopropane $[c\text{-}(CH_2)_2CNO_2]^-$ (**4**) depicted in Figure 4.2.
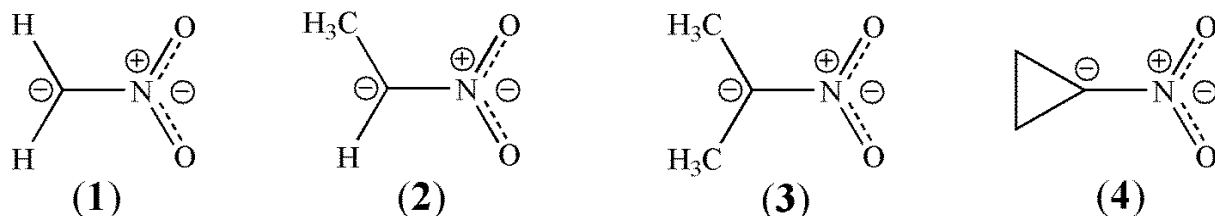
Figure 4.2. Chemical structures of four deprotonated nitroalkanes (nucleophiles): nitromethane (**1**), nitroethane (**2**), 2-nitropropane (**3**), and nitrocyclopropane (**4**).

The energy difference between the transition state (activated complex) and the reactant complex corrected for zero-point (ZP) energy is taken as the energy of activation ($\Delta^{\ddagger}E$) that can be employed in the RRKM or TST expressions for the reaction rates. The energy difference between the separated reactants and the separated products yields the free energy of the reaction ($\Delta_r E$). Table 4.2 represents the calculated values of these quantities for the reactions of CH_3I with deprotonated nitromethane, nitroethane, 2-nitropropane and cyclonitropropane in gas phase at different theoretical levels. The geometries of different optimized structures at MP2/aug-cc-pVDZ level are presented in Figures 4.3–4.6. The corresponding energy profiles for the reaction pathways are shown in Figures 4.9–4.12. Harmonic vibrational frequencies of various transition state found are presented in Table 4.1.

4.2 Molecular Structures

The optimized molecular geometries of various intermediates, transition states, and products calculated at MP2/aug-cc-pVDZ level are presented in Figures 4.3–4.6. The experimental value of C–I bond length of iodomethane obtained from microwave spectrum is 2.136 Å [236]. The calculated C–I bond length in the iodomethane is slightly longer (0.03 Å on average) in the reactant ion-dipole complexes (RC@C and RC@O). This implies that the bond between central carbon and the leaving group starts cleaving with the entrance of the nucleophile. As the nucleophile approaches the substrate, the C–I bond starts lengthening and the bond between nucleophilic carbon (or oxygen) and the substrate carbon starts being formed, leading to the transition state structure. The calculated C–I bond length in the transition state structures, TS@C, of all the reactions is found to be 2.37 Å on average. The same bond length in TS@O is found to be 2.545 Å on average in all the reactions. Thus, the C–I bond length is calculated to be 0.175 Å longer in TS@O than in TS@C, which makes the TS@O a late transition state than TS@C, because the former resembles more the product. Table A3 in the Appendix presents the C–I bond length in isolated Iodomethane calculated at different theoretical levels. The C–C single bond distance is 0.067 Å on average than the C–O bond formed in the product complexes, which also indicates that TS@C is an earlier transition state compared to TS@O. The newly formed bonds (C–C and C–O) are also longer in the product complex than it is in separated product, which reveals the interaction effect of the leaving group. This is mainly because in the optimized structures of the product complexes, the leaving group (I^-) stays near the methyl group of the product and interacts with it (Figures 4.4–4.6).

The negative charge in the nucleophile is delocalized and results in a partial double bond character of the C–N bond. The evidence came from the large values of barrier to internal rotation, that is, 120.8, 139.2, 131.3 and 55.1 kJ/mol for $[H_2C–NO_2]^-$, $[(CH_3)HC–NO_2]^-$, $[(CH_3)_2C–NO_2]^-$, and $[c-(CH_2)_2C–NO_2]^-$, respectively, as compared to those calculated for neutral species $H_3C–NO_2$, $(CH_3)H_2C–NO_2$, $(CH_3)_2HC–NO_2$, and $c-(CH_2)_2HC–NO_2$, namely, 0.0, 1.0, 5.25 and 18.38 kJ/mol at MP2/DZ level. The lowest C–N double bond character is found in $[c-(CH_2)_2C–NO_2]^-$ while the highest of it is found in $[(CH_3)HC–NO_2]^-$. The small internal rotation barrier in $[c-(CH_2)_2C–NO_2]^-$ suggests a large sp^3 character of C–N bond.

As the nucleophile approaches the substrate, a new bond starts to form between nucleophilic carbon and the carbon of the substrate (C-methylation). As a result, the C–N bond lengthens and both N–O bonds shorten. A similar effect was also observed in nucleophilic reaction through the oxygen atoms (O-methylation), where the electron density on the N–O bond of the nucleophilic oxygen moves to the new bond being formed. As a result, the N–O bond lengthens and the other N–O bond shortens.
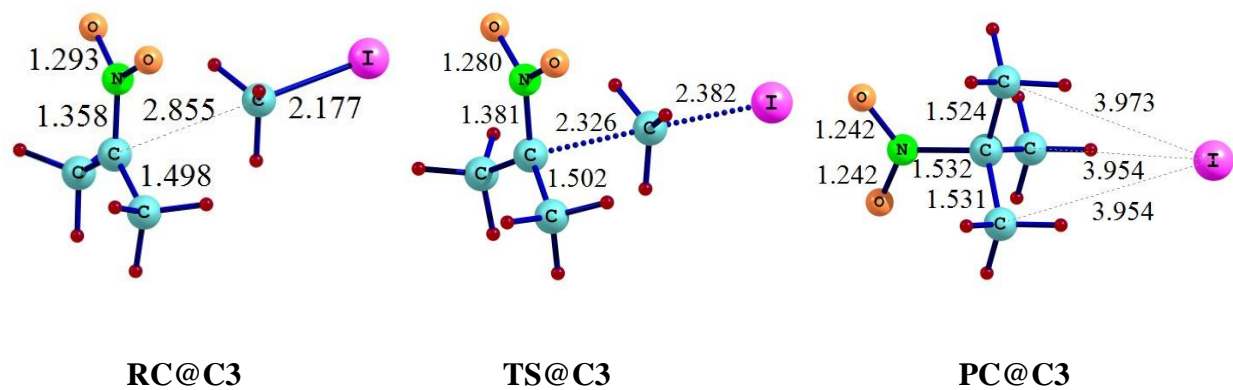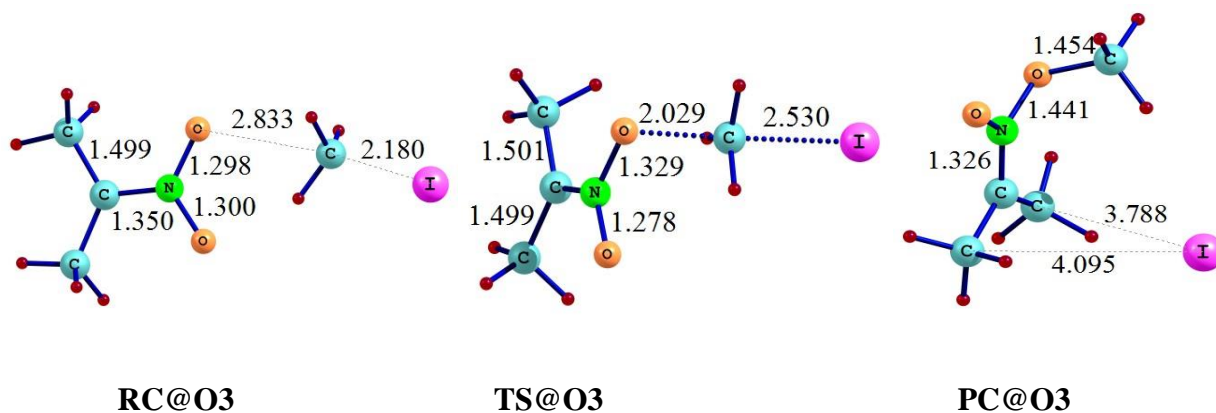

RC@C1   **TS@C1**   **PC@C1**

RC@O1   **TS@O1**   **PC@O1**
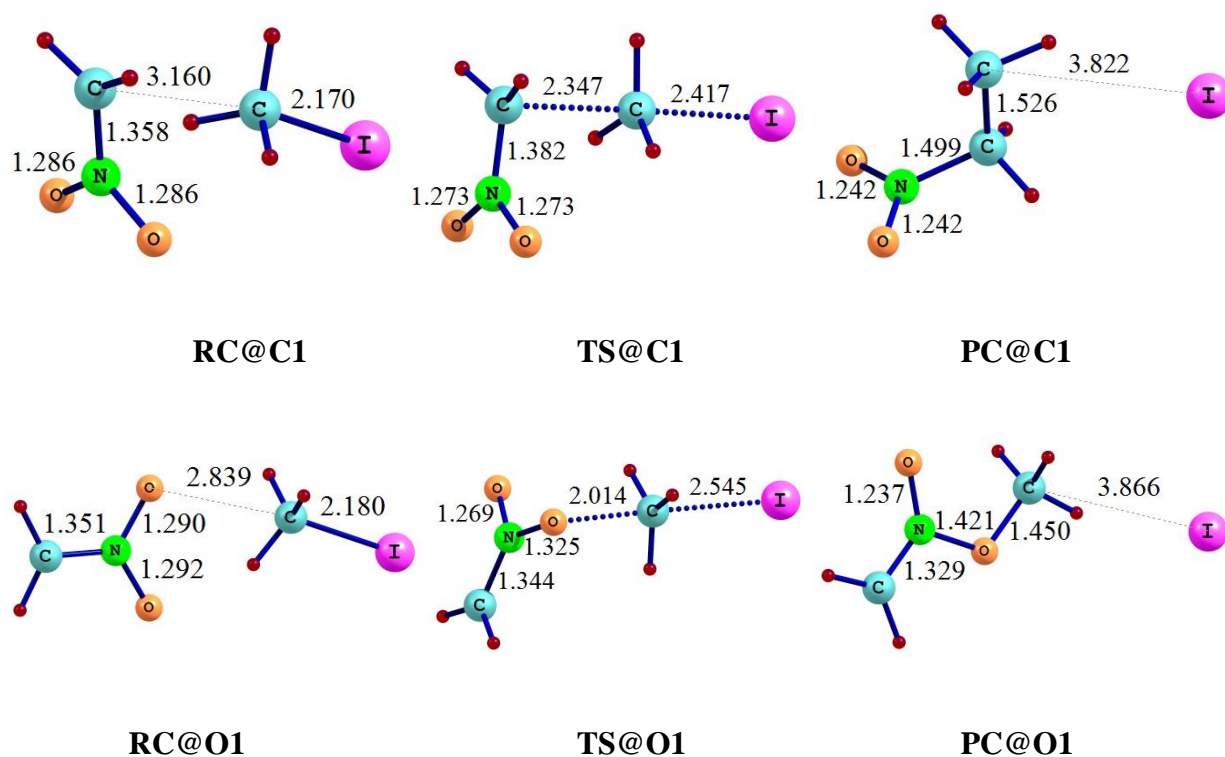
Figure 4.3. Equilibrium structures along the reaction path for S_N2 reaction of $[CH_2NO_2]^-$ + CH_3I computed at MP2/aug-cc-pVDZ level.
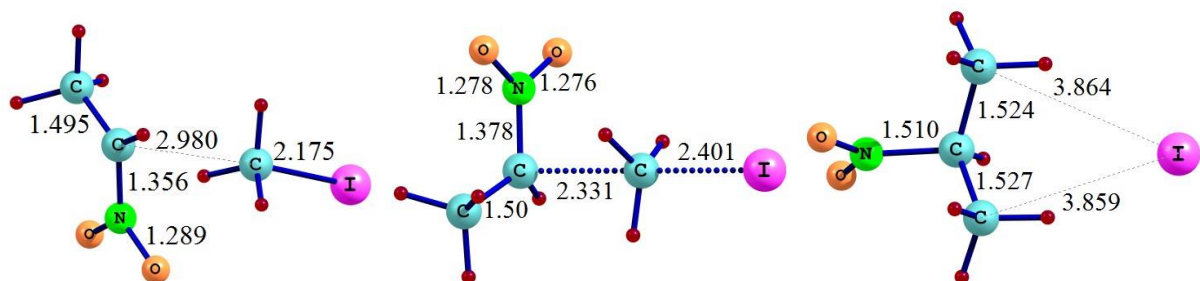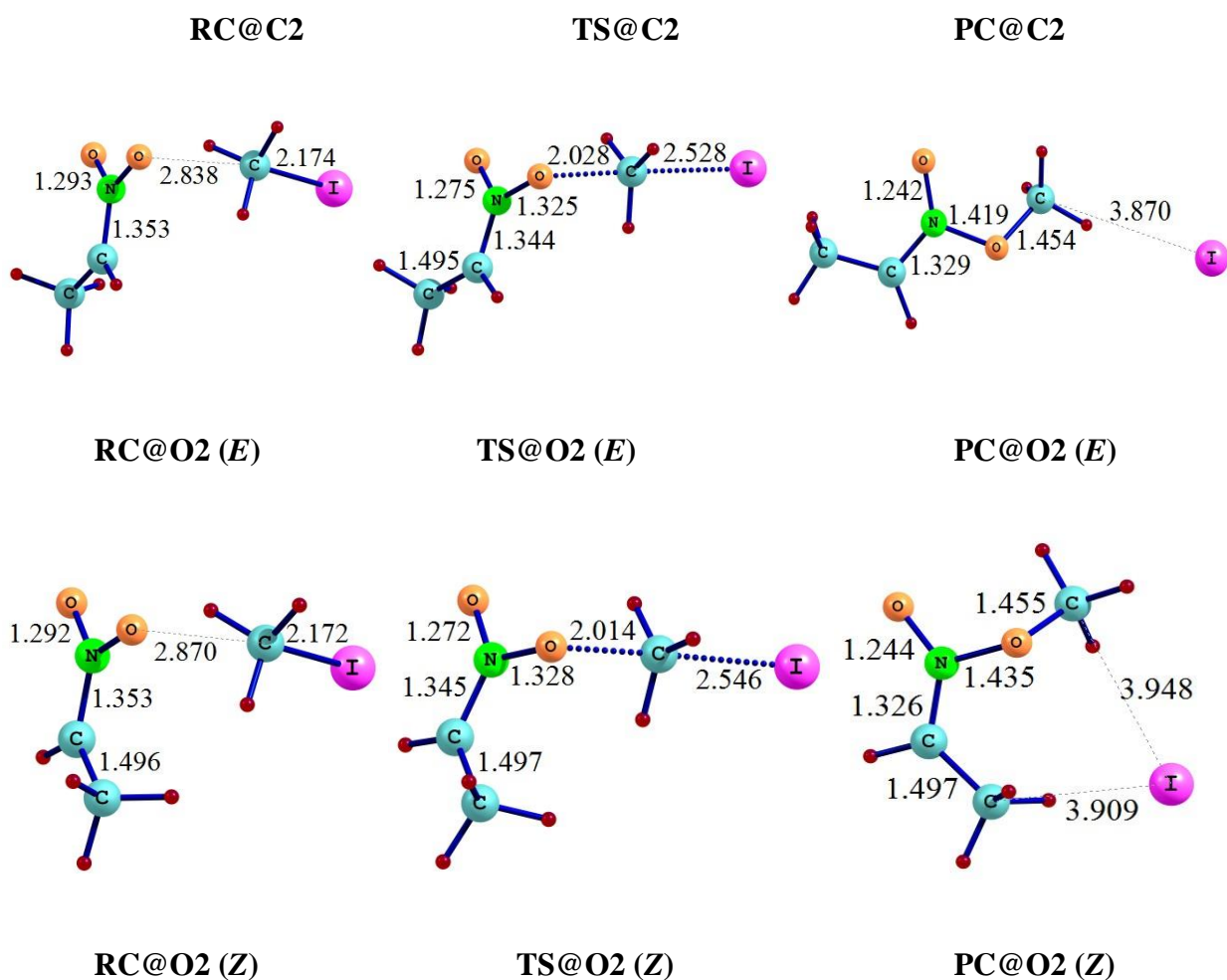
Figure 4.4. Equilibrium structures along the reaction path for S_N2 reaction of $[CH_3CHNO_2]^-$ + CH_3I computed at MP2/aug-cc-pVDZ.

Figure 4.5. Equilibrium structures along the reaction path for S_N2 reaction of $[(CH_3)_2CNO_2]^-$ + CH_3I computed at MP2/aug-cc-pVDZ.
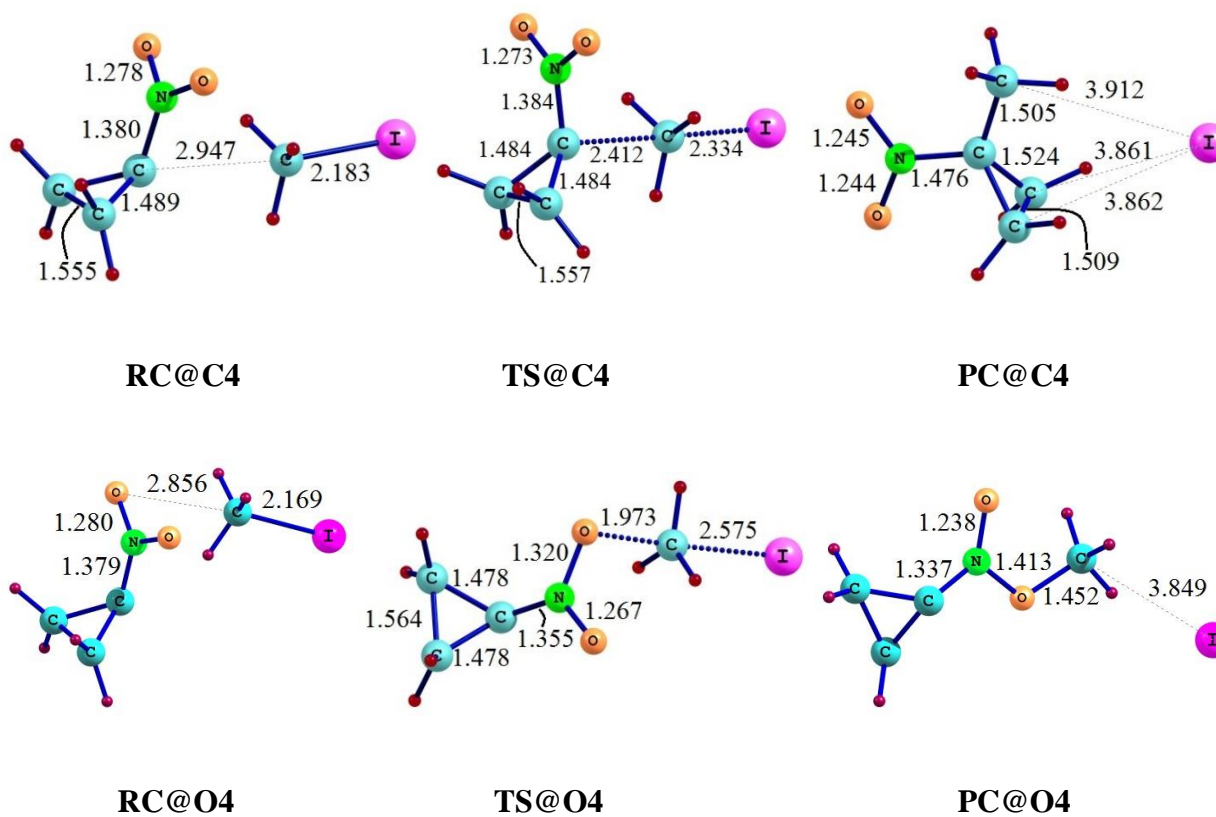
Figure 4.6. Equilibrium structures along the reaction path for S_N2 reaction of c-$[(CH_2)_2CNO_2]^-$ + CH_3I computed at MP2/aug-cc-pVDZ.
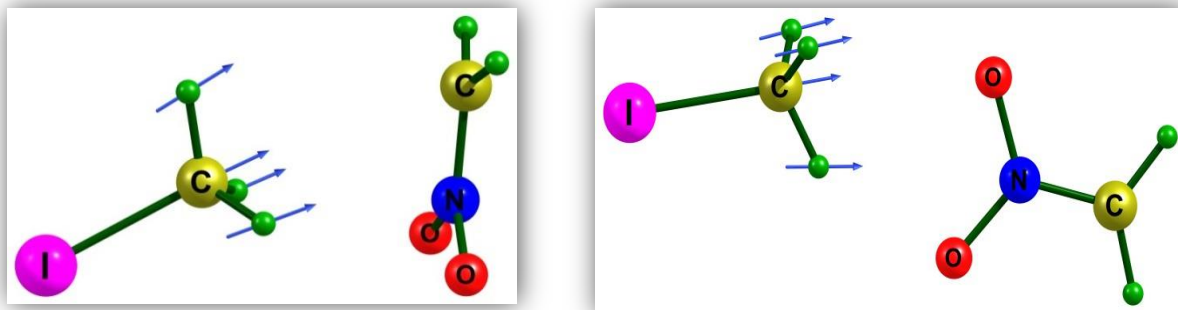
4.3 Vibrational frequencies

A minimum on the potential energy surface is characterized by all positive force constants, that is, positive second derivatives of the energy. Thus, there exists a restoring force for each vibration as in case of a spring when the force constant is positive. A transition state is a first-order saddle-point that has one negative force constant along the reaction coordinate and the remaining force constants are all positive. The motion along this vibrational mode takes the transition state towards the products or the reactants. The potential energy curve for this vibrational mode has a downward slope where the energy decreases as the atoms vibrate. Therefore, the force constant corresponding to this vibration (with negative slope) is negative and its frequency is imaginary.

In the case of the $[CH_2NO_2]^- + CH_3I$ reaction, it can clearly be seen when animated, that the CH_3 group migrates between I and the C or O atoms of the nucleophile in the transition state structures as shown in Figures 4.7. In the reactant ion-dipole complex, there exists one vibrational mode, which has the motion along the reaction coordinate towards transition state (Figure 4.8).
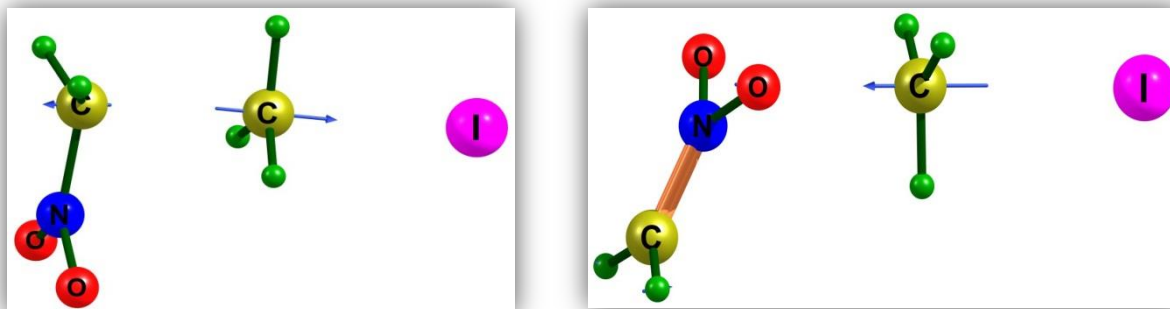
Figure 4.7 Displacement vectors of the vibration at the transition state associated with the imaginary frequency along the reaction coordinate of the $S_N2@C$ (left) and $S_N2@O$ (right) pathways for the $[CH_2NO_2]^- + CH_3I$ reaction computed at MP2/aug-cc-pVDZ.

Figure 4.8. Displacement vectors of the vibration at the reactant complex corresponding to the motion associated to the $S_N2@C$ (left) and $S_N2@O$ (right) pathways of the $[CH_2NO_2]^- + CH_3I$ reaction computed at MP2/aug-cc-pVDZ.

The imaginary frequencies of the vibration responsible for the dissociation of the transition state into the product complex for all the reactions computed at different theoretical levels are listed in Table 4.1.

From the analysis of the Table 4.1 and Table 4.2 (energies of activation) we observed a relation between the magnitude of imaginary frequency of the transition state and the barrier height. It can be seen that the lower imaginary frequencies corresponds to smaller barrier, while the transition state with larger barrier heights comes out with higher imaginary frequency values. This relationship is quite understandable because the magnitude of the any frequency is related to the force constant that is the measure of curvature of the potential energy. So a steep curvature (sharp barrier region) would give a higher force constant that in turn would give a higher imaginary frequency (because the curvature is downward) and a relatively gentle curvature means that the transition state region is relatively flat, which would give a lower force constant and hence a lower imaginary frequency.

Despite of the imaginary frequency and the barrier height values computed with different methods are distinct for the same reaction, the relationships and trends between these two quantities are the same namely, a higher imaginary frequency corresponds to a higher barrier and a lower imaginary frequency to a lower barrier. Notice, however, that the magnitude of

imaginary frequency is affected by the mass of the atoms involved in the vibration through the reduced mass in Equation 4.1. Thus, some care must be exercised when comparing barrier highs and imaginary vibrational frequencies associated with distinct reaction pathways.

Table 4.1 Calculated imaginary frequencies (cm^{-1}) at transition states of the $S_N2@C$ and $S_N2@O$ pathways for all the reactions computed at different theoretical levels.[a]

| TS	MP2/ LAN	MP2/ DZ	B2PLYP/ LAN	B2PLYP / DZ	mPW2PLY P/ LAN	mPW2PLY P/ DZ
$[CH_2NO_2]^-$						
TS@C	-473.5	-445.5	-335.6	-302.7	-358.8	-331.5
TS@O	-515.1	-519.7	-394.8	-381.3	-404.8	-391.6
$[CH_3CHNO_2]^-$						
TS@C	-467.9	-432.9	-343.6	-309.2	-367.4	-339.0
TS@O (*E*)	-504.4	-509.8	-382.1	-371.7	-392.1	-382.8
TS@O (*Z*)	-511.5	-522.0	-392.6	-381.6	-402.6	-391.7
$[(CH_3)_2NO_2]^-$						
TS@C	-443.8	-408.2	-338.1	-301.4	-362.0	-333.9
TS@O	-504.0	-511.9	-382.6	-370.7	-393.1	-381.8
$[c-(CH_2)_2CNO_2]^-$						
TS@C	-335.3	-272.6	-211.0	-93.5	-238.1	-159.0
TS@O	-534.4	-546.3	-409.7	-397.4	-420.3	-413.6

[a] LAN = LanL2DZ, DZ = aug-cc-pVDZ.

4.4 Energetics of the reactions

The potential energy profiles of $[R^1R^2CNO_2]^- + CH_3I$ reactions, with $R^1 = R^2 = H$ (**1**); $R^1 = CH_3$, $R^2 = H$ (**2**); $R^1 = R^2 = CH_3$ (**3**); and $R^1 + R^2 = c-(CH_2)_2$ (**4**), calculated at MP2/CBS level are presented in Figures 4.9–4.12. These energy profiles show the typical behaviour of a double-well/single barrier model of S_N2-type reactions [231–233, 237, 238] involving either the carbon

(C-methylation) or the oxygen (O-methylation) atom of the nucleophile. Both pathways start at the appropriate reactant complex (RC@C or RC@O) formed between the anion and the polar neutral substrate. These reactant complexes formed at the oxygen are slightly more stable for **1** and **2**, while the reverse is observed for **3**, whereas for **4** they are degenerate. These results are relevant because they suggest that a pre-equilibration between the reactant complexes should not strongly affect selectivity. Thus, the selectivity should be driven by the kinetics. From the respective reactant complex, the reaction proceeds through a typical bipyramidal distorted transition state structure [226–233, 237, 238] towards the product.

The nucleophilic displacements can occur at the carbon ($S_N2@C$) or at oxygen ($S_N2@O$). As discussed previously, the potential energy profile for S_N2 reactions in gas phase has a double-well potential. The reaction starts with the initial formation of the reactant ion-dipole complex (minimum – first well), which is stable compared to the reactants at infinite distance: $[R^1R^2CNO_2]^- + CH_3I$. The reactants were considered at zero potential energy and the energy of the other stationary points (ion-dipole complexes, TS, product) was calculated relative to the reactants. The reactant complexes (RC@C and RC@O) cross the barrier associated with the transition states (TS@C and TS@O) to go into another well (second well) corresponding to the product ion-dipole complexes (PC@C and PC@O), which dissociate to give separated products. The reaction barriers are calculated as the difference between the energy of the reactant complex and the transition state.

Figure 4.9 represents the potential energy diagram for the $[CH_2NO_2]^- + CH_3I$ computed with the CBS(T,Q) method. The initially formed reactant complexes, RC@C1 and RC@O1, are stable relative to the separated reactants by -50.1 and -52.3 kJ/mol, respectively. The transition states, TS@C1 and TS@O1, are calculated with activation energy barriers ($\Delta^{\ddagger}E$) of 29.9 and 47.0 kJ/mol, respectively, relative to the respective reactant complex. The PC@C1 is more stable than the PC@O1 by -147.0 kJ/mol and so does the product, P@C1, by -116.1 kJ/mol. The reactions are found to be exothermic with reaction energies ($\Delta_r E$) of -183.8 and -67.7 kJ/mol for the reaction @C and reaction @O, respectively.
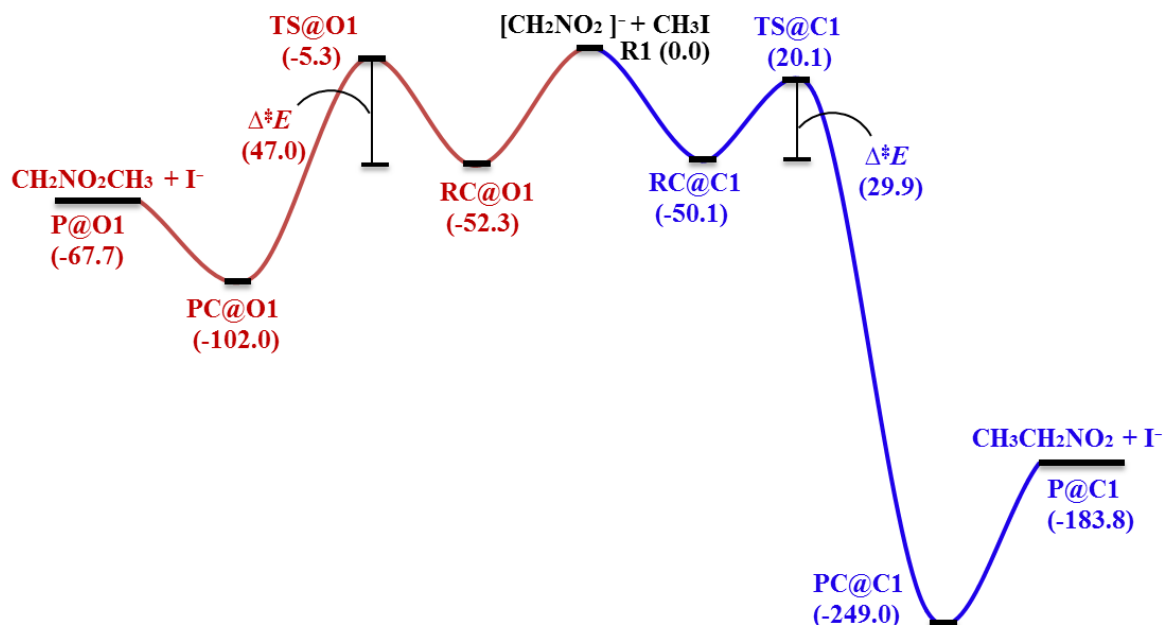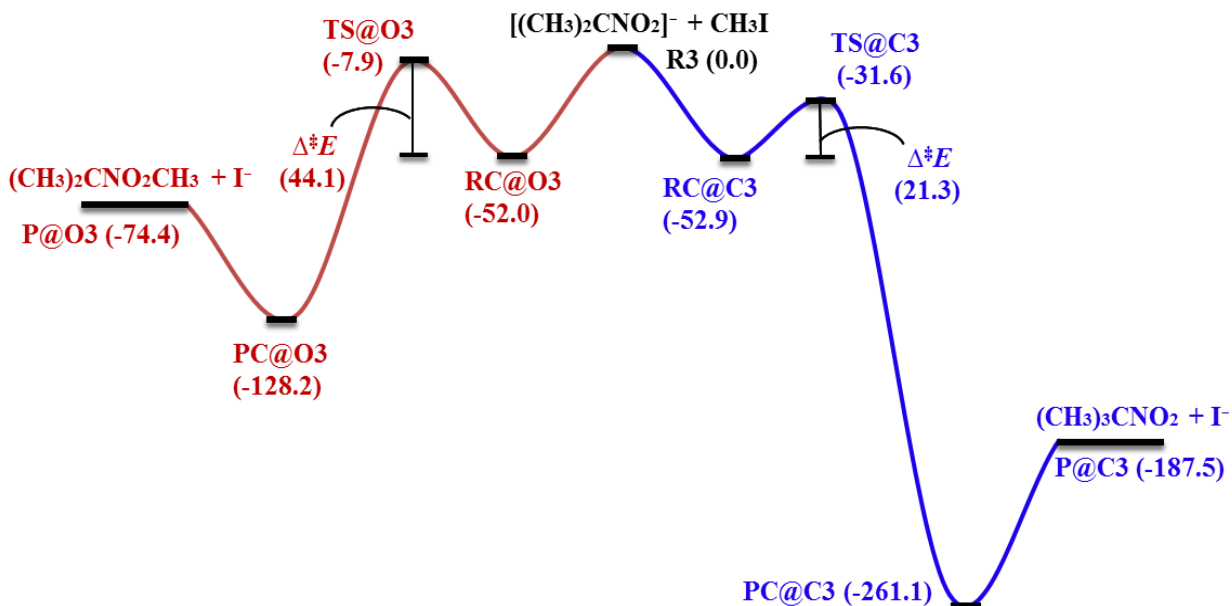
Figure 4.9. Energy profiles of the $[CH_2NO_2]^-$ + CH_3I gas-phase reaction of **1** through the oxygen (O-methylation), and the carbon (C-methylation), atoms of the nucleophile. Calculations at the MP2/CBS level. Energies (in kilojoules per mole) include the zero-point vibrational corrections.

The substituent effects on the reaction rates, mechanism and selectivities were addressed by replacing the hydrogen atoms at the central carbon of the nitroalkane by methyl groups. The replacement of one of the hydrogen in $[CH_2NO_2]^-$ by a methyl group gives the mono-substituted nitroalkane $[CH_3CHNO_2]^-$ (**2**). The two oxygen atoms in $[CH_3CHNO_2]^-$ are no longer equivalent, so the reaction at the oxygen atoms can occur via two different pathways: TS@O (E) and TS@O (Z). The energy profiles for this reaction are shown in Figure 4.10. All the three pathways, that is, $S_N2@C2$, $S_N2@O2$ (E) and $S_N2@O2$ (Z) are exothermic with energy of the reaction ($\Delta_r E$) -188.5, -76.6 and -68.5 kJ/mol, respectively. The product of the reaction at carbon is found to be more stable than the products of reaction through oxygen pathway. The transition states, TS@C2, TS@O2 (E) and TS@O2 (Z), lie below the reactants on the potential energy diagrams with activation energy barriers ($\Delta^\ddagger E$) 25.8, 42.7 and 48.4 kJ/mol, respectively, relative to the respective reactant complex.
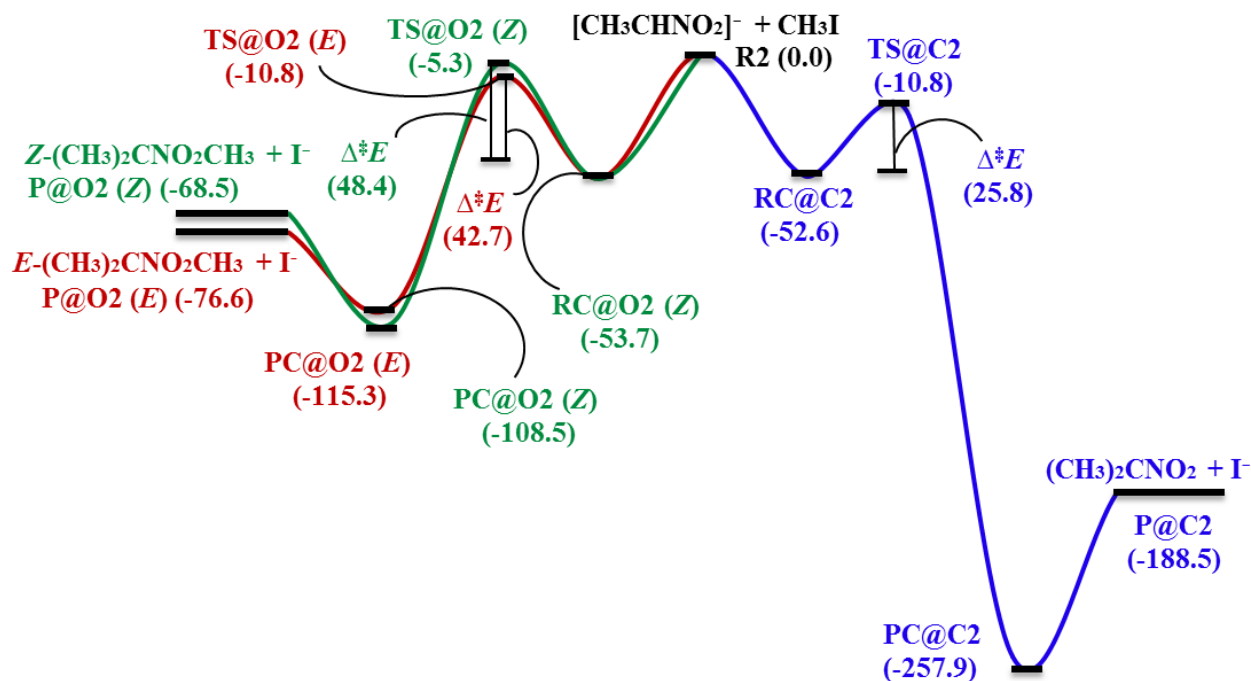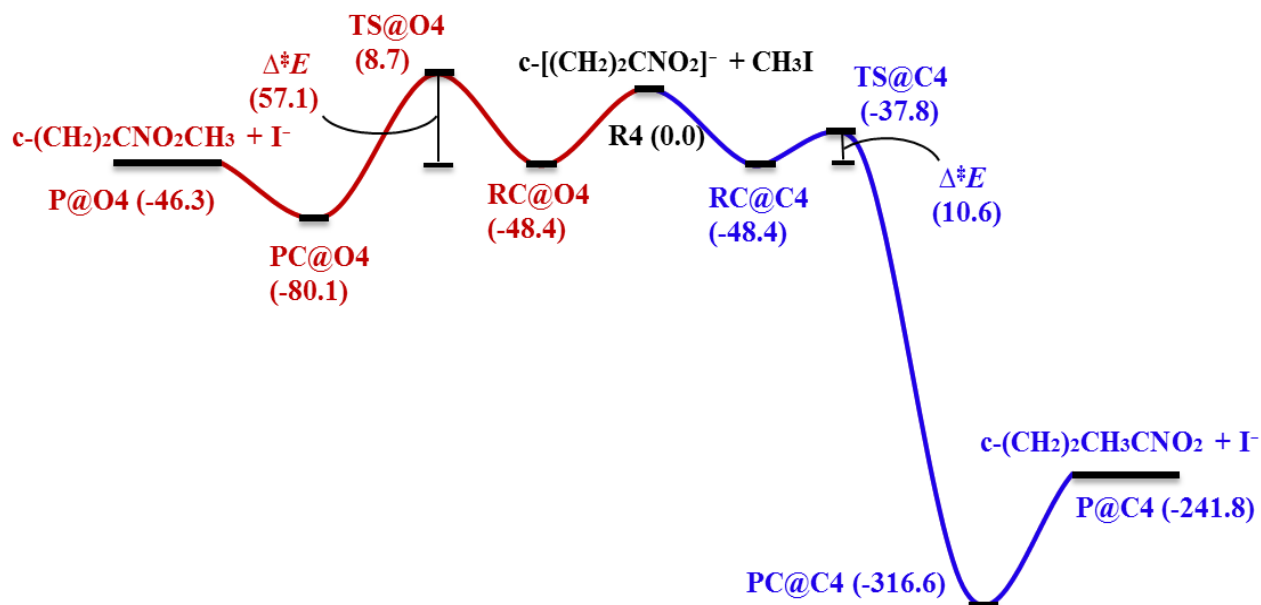
Figure 4.10. Energy profiles of the [CH$_3$CHNO$_2$]$^-$ + CH$_3$I gas-phase reaction of **2** through the oxygen (O-methylation), and the carbon (C-methylation), C-methylation, atoms of the nucleophile. The O-methylation reaction takes place via *syn* and *anti* orientations relative to the substituting alkyl group. Calculations at the MP2/CBS level. Energies (in kilojoules per mole) include the zero-point vibrational corrections.

For the di-substituted nitroalkane, [(CH$_3$)$_2$CNO$_2$]$^-$ (**3**), the oxygen atoms become equivalent as in the unsubstituted substrate and we observed that the reaction barriers decreased as depicted in Figure 4.11. The calculated activation energies of the C-methylation and O-methylation pathways are 21.3 and 44.1 kJ/mol, respectively, and the corresponding reaction energies are -187.5 and -74.4 kJ/mol.

Figure 4.11. Energy profiles of the $[(CH_3)_2CNO_2]^- + CH_3I$ gas-phase reaction of **3** through the oxygen (O-methylation), and the carbon (C-methylation), atoms of the nucleophile. Calculations at the MP2/CBS level. Energies (in kilojoules per mole) include the zero-point vibrational corrections.

The energy profiles show that the C-methylation pathway with the cyclopropane substituent, $[c\text{-}(CH_2)_2CNO_2]^-$ (**4**), has the smallest activation energy (10.6 kJ/mol) while the reaction barrier for $S_N2@O4$ (57.1 kJ/mol) is calculated to be the highest among all reaction pathways involving nitroalkane anions and Iodomethane in the present study. The energy profiles for the $[c\text{-}(CH_2)_2CNO_2]^- + CH_3I$ reaction are illustrated in Figure 4.12. The reaction at the carbon atom is highly exothermic (-241.8 kJ/mol) compared to the reaction at the oxygen atoms (-46.3 kJ/mol). The energy of activation corrected for ZP energy for $S_N2@O4$ pathway is calculated to be much higher than that found for the other pathway, that is, $S_N2@C4$. The PC@C4 is more stable than the PC@O4 by 236.5 kJ/mol.

Figure 4.12. Energy profiles of the $[c-(CH_2)_2CNO_2]^-$ + CH_3I gas-phase reaction of **4** through the oxygen ($S_N2@O$), O-methylation, and the carbon ($S_N2@C$), C-methylation, atoms of the nucleophile. Calculations at the MP2/CBS level. Energies (in kilojoules per mole) include the zero-point vibrational corrections.

The activation energies and reaction energies for the reaction pathways illustrated in Figures 4.9-4.12 are summarized in Table 4.2.

A general feature of these energy profiles is that the C-methylation pathways have energy barriers almost half, except for **4**, where this barrier is nearly one-sixth, of the corresponding pathway through the oxygen, O-methylation. Other general and relevant features of these energy profiles are,

(i)   the activation energies ($\Delta^{\ddagger}E$) of the C-alkylation reactions follow: $\Delta^{\ddagger}E(\mathbf{1}) > \Delta^{\ddagger}E(\mathbf{2}) > \Delta^{\ddagger}E(\mathbf{3}) >> \Delta^{\ddagger}E(\mathbf{4})$, whereas those O-alkylation: $\Delta^{\ddagger}E(\mathbf{4}) >> \Delta^{\ddagger}E(\mathbf{2}\text{-}Z) \geq \Delta^{\ddagger}E(\mathbf{1}) > \Delta^{\ddagger}E(\mathbf{3}) \geq \Delta^{\ddagger}E(\mathbf{2}\text{-}E)$. The trend observed for the C-methylation reactions follows the same trend of the experimental rate constants.

(ii)   the reactant complexes (RC) are formed with an internal energy excess of *ca.* 50 kJ mol^{-1}. This suggests that the RCs have enough internal energy to overcome the energy barriers, especially via the $S_N2@C$ pathway.

(iii)   the product complexes formed through the C-methylation (PC@C) are *ca.* 140 kJ mol^{-1} more stable than the corresponding PC@O, except for **4**, where this stability is nearly 240 kJ mol^{-1}. The reactions are highly exothermic, especially for the formation of PC@C.

These results combined indicate that these gas-phase reactions should be quite efficient and irreversible. The overall trend found is that the activation energies ($\Delta^{\ddagger}E$) decreases with the increase of crowdedness around the central carbon. This trend is quite interesting because it was expected that the reaction barrier should increase as the environment around the central carbon becomes more crowded due to the steric hinderance effects. A similar trend has also been found experimentally for these same reactions by Kato et al [71]. In fact, the C-methylations are favored over O-methylations as they proceed with smaller activation energies. The reactions through the carbon atom are much more exothermic than the corresponding reactions through the oxygen atoms.

Clearly, considering the difference between the activation energies and the exothermicities, the reaction pathways through the carbon atom are strongly preferred. These results do contradict the proposed explanation for the differences in reaction efficiencies [71], namely, as the nucleophile becomes more sterically hindered the reaction efficiencies increase and thus, the nucleophilic attack should be through the oxygen atom where the steric effect is insignificant. Whereas for ring substituted phenyl nitronates $[R^1R^2CNO_2]^-$, where R^1 = X-Ph and R^2 = H, B3LYP/6-31+G* calculations provided slightly lower barriers for the O-methylation than the respective C-methylation [63]. The origin of these differences between alkyl and aryl nitronates regioselectivities is under investigation and partial results are presented in Chapter 5. Notice that the transition states for O-alkylation (TS@O) of symmetric nitronates are doubly degenerate and thus, care must be exercised when inferring the selectivity from the energy differences between TS@C and TS@O. Except for the O-methylation **2** that can occur via two different pathways

TS@O (*E*) and TS@O (*Z*) to form isomers *E* and *Z*, respectively (see Scheme 1), and are thus treated separately.

It is noteworthy that the calculated difference of the activation energies between both pathways (TS@C *vs.* TS@O) is probably due to the transition states found in C-methylation reactions are early transition states because they resemble more the reactants and according to the Hammond postulate the early transition states are generally characteristic of fast exothermic reactions [239] [208]. On the other hand, the transition states found in the reaction pathways of O-methylations are late transition states as they resemble more the products, thus are characteristic of slow endothermic reactions.

These differences in activation energies can also be directly related to the difference of the exorthermicity of the respective product, in accordance with the Bell-Evans-Polanyi principle [240–242]. In other words, we could use the difference of the exorthermicity to predict the selectivity. Employing average bond strengths to estimate reaction enthalpy is not a straightforward task for these reactions because of the Lewis structures associated with the R–NO$_2$ and C=N(O)O–R groups. For instance, the exorthermicity difference between O- and C-methylation $R^1R^2C=N(=O)–O–Me \rightarrow R^1R^2C(Me)–N(=O)_2$ is approximated as $\Delta_r H \approx [L(C=N) - L(N=O)] + [L(N–O) - L(C–N)] + [L(C–O) - L(C–C)] = (615 - 594) + (201 - 305) + (360 - 347) = 21 - 104 + 13 = 70 \text{ kJ mol}^{-1}$, where $L(A–B)$ are average bond enthalpies [243]. Thus, the larger exorthermicity of the C-methylated products are in agreement with the quantum chemical calculations, despite the underestimation of more than twice by the average bond enthalpy approach applied to those Lewis structures. Noteworthy that the origin of larger exorthermicity of the C-methylated products is the much stronger C–N bond compared to the N–O bond.

Regarding the structures of the main stationary points on the energy profiles, we observed that transition states show the following order of the C–I distance: (**1**) > (**2**) > (**3**) > (**4**) for the C-methylation (TS@C) and (**4**) > (**2**-*Z*) ≥ (**1**) > (**3**) ≥ (**2**-*E*) for the O-methylation (TS@O). These

sequences match exactly those observed for their respective activation energies. This is because the C–I distance is associated with the geometry distortion from the reactant structure (positive contribution to the activation energy) and with the partially broken C–I bond (stabilizing contribution to $\Delta^\ddagger E$). Namely, the shortest C–I distance would have the smallest distortion and the largest C–I stabilizing interaction, thus the smallest activation energy. In fact, the trends observed for the C–I distances indicate that the most exothermic reactions (C-methylation) occur through earlier transition states that correlate to lower activation energies for larger reaction exorthermicities via the Bell-Evans-Polanyi principle [240–242].

In a more technical note, we observed that the activation energies of the reaction pathway through the carbon atom decrease more strongly than that through the oxygen atom with increase of the basis set. This is mainly due to that for the $S_N2@C$ reactions to occur the nucleophile has to change its hybridization from sp^2 to sp^3 that involves a larger structural (from planar to pyramidal type geometries) and electronic rearrangement of the nucleophile and should be more susceptible to the quality of the basis set employed. The basis aug-cc-pVDZ-pp calculates more efficiently these structural changes than the LAN basis. However, for $S_N2@O$ reactions, there are no such changes in the geomtry during the nucleophilic attack and hence both basis sets gives almost the same $\Delta^\ddagger E$ values. Concerning the reliability and convergence of the calculated properties, the potential energy profiles of methylation reactions of **1** and **2** were determined with the MP2/aug-cc-pVTZ method, which corroborated quantitatively the results presented in Figures 4.9 and 4.10, as presented in Tables 4.2 and 4.3.

It can be seen from the Table 4.2 that the reaction with cyclopropylnitronate, $[c\text{-}(CH_2)_2CNO_2]^-$ (**4**), presents the lowest reaction barrier ($\Delta^\ddagger E$) corrected for zero-point (ZP) energy and therefore it is likely to proceed with the fastest rate. The S_N2 reactions are supposed to be less favorable for larger anions if the reaction occurs at carbon atom of anion. One can assume that the nucleophilic attack is actually made by the oxygen atom of the nitro group rather than carbon but a comparison of reaction barriers computed for reactions at carbon and reactions at oxygen (Table 4.2) shows that the reaction through carbon is always preferred, which cannot rationalize the experimental data.

Despite the agreement between observed and calculated trends, a consistent explanation for this reaction mechanism and experimental results is still lacking. This explanation should be based on comparisons between the calculated rate constants and kinetics simulations as well as the origin of the reactivity differences. We thus present next the results for the RRKM calculations of the rate constants, the numerical solutions of the complete kinetics scheme of these reactions, and the possible reasons for the observed and calculated dependence of the nucleophile reactivity upon substituent replacements.

Table 4.2 Relative barrier heights ($\Delta^{\ddagger}E$) and energy of reaction ($\Delta_r E$) for the $S_N 2$ reactions between $[R_1 R_2 CNO_2]^-$ and CH_3I computed at different theoretical levels. The zero-point energy (ZPE) corrections have been included. DZ = aug-cc-pVDZ, TZ = aug-cc-pVTZ, QZ = aug-cc-pVQZ.

| Species	$\Delta^{\ddagger}E$ (kJ/mol)						$\Delta_r E$ (kJ/mol)					
	MP2/DZ	MP2/TZ	SP-MP2/TZ	SP-MP2/QZ	CBS (D,T)	CBS (T,Q)	MP2/DZ	MP2/TZ	SP-MP2/TZ	SP-MP2/QZ	CBS (D,T)	CBS (T,Q)
$[CH_2NO_2]^-$												
$S_N 2@C1$	20.7	27.8	26.8	28.6	28.7	29.9	-208.1	-188.0	-188.5	-185.7	-176.8	-183.8
$S_N 2@O1$	36.9	44.9	44.4	46.0	47.0	47.0	-83.2	-70.6	-71.2	-69.0	-62.1	-67.8
$[CH_3CHNO_2]^-$												
$S_N 2@C2$	16.1	23.7	22.8	24.6	25.2	25.8	-214.9	-193.3	-193.8	-190.7	-186.1	-188.5
$S_N 2@O2$ (E)	34.5	41.33	41.2	42.1	43.5	42.7	-91.9	-79.8	-80.2	-78.0	-75.8	-76.6
$S_N 2@O2$ (Z)	39.9	46.57	47.0	47.9	49.5	48.4	-83.9	-71.6	-72.2	-69.9	-67.8	-68.5
$[(CH_3)_2CNO_2]^-$												
$S_N 2@C3$	11.6		18.0	20.0	20.2	21.3	-219.2		-195.4	-191.8	-186.7	-187.4
$S_N 2@O3$	33.1		41.7	43.4	44.8	44.1	-90.9		-79.6	-77.4	-75.4	-74.4
$[c\text{-}(CH_2)_2CNO_2]^-$												
$S_N 2@C4$	4.3		8.5	9.8	10.0	10.6	-266.3		-246.9	-244.8	-239.9	-241.8
$S_N 2@O4$	49.8		56.8	57.2	59.2	57.1	-61.6		-51.1	-49.1	-47.2	-46.3

Table 4.3 represents RMS deviations (kJ/mol) from the complete basis limit, CBS(T,Q), for the energies of activation and enthalpies of reaction. For reaction barrier, the accumulative RMS deviations are calculated to be 80.0, 19.7, 7.5 and 8.2 kJ/mol for MP2/DZ, MP2/TZ, MP2/QZ and CBS(D,T) methods, respectively. The average RMS deviation are found to be 8.89, 2.19, 0.83 and 0.91 kJ/mol for MP2/DZ, MP2/TZ, MP2/QZ and CBS(D,T) methods, respectively. For reaction energy, the accumulative RMS deviations are calculated as 44.5, 43.8, 21.3 and 21.1 kJ/mol, while the average RMS deviations are 4.94, 4.86, 2.36 and 2.34 kJ/mol for MP2/DZ, MP2/TZ, MP2/QZ and CBS(D,T) methods, respectively. These comparisons show that the method CBS(D,T) presents the lowest RMS deviation.

Table 4.3 RMS deviations (kJ/mol) from the complete basis limit, CBS(T,Q), for the energy of activation and energy of reaction corrected for ZP energy. DZ = aug-cc-pVDZ, TZ = aug-cc-pVTZ, QZ = aug-cc-pVQZ.

Species	$\Delta^{\ddagger}E$ (kJ/mol)					$\Delta_{r}E$ (kJ/mol)				
	MP2/DZ	MP2/TZ	SP-MP2/TZ	SP-MP2/QZ	CBS(D,T)	MP2/DZ	MP2/TZ	SP-MP2/TZ	SP-MP2/QZ	CBS (D,T)
[CH$_2$NO$_2$]$^{-}$										
S$_N$2@C1	9.2	2.1	3.1	1.3	1.2	10.1	4.2	4.7	1.9	7.0
S$_N$2@O1	10.1	2.1	2.6	1.0	0	2.2	2.8	3.4	1.2	5.7
[CH$_3$CHNO$_2$]$^{-}$										
S$_N$2@C2	9.7	2.1	3.0	1.2	0.6	12.3	4.8	5.3	2.2	2.4
S$_N$2@O2 (*anti*)	8.2	1.4	1.5	0.6	0.8	0.8	3.2	3.6	1.4	0.8
S$_N$2@O2 (*syn*)	8.5	1.8	1.4	0.5	1.1	0.1	3.1	3.7	1.4	0.7
[(CH$_3$)$_2$CNO$_2$]$^{-}$										
S$_N$2@C3	9.7		3.3	1.3	1.1	11.4		8.0	4.4	0.7
S$_N$2@O3	11.0		2.4	0.7	0.7	1.8		5.2	3.0	1.0
[c-(CH$_2$)$_2$CNO$_2$]$^{-}$										
S$_N$2@C4	6.3		2.1	0.8	0.6	5.7		5.1	3.0	1.9
S$_N$2@O4	7.3		0.3	0.1	2.1	0.1		4.8	2.8	0.9

4.5 Reaction rates and kinetics simulations

To calculate the relative concentrations and, thus, the reaction selectivity we solved the kinetics rate equations, which depend upon the rate constant of each elementary step. Figure 4.13 represents all of the different pathways of the reaction between iodomethane and nitronates.
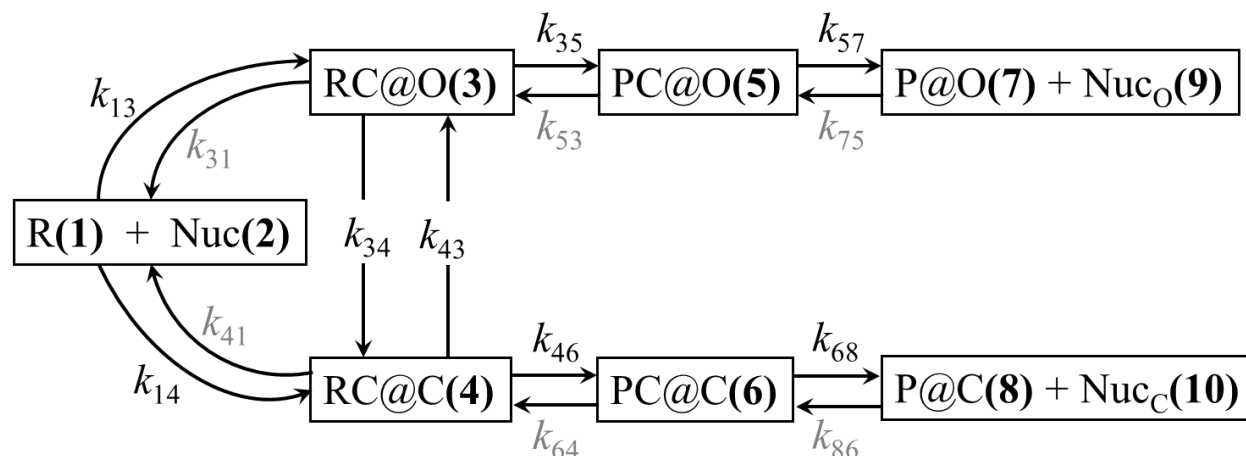
Figure 4.13. Kinetics scheme for the S_N2 reaction pathways involving nitronate nucleophiles (Nuc) and iodomethane substrate (R).

The general kinetic equation associated with the reaction pathways scheme in Figure 4.13 can be expressed as follows:

$$\frac{d[C]_i}{dt} = \sum_j k_{j \to i}[C]_j - \sum_m k_{i \to m}[C]_i$$

where $[C]_i$ and $[C]_j$ are the concentrations of various intermediates and products, respectively, and $k_{j \to i}$ is the microcanonical rate constant for step j to i.

Simulations of the kinetics of these reactions require the knowledge of the rate constants associated with the reactant complexes, their reactions to form the product complexes that dissociate into the products. Because the reactions are highly exothermic, the backward rate constants (k_{31}, k_{41}, k_{53}, k_{64}, k_{75}, and k_{86}) are very small.

As discussed earlier, the separated reactants form a reactant and product ion-dipole complex. The formation of the complexes is barrierless, hence the transition state theory for bimolecular reactions cannot be used. To calculate the capture rate constant for the formation of the reactant ion-dipole complexes (k_{13} and k_{14}) and product ion-dipole complexes (k_{75} and k_{86}), we have employed the parameterized average dipole orientation (ADO) theory [36, 37] that uses the dipole moment and polarizability of the neutral substrate (CH_3I) for reactant complexes and of the neutral products (P@C and P@O) for product complexes, and the reduced mass and charge of the anions calculated at MP2/aug-cc-pVDZ (Tables 4.4 and 4.5). This choice of theory was predicated upon the consistency with the experimental measurements and calculations of the reaction efficiencies. The details of the theory were presented in the Methodology section. The calculated rate constant values are presented in Table 4.4 and Table 4.5.

Table 4.4 The calculated rate constants of association or capture, k_R ($\times 10^9$ cm^3 molecule^{-1} s^{-1}), for the reactions of $[R^1R^2CNO_2]^-$ with CH_3I to form reactant complexes using equation 3.43. Values used for CH_3I: dipole moment 2.027 D (calculated) and polarizability 7.14 Å^3 (calculated). The locked dipole or induced dipole approximation are obtained by setting $c = 0$ or 1 in equation 3.43, respectively.

Nucleophile	k_R (ADO)	k_R (induced dipole)	k_R (locked dipole)
	(k_{13} and k_{14})		
$[H_2CNO_2]^-$ (**1**)	3.13	0.96	3.82
$[CH_3CHNO_2]^-$ (**2**)	2.92	0.90	3.56
$[(CH_3)_2CNO_2]^-$ (**3**)	2.76	0.85	3.37
$[c-(CH_2)_2CNO_2]^-$ (**4**)	2.78	0.85	3.39

Table 4.5 The calculated rate constants of association or capture, k_P ($\times 10^9$ cm^3 molecule^{-1} s^{-1}) for the formation of product complexes from separated products.

Nucleophile		k_P (ADO)	k_P (induced dipole)	k_P (locked dipole)
$[H_2CNO_2]^-$ (**1**)	k_{86}	2.99	0.87	3.57
	k_{75}	2.22	0.92	3.08
$[CH_3CHNO_2]^-$ (**2**)	k_{86}	9.70	0.93	6.60
	k_{75} (E)	3.46	0.97	4.06
	k_{75} (Z)	4.11	0.98	4.44
$[(CH_3)_2CNO_2]^-$ (**3**)	k_{86}	8.57	0.98	6.39
	k_{75}	3.74	1.03	4.33
$[c\text{-}(CH_2)_2CNO_2]^-$ (**4**)	k_{86}	9.13	0.97	6.54
	k_{75}	2.92	1.03	3.79

The dissociation rate constants of the reactant complexes (k_{31} and k_{41}) were estimated from the equilibrium constant obtained from the calculated standard Gibbs free energy using TST, and similarly for the dissociation rates of the product complexes (k_{57} and k_{68}).

Now, there is a possibility of the conversion of RC@C into RC@O prior to the S_N2 steps. The canonical rates constants for these conversions, k_{34} and k_{43}, were calculated using RRKM theory.

The remaining rate constants were obtained by integration of the microcanonical RRKM rates [132, 133, 138] weighted by the Boltzmann factor at 298 K [138]. In the RRKM theory, the structures and vibrational frequencies calculated at the MP2/aug-cc-pVDZ level were employed, whereas the energy barriers were provided by the MP2/CBS method. The available energy (E) to be distributed within the rovibrational states is given by $E_0 + E_{thermal}$, where E_0 is calculated as the difference between energy of the transition state and of the separated reactants, while $E_{thermal}$ is the (classical) thermal energy [132, 133, 138]. The calculated canonical rate constants as a function of the available energy to the reactant complexes for each reaction pathway are presented in Figures 4.14 and 4.15. It can be observed that the canonical rate constants for the C-methylation reactions have the following order: **4** > **3** > **1** > **2**, while the O-methylation: **2**-E > **1**

> **2**-Z > **4** > **3**, which is not exactly the same sequence as that of the activation energies. Therefore, one can say that the activation energy is not the only determining factor of the reaction rate. However, the calculated trend for the C-methylation reactions does coincide with the observed reaction rates, namely, k_{obs} (10^{-10} cm^3 s^{-1}) = 1.05, 1.50, 1.77, and 5.02 for nitronates **1**, **2**, **3**, and **4** [71]. It also can be observed in Figure 6 that the canonical rate constant of C-methylation reaction **2** is initially larger than that of reaction **1**. However, as the available energy increases the rate of **1** becomes higher than **2**, because the reactant complex of **1** has fewer vibrational modes than of **2**. Therefore, the available energy is more focused towards the reaction coordinate for the alkylation of nitronate **1**.

Clearly, despite the O-methylation reactions being doubly degenerate, the regioselectivity towards the formation of the C–C bond is highly preferred according to the canonical rates by several orders of magnitude.

In the calculation performed at MP2/LAN level, the available energy induces a change of the S_N2 pathway for nitromethane nitronate (**1**), namely, for available energies near the minimum, the C-methylation pathway has a larger rate constant than the O-methylation pathway, however, as the available thermal energy increases, the rate constant O-methylation become larger than that of the C-methylation pathway. For nitroethane nitronate (**2**), a similar trend is observed. However, the calculations with CBS(T,Q) method does not show any change in selectivity with the increase of available energy because the difference in the energy barriers of the two pathways becomes larger and hence the rate for the O-methylation reactions calculated at the CBS(T,Q) level are much smaller than those calculated at the MP2/LAN one. The increase of available energy increases the rate of O-methylation, however it does not reverse the selectivity of the two pathways.
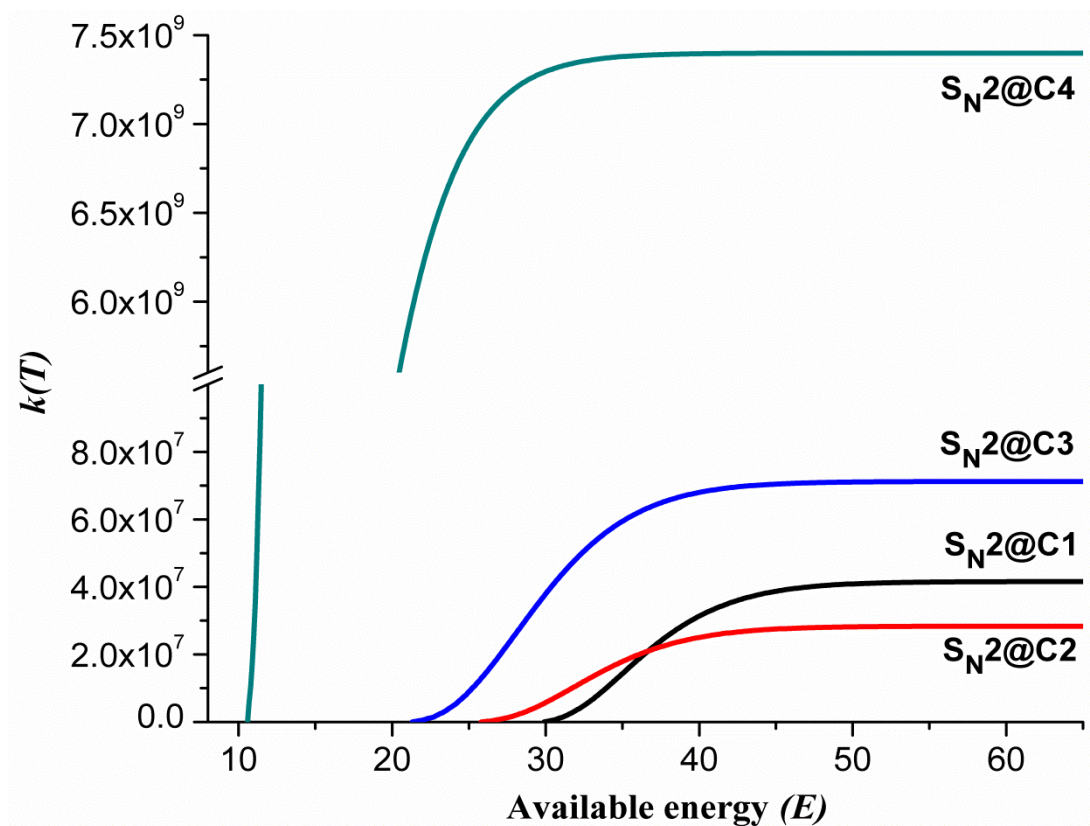
Figure 4.14 Canonical rate constants (in cm^3 s^{-1}) for the C-methylation (@C) of the nitronates $[H_2CNO_2]^-$ (**1**), $[CH_3CHNO_2]^-$ (**2**), $[(CH_3)_2CNO_2]^-$ (**3**), and $[c-(CH_2)_2CNO_2]^-$ (**4**) with CH_3I, calculated with the RRKM theory as a function of the available energy (kJ mol^{-1}) to the reactant complexes, starting at the E_0. The energetics used are those calculated at the MP2/CBS (T,Q) level.
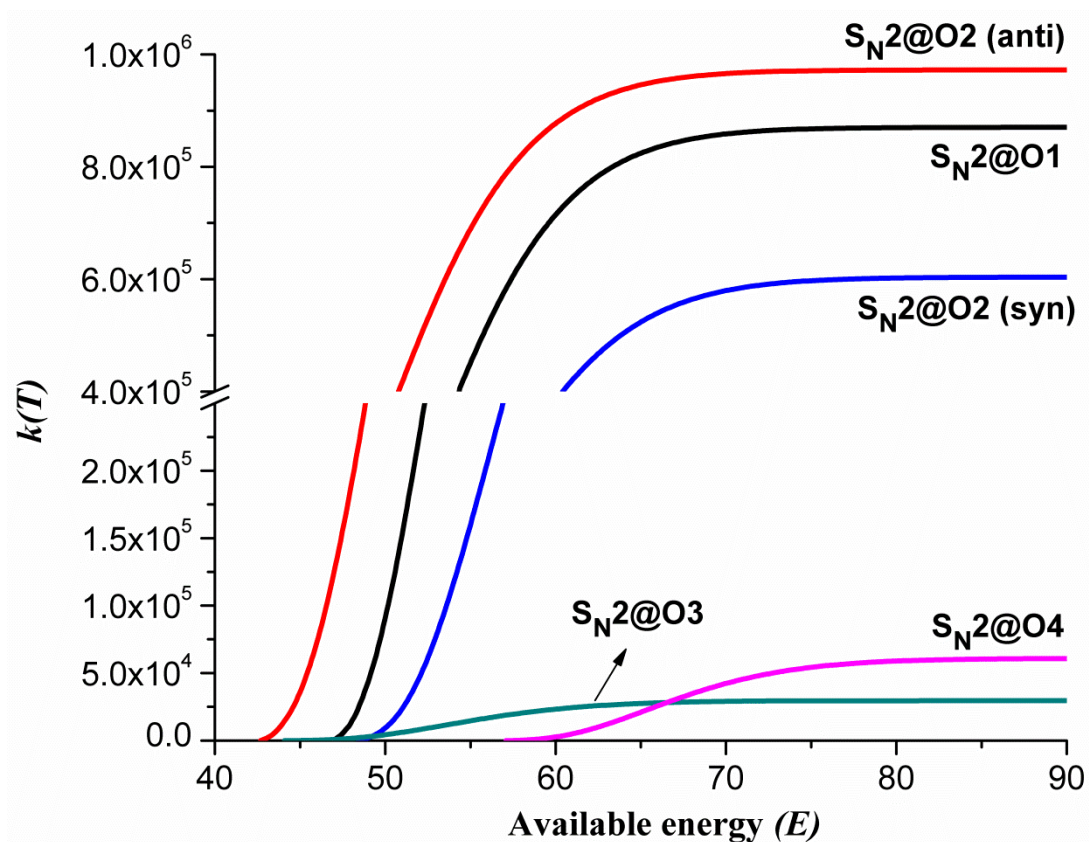
Figure 4.15. Canonical rate constants (in $cm^3 \; s^{-1}$) for the O-methylation (@O) of the nitronates $[H_2CNO_2]^-$ (**1**), $[CH_3CHNO_2]^-$ (**2**), $[(CH_3)_2CNO_2]^-$ (**3**), and $[c\text{-}(CH_2)_2CNO_2]^-$ (**4**) with CH_3I, calculated with the RRKM theory as a function of the available energy (kJ mol^{-1}) to the reactant complexes, starting at the E_0.

For most S_N2 reactions, the rates increase steeply with the available energy to the reactant complexes. From Figures 4.14 and 4.15 and Table 4.7, it can be observed that the canonical rate constants $k(T)$ for the $S_N2@C$ conversion of reactant complexes into product complexes have the following order: $S_N2@C4 > S_N2@C3 > S_N2@C1 > S_N2@C2$. In the case of $S_N2@O$ reactions (Figure 4.15) the following order was found $S_N2@O2$ (E) $> S_N2@O1 > S_N2@O2$ (Z) $> S_N2@O4 > S_N2@O3$, which is not exactly the same sequence as that of the activation energies. Therefore, one can say that the activation energy is not the only determining factor of the reaction rate. However, the calculated order for the $S_N2@C$ reaction rates does coincide with the observed reaction rates, namely, k_{obs} (10^{-10} $cm^3 \; s^{-1}$) = 1.05, 1.50, 1.77, and 5.02 for deprotonated nitroalkanes **1**, **2**, **3**, and **4** [71].

4.5.1 Stepwise increase of the RRKM rate $k(E)$

It was observed that the microcanonical rate constant of the reactions calculated by RRKM theory increases in a stepwise manner, as shown in Figure 4.16.
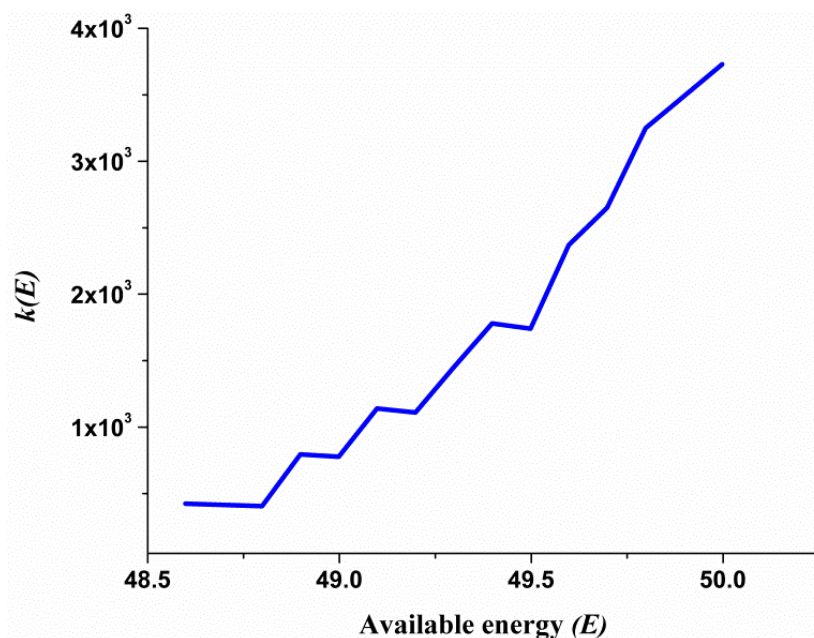
Figure 4.16. The stepwise increase in the RRKM rate constant k (cm^3 molecule^{-1} s^{-1}) of $S_N2@O4$ reaction as a function of the available energy (kJ/mol) to the reactant complex.

The stepwise increase in the rate constant $k(E)$ is a result of the RRKM theory expressed by equation 4.2, that is,

$$k(E) = \frac{G^{\ddagger}(E - E_0)}{hN(E)} \qquad\qquad 4.2$$

where $G^{\ddagger}(E - E_0)$ is the sum of vibrational states in the transition state at energy $E - E_0$, E_0 is the threshold energy, and $N(E)$ is the density of vibrational states. Usually, $N(E)$ is a smooth function of vibrational energy at energies around the threshold energy. However, $G^{\ddagger}(E - E_0)$ is a step function of the vibrational energy, that is, it is zero at energy smaller than the threshold. It

is equal to one at threshold, two at first excited vibrational level, three at second excited vibrational level and so on. Thus, the stepwise behavior of $k(E)$ as the energy increases is due to the quantized nature and the small degeneracy of the vibrational states for small molecules. It can be observed from the plot in Figure 4.16 that the stepwise manner is more pronounced just above the threshold and becomes less pronounced with the increasing energy. The reason of this trend is that, in a region just above the threshold the spacing between vibrational levels is large, whereas state separations become increasingly smaller with the increase of energy. Also, the step size, $1/hN(E)$, decreases due to the increase of density of vibrational states, $N(E)$.

The stepwise increase in the RRKM rate constant with the energy provides evidence that the vibrational states of the transition state are quantized, which is one of the assumptions of the RRKM theory. The stepwise increase of the rate constant has also been observed experimentally for some unimolecular reactions [244−246] that leads to the confirmation of quantization of the energy level of the transition state [247, 248]. The rate of the reactions calculated in this work by RRKM theory increases in a stepwise manner thus providing evidence of the quantization of the vibrational states of the transition state.

4.5.2 Kinetics Equations and Temporal Dependence of Concentrations

The kinetics equations associated with the reaction pathways scheme in Figure 4.13 are,

$$\frac{d[R]}{dt} = \frac{d[Nuc]}{dt} = -k_{13}[R][Nuc] - k_{14}[R][Nuc] + k_{31}[RC@O] + k_{41}[RC@C]$$

$$\frac{d[RC@O]}{dt} = -k_{34}[RC@O] - k_{35}[RC@O] - k_{31}[RC@O] + k_{13}[R][Nuc] + k_{43}[RC@C] + k_{53}[PC@O]$$

$$\frac{d[RC@C]}{dt} = -k_{43}[RC@C] - k_{46}[RC@C] - k_{41}[RC@C] + k_{14}[R][Nuc] + k_{34}[RC@O] + k_{64}[PC@C]$$

$$\frac{d[PC@O]}{dt} = -k_{53}[PC@O] - k_{57}[PC@O] + k_{35}[RC@O] + k_{75}[P@O][Nuc_O]$$

$$\frac{d[PC@C]}{dt} = -k_{64}[PC@C] - k_{68}[PC@C] + k_{46}[RC@C] + k_{86}[P@C][Nuc_C]$$

$$\frac{d[P@O]}{dt} = \frac{d[Nuc_O]}{dt} = -k_{75}[P@O][Nuc_O] + k_{57}[PC@O]$$

$$\frac{d[P@C]}{dt} = \frac{d[Nuc_C]}{dt} = -k_{86}[P@C][Nuc_C] + k_{68}[PC@C]$$

These equations were solved numerically using the fourth-order Runge-Kutta method with an adaptive integration step [225]. To mimic the experimental conditions [71], the initial concentration of the nucleophile, Nuc, was set 10^4 times smaller than the concentration of the neutral substrate, R, in Figure 4.13. The initial concentrations of the remaining species (intermediates and products) were set to zero.

The concentration of nucleophile decreases from maximum to *ca.* 0 and hence the concentration of the reactant complexes increases from zero to its maximum value within $10^{-6} - 10^{-7}$ s. The temporal dependence of these concentrations is presented in Figure A3 in the Appendices. These populations decreased slowly but steadily as the S_N2 reactions occurred. The rate constants involved in the kinetics scheme (Figure 4.13) calculated at total available energy $(E + E_T)$, are presented in Table 4.6. Table 4.7 represents the calculated canonical rate constants $k(T)$ (cm^3 molecule^{-1} s^{-1}) for the conversion of reactant complex into the product complex passing through the transition state using RRKM theory at different theoretical levels.

Table 4.6 The calculated rate constants (s^{-1} and cm^3 molecule^{-1} s^{-1}) at total available energy ($E + E_T$), involved in kinetics scheme of $[R^1R^2CNO_2]^-$ + CH$_3$I reactions. All calculations at the MP2/aug-cc-pVDZ level at 298 K.

Rate constants	Method	$[CH_2NO_2]^-$	$[CH_3CHNO_2]^-$ (Z)	$[CH_3CHNO_2]^-$ (E)	$[(CH_3)_2CNO_2]^-$	$[c\text{-}(CH_2)_2CNO_2]^-$
k_{13}	ADO	3.13×10^9	2.92×10^9	2.92×10^9	2.76×10^9	2.78×10^9
k_{31}	TST	6.40×10^5	7.26×10^5	8.76×10^5	4.13×10^5	2.06×10^6
k_{14}	ADO	3.13×10^9	2.92×10^9	2.92×10^9	2.76×10^9	2.78×10^9
k_{41}	TST	4.13×10^6	1.61×10^6	1.61×10^6	9.20×10^5	1.39×10^6
k_{34}	RRKM	1.02×10^{12}	2.62×10^{12}	2.62×10^{12}	1.04×10^{12}	1.08×10^{12}
k_{43}	RRKM	2.84×10^{12}	4.31×10^{12}	2.53×10^{12}	1.32×10^{13}	3.44×10^{12}
k_{35}	RRKM	5.58×10^6	5.08×10^5	3.45×10^6	4.36×10^5	2.52×10^5
k_{53}		0.0	0.0	0.0	0.0	0.0
k_{46}	RRKM	3.70×10^8	4.75×10^8	4.75×10^8	2.34×10^9	1.43×10^{11}
k_{64}		0.0	0.0	0.0	0.0	0.0
k_{57}	TST	3.48×10^{11}	1.42×10^{11}	1.68×10^{13}	8.73×10^{13}	2.63×10^{11}
k_{75}	ADO	2.22×10^9	3.46×10^9	4.11×10^9	3.74×10^9	2.92×10^9
k_{68}	TST	9.14×10^{15}	1.67×10^{17}	1.67×10^{17}	3.52×10^{17}	7.97×10^{17}
k_{86}	ADO	2.99×10^9	9.70×10^9	9.70×10^9	8.57×10^9	9.13×10^9

Table 4.7 Calculated canonical rate constants $k(T)$ (cm^3 molecule^{-1} s^{-1}) for the conversion of reactant complex into the product complex passing through the transition state using RRKM theory at available energy E. DZ = aug-cc-pVDZ, TZ = aug-cc-pVTZ, QZ = aug-cc-pVQZ.

Nucleophile	MP2/DZ	MP2/TZ	MP2/QZ	CBS(D,T)	CBS(T,Q)
[CH$_2$NO$_2$]$^-$					
S$_N$2@C1	3.69×10^8	8.26×10^7	5.46×10^7	5.41×10^7	4.16×10^7
S$_N$2@O1	5.59×10^6	1.37×10^6	1.03×10^6	8.61×10^5	8.71×10^5
[CH$_3$CHNO$_2$]$^-$					
S$_N$2@C2	4.75×10^8	6.37×10^7	3.91×10^7	3.35×10^7	2.84×10^7
S$_N$2@O2 (*anti*)	5.08×10^5	1.34×10^6	1.09×10^6	8.25×10^5	9.53×10^5
S$_N$2@O2 (*syn*)	3.45×10^6	7.92×10^5	6.64×10^5	4.9×10^5	6.04×10^5
[(CH$_3$)$_2$CNO$_2$]$^-$					
S$_N$2@C3	2.34×10^9	2.15×10^8	1.07×10^8	1.01×10^8	7.12×10^7
S$_N$2@O3	4.36×10^5	5.11×10^4	3.51×10^4	2.52×10^4	2.96×10^4
[c-(CH$_2$)$_2$CNO$_2$]$^-$					
S$_N$2@C4	1.43×10^{11}	1.73×10^{10}	9.92×10^9	9.48×10^9	7.40×10^9
S$_N$2@O4	2.52×10^5	6.93×10^4	5.91×10^4	4.09×10^4	6.09×10^4

The populations of the product complexes and the separated products increase with a similar rate and are depicted in Figure 4.17 for different available energies. The energetics used were calculated at the CBS(T,Q) level.
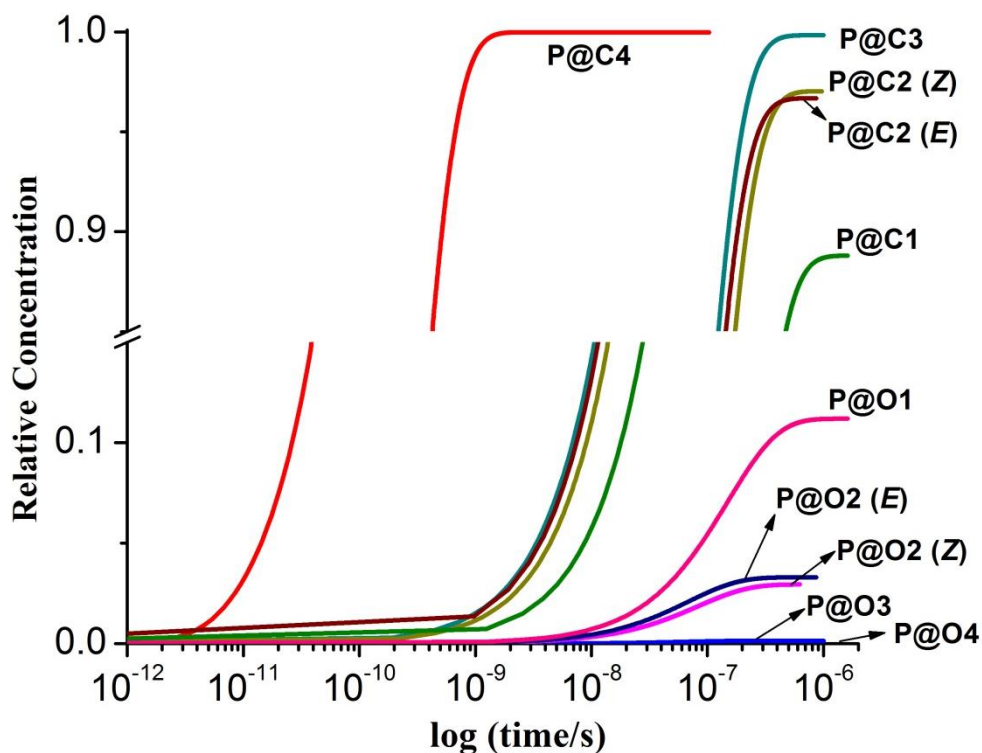
Figure 4.17. Temporal dependence of the relative concentration of the O- (@O) and C-methylation (@C) products of nitronates $[H_2CNO_2]^-$ (**1**), $[CH_3CHNO_2]^-$ (**2**), $[(CH_3)_2CNO_2]^-$ (**3**), and $[c\text{-}(CH_2)_2CNO_2]^-$ (**4**) by CH_3I, at available energy $E_0 + E_{thermal}$. This simulation uses equilibrium between the reactant complexes, namely, $k_{34} \cong k_{43} \sim 10^{12}$ s^{-1}, $k_{31} \neq 0$, and $k_{41} \neq 0$.

Once the reactions have reached their completion, the O/C-product ratio can be calculated for each nitronate to provide quantitative measurements of the selectivity. Notice that this selectivity shall depend upon the values of the interconversion rates between the reactant complexes, namely, k_{34} and k_{43}. Thus, when $k_{34} = k_{43} = 0$, we have no equilibrium between the reactant complexes, which represents a purely kinetics control of the selectivity. Whereas for k_{34} and k_{43} obtained from the RRKM theory that provides values of the order of 10^{12} s^{-1}, a pre-equilibrium is established between the reactant complexes and concentration of the slower pathway can populate the faster one. We also can assume that neither the reactant complexes are in equilibrium ($k_{34} = k_{43} = 0$) nor they are in equilibrium with the separated reactants ($k_{31} = k_{41} = 0$). The selectivities for all these cases are presented in Table 4.8.

When the reaction pathways are independent ($k_{34} = k_{43} = 0$, $k_{31} = k_{41} = 0$), there is no selectivity because the reactant complexes RC@O and RC@C are formed at the same rate ($k_{13} = k_{14}$). Except for the nitronate **4**, [c-$(CH_2)_2CNO_2$]$^-$, where the rate of dissociation of the reactant complex is so small that the RC@O species becomes trapped and yields a C-:O-methylation ratio of 50:23 in the time-scale of the simulation. If the reactant complexes are allowed to dissociate back to the separated reactants (k_{31} and $k_{41} \neq 0$), then some selectivity towards the C-methylation is observed. Indeed, in this case, when these back-dissociation rates become comparable to the rates of the RC $\rightarrow$ PC steps, the C-methylation selectivity increases significantly because it is the fastest reaction pathway. In the limit where the reactant complexes RC@O and RC@C are in fast pre-equilibrium, the C-methylation is dominant and practically quantitative.

Table 4.8. Product ratios C-/O-methylation of the nitronates [$R_1R_2CNO_2$]$^-$ by CH_3I at different equilibrium situations between the reactant complexes. Calculations at available energy $E = E_0 + E_{thermal}$.

Product ratio	$k_{31} = k_{41} = 0$ $k_{34} = k_{43} = 0$	$k_{34} = k_{43} = 0$	$k_{34} \cong k_{43} \sim 10^{12} \ \text{s}^{-1}$
S_N2@C1: S_N2@O1	50:50	66:34	89:11
S_N2@C2: S_N2@O2 (*E*)	50:50	61:39	97:03
S_N2@C2: S_N2@O2 (*Z*)	50:50	70:30	97:03
S_N2@C3: S_N2@O3	50:50	94:06	100:0
S_N2@C4: S_N2@O4	50:23	97:03	100:0

It can be observed from Table 4.8 that, for the minimum available energy, the C-methylation mechanism is dominant and the selectivity towards this product increases with the substitution at the central carbon atom of the nitroalkane. The barriers for the interconversion of reactant complexes, namely, RC@C $\leftrightarrows$ RC@O, are very small and hence a larger rate of conversion establishes the equilibrium between these RCs. Although RC@O is slightly more stable than RC@C in reactions of **1** and **2**, the small RRKM rate for the conversion of RC@O into PC@O, the large conversion rates between the RCs and much larger RRKM rates for RC@C $\rightarrow$ PC@C

favors the $S_N2@C$ pathway. This diversion from the O-methylation pathway towards the C-methylation is best represented in Figure 4.18. It can therefore be inferred that the selectivity strongly depends on the equilibrium between the reactant complexes. The selectivity towards O-methylation pathway increases when there is no equilibrium between reactant complexes i.e. $k_{34} = k_{43} = 0$. A 50:50 selectivity was obtained when there is no equilibrium at all between the two RCs and between RCs and the reactants i.e. both $k_{34} = k_{43} = 0$ and $k_{31} = k_{41} = 0$. This is because both RCs complexes are formed at the same rate and therefore once formed they can only go towards the products. In the reaction of **4**, some of the concentration (27%) of RC@O is trapped and a $S_N2@C4:S_N2@O4$ selectivity of 50:23 for this reaction is obtained. Adding the trapped concentration gives a total concentration of 100%.
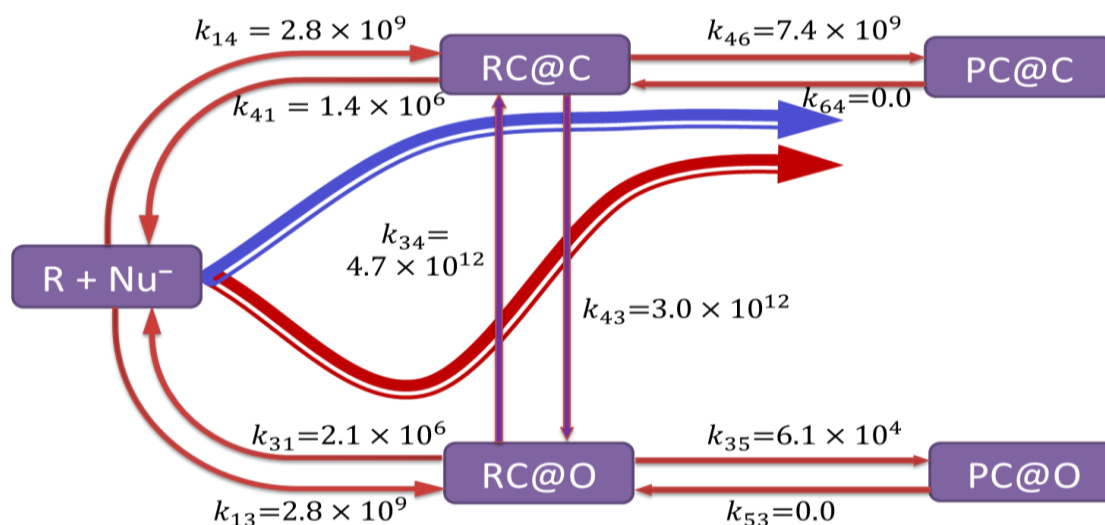

Figure 4.18. The diversion from the $S_N2@O$ pathway towards the $S_N2@C$ pathways in the reaction of **4**. The rate values are those calculated at the CBS (T,Q) level.

In flowing afterglow studies, as already mentioned, the concentration of the neutral substrate, [R], is *ca*. 10^4 times larger than the anion (nucleophile) concentration, [Nuc], typically [R] ~ 10^{12} cm^{-3} and [Nuc] ~ 10^8 cm^{-3} [71, 249]. Thus, the pseudo-first-order kinetics applies and the bimolecular reaction rate coefficient can be estimated with accuracy of ±25% [71, 249]. The numerical simulations of the kinetics mechanisms (Scheme 2) provide the temporal dependence

of the concentration of each species at both reaction pathways, which can be used to obtain the overall rate coefficient (k_{obs}) for comparison with the experimental value. The total rate constant of the reaction was calculated from the rate determining step, which in the present case is the decomposition of the reactant complexes **3** (RC@O) and **4** (RC@C), mathematically, for $[RC]^- \rightarrow [PC]^-$, the rate can be written as

$$-\frac{d[RC]^-}{dt} = k_{obs}[RC]^- \Rightarrow \frac{1}{[RC]^-}\frac{d[RC]^-}{dt} = \frac{d\ln[RC]^-}{dt} \cong -k_{obs} \Rightarrow k_{obs} \cong -\frac{d\ln[RC]^-}{dt}$$

In fact, plots of ln[RC] or ln(1 – [P]/[RC]$_0$) *vs.* time (*t*) have slopes equal to [Nuc]×k_{obs}, where [RC] and [P] are the overall concentrations of the reactant complexes and of the products at *t*, respectively, and [Nuc] is the concentration of the nitronate as shown in Figure 4.19. Unfortunately, this concentration was not provided in the experimental studies and direct comparisons with the calculated values are not feasible. Therefore, in Table 4.9 we present the relative rate coefficients calculated for the three cases considered as well as the experimental values.
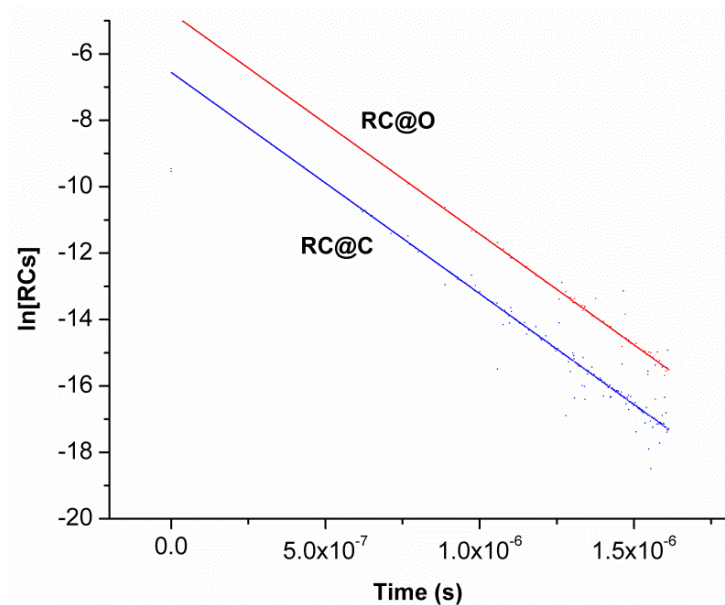
Figure 4.19. Temporal dependence of $[RC]^-$ when the two reactant complexes are in equilibrium i.e. $k_{34} \cong k_{43}$.

The slopes are -6.6668×10^6 and -6.6665×10^6 for RC@O and RC@C, respectively. As expected, these rates are the same because the RCs are in (fast) equilibrium and the rate of decomposition will be given the fastest rate. In equilibrium conditions, k_{obs} should be equal to the decay rate of either RC, that is, *ca.* 6.7×10^6 s^{-1}, because both provide the pathways responsible for depleting concentration of the nitronate, which is measured in the experimental kinetics.
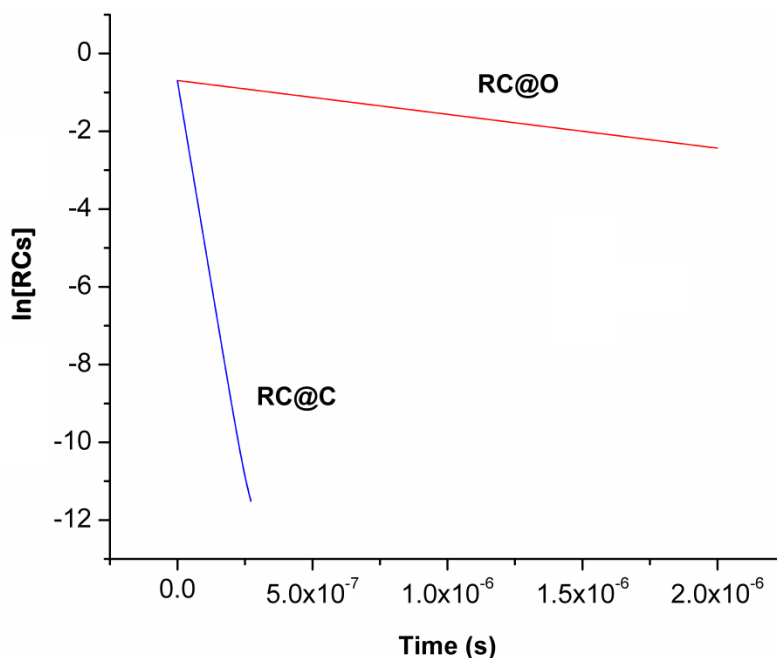
Figure 4.20. Temporal dependence of $[RC]^-$ when the two reactant complexes are not in equilibrium i.e. both $k_{31} = k_{41} = 0$ and $k_{34} = k_{43} = 0$.

The slopes are -8.7×10^5 and -4.1×10^7 for RC@O and RC@C, respectively. As expected, these rates practically coincide with $k_{35} = 8.6×10^5$ s^{-1} and $k_{46} = 4.2×10^7$ s^{-1} because the RC´s are not in equilibrium and thus they behave independently. In this case, k_{obs} should be equal to the fastest rate because it is the main pathway responsible for depleting concentration of deprotonated nitroalkane, which is measured in the experimental kinetics. Table 4.9 presents the calculated overall rate constants for the series of four reactions.

Table 4.9. Calculated and experimental relative rate coefficients for the $[R^1R^2CNO_2]^- + CH_3I$ gas-phase reactions. Calculations at available energy $E = E_0 + E_{thermal}$.[a]

Nitronate	$k_{31} = k_{41} = 0$ $k_{34} = k_{43} = 0$	$k_{34} = k_{43} = 0$	$k_{34} \cong k_{43}$ [b]	Experimental [71]
1	1.0	1.0	1.0	1.0
2-*E*	0.7	0.7	2.2	1.4
2-*Z*	0.7	0.7	1.8	
3	1.8	1.6	2.3	1.7
4	174	189	670	4.8

[a] Relative rate coefficients: $k_{obs}/k_{obs}(\mathbf{1})$. [b] Approximately 10^{12} s^{-1}.

The trend in the calculated relative rate coefficients considering the equilibrium between the reactants and reactant complexes (fourth column in Table 4.9) matches the experimental one. This is consistent with the experimental conditions where the kinetics measurements are performed in buffer gas (helium) at 40 Pa, which could allow the equilibrium between the reactant complexes to be reached. These trends show that the bimolecular reaction rate coefficients increase with the increase of crowdedness around the central carbon atom of the nitronate. However, the calculations do overestimate the substituent effects on the reaction rates, especially of nitronate **4**, $[c\text{-}(CH_2)_2CNO_2]^-$. These overestimations may be due to dynamics effects [231, 232] that are not taken into consideration in the RRKM calculations. For instance, reactions between methyl nitrate (CH_3ONO_2) and OH$^-$ can occur via S$_N$2 direct mechanism without forming the reactant complex [232]. In addition, for these reactions, the long-range electrostatic interactions can direct the nucleophilic attack and determine the selectivity [232]. Another relevant dynamics effect is the significant number of quasiclassical trajectories that present recrossings during S$_N$2 pathways [231, 232]. Therefore, for quantitative predictions of the relative and absolute rate coefficients of the $[R^1R^2CNO_2]^- + CH_3I$ gas-phase reactions, the inclusion of dynamics effects via, for instance, quasiclassical direct molecular simulations, is probably necessary.
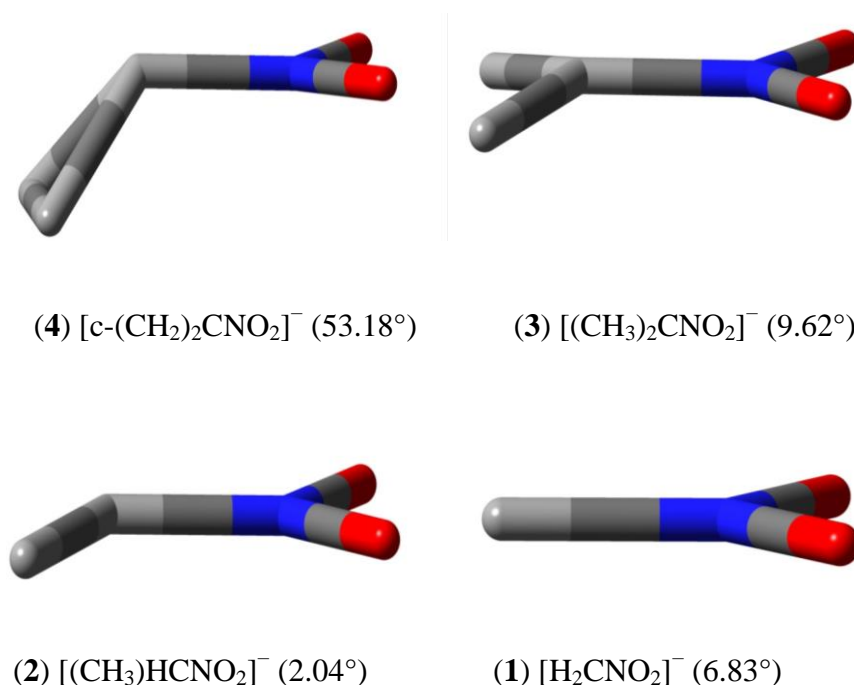
4.6 Explaining the reactivity

The agreement between the calculated and experimental trends suggests that the theoretical approach is reliable and may be used to explain the dependence of the rate coefficients upon the nitronates. Indeed, the increase of the rate coefficients with the increase of crowdedness around the central carbon atom of the nucleophile suggested selectivity towards the O-methylation of the nitronate [71]. However, the calculated energy profiles showed a high regioselectivity towards C-methylation, which is corroborated by the agreement between the experimental and calculated trends of the reaction rates. The explanation for this regioselectivity can be drawn from Bell-Evans-Polanyi principle [240–242], where the most exothermic pathway (C-methylation) should be preferred because it would have smaller activation energy. The differences in exorthermicity of C- and O-alkylated products were already qualitatively rationalized in terms of average bond enthalpies.

A complete explanation still needs to account for the increase of the reaction rate coefficients upon the increase of substituents at the central carbon atom of the nitronate.

The pyramidalization of the carbanion, the localized molecular orbitals and the molecular electrostatic potential maps (MEP) of the nucleophile helps to understand this trend of the nucleophilicity and hence the observed and calculated rates. It can be seen from the Figure 4.21 that it is most probably the pyramidalization of the structure of the nucleophile that makes the difference. The structures of the nucleophiles involved in the S_N2 reactions are illustrated in Figure 4.21.

(**4**) [c-(CH$_2$)$_2$CNO$_2$]$^-$ (53.18°)   (**3**) [(CH$_3$)$_2$CNO$_2$]$^-$ (9.62°)

(**2**) [(CH$_3$)HCNO$_2$]$^-$ (2.04°)   (**1**) [H$_2$CNO$_2$]$^-$ (6.83°)

Figure 4.21. The equilibrium structures of deprotonated nitroalkanes (nucleophiles) involved in the S$_N$2 reactions with CH$_3$I.

The structures of nucleophiles **1**, **2** and **3** are planar, whereas nitronate **4** presents a pyramidal geometry around the central carbon. This suggests that this central carbon should have a strong sp^2 character in nucleophiles **1**, **2** and **3**, while sp^3 hybridization would be expected in nucleophile **4**. The evidence comes from the small barrier to internal rotation in **4**.

The large barrier to internal rotation in the deprotonated nitroalkanes indicates the double bond character of C–N bond and hence its sp^2 type hybridization. When the nucleophilic attack occurs, the planar nucleophilic geometry has to be converted into a pyramidal type, that is, the change of hybridization of C–N bond from sp^2 to sp^3 occurs and thus exposing more the nucleophilic carbon to the substrate carbon in all the nucleophiles. Thus, it would be expected that as the pyramidalization in the starting nucleophile increases, the nucleophilic displacement would also increase. The dihedral angle (O–N–C–C in **2**, **3**, **4** and O–N–C–H in **1**) associated with the pyramidal geometry is found be to 6.83°, 2.04°, 9.62° and 53.18° in **1**, **2**, **3** and **4**, respectively. Therefore, the reaction rate increases with the increase of pyramidalization that in turn increases

with the increases of substitution. The structure of nitrocycloalkane is observed to be highly pyramidal and its smaller value of barrier to internal rotation indicates the sp^3 type hybridization of the central carbon. Therefore, the process of attack of nitrocycloalkane is much faster as compared to other nucleophiles and hence the largest value of $k(E)$ is observed for **4**. Because central C has sp^3 hybridization in the products, the largest reaction rate coefficient obtained with nitronate **4** may be explained by the smaller energy required to deform its electronic density from the reactant to the product.

The conversion of the planar nucleophilic structure into a pyramidal shape can be observed from the animated images drawn from the IRC calculation (Figure 4.22). The dihedral angle, O–N–C–C, associated with the pyramidal geometry of the nucleophile is found to be 3.8°, 17.8°, and 29.9° respectively, in the reactant complex, transition state and the product complex of S$_N$2@C3: $[(CH_3)_2CNO_2]^- + CH_3I$. The increment in the dihedral angle leads the structure from planar to a pyramidal one. These dihedral angles were observed to be 6.8°, 19.6°, and 32.7° in the reaction of **1** ($[H_2CNO_2]^- + CH_3I$); 2.0°, 15.4°, 29.2° in the reaction of **2** ($[CH_3HCNO_2]^- + CH_3I$); and 52.9°, 54.2°, 56.9° in the reaction of **4** ($[c-(CH_2)_2CNO_2]^- + CH_3I$), respectively in reactant complex, transition state and product complex. The largest rate of the reaction of **4** is evident from the smallest change in its dihedral angle in moving from RC to TS to convent into PC.
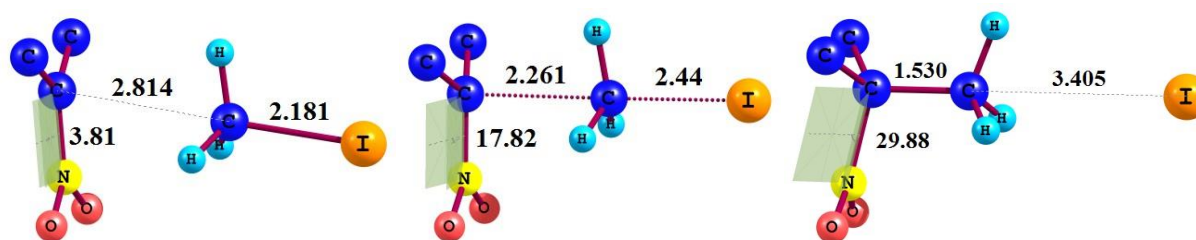
Figure 4.22. Equilibrium structure of the reactant complex (left), transition state (middle), and product complex (right) for the reaction of **3**; $[(CH_3)_2CNO_2]^- + CH_3I$. A representation of the change of geometry of the nucleophile from linear to pyramidal type. The dihedral angle O–N–C–C can be observed to increase while moving from reactants to products passing through intermediates.

Analyses using electron density and orbitals [114, 219, 122, 250] have provided inconclusive results for the hybridization character at the central carbon atom. However, vibrational analysis showed that the frequency of the normal mode related to the pyramidalization of the central carbon decreases significantly in the series **1**, **2** and **3**, as observed in Table 4.10.

Table 4.10. Vibrational properties of the central carbon pyramidalization mode of the nucleophiles calculated with the MP2/aug-cc-pVDZ method. Vibrational frequency ν (cm^{-1}), force constant k $(N\ m^{-1})$ and reduced mass μ (amu).

Property	1	2	3	4
ν	326	155	87	228
k	7.88	4.85	0.68	10.87
μ	1.26	4.08	1.53	3.53

This trend matches perfectly the calculated and experimental trends in reactivity. In fact, the decrease of this vibrational frequency upon the increase of substituents is directly related to a decrease of the force constant and an increase of the reduced mass, where the former has a larger effect. Steric effects between the substituents at the central carbon atom are probably the reason for the significant decrease of the force constant in the series **1**, **2** and **3**. Thus, thermal excitation of this low-frequency mode is more likely, which causes the reaction to accelerate because the nitronate would be more apt to react. In fact, because this normal mode can couple with the intermolecular mode of the S_N2 pathway [231, 232, 237, 238], the direct mechanism without the formation of the reactant complexes also becomes more probable as the frequency of pyramidalization mode decreases.

Conclusion

Methylation of $[R^1R^2CNO_2]^-$, where $R^1 = R^2 = H$ (**1**), $R^1 = CH_3$ and $R^2 = H$ (**2**), $R^1 = R^2 = CH_3$ (**3**); and $R^1 + R^2 = $ c-$(CH_2)_2$ (**4**), by CH_3I was studied by *ab initio* MP2/CBS method, RRKM theory and kinetics simulations. Contrary to a previous proposal for the reaction mechanism, the C-methylation is the thermodynamics and kinetics preferred pathway. This is corroborated by the agreement between the calculated and experimental reactivity trend **4** $\gg$ **3** $>$ **2** $>$ **1**. The regioselectivity towards the C-alkylation is explained by the much larger exothermicity of this reaction channel compared to the O-alkylation. The increase of reactivity upon the increase of crowdedness of the central carbon atom is explained by differences of sp^3 character at this atom and the decrease of the vibrational frequency associated with pyramidalization around this carbon atom.

Chapter 5

Alkylation of nitronates in solution

5.1 Introduction

Based on the results obtained for methylation of alkylnitronates in the gas-phase, namely, the regioselectivity towards C-alkylation, these reactions became relevant to ascertain the importance of the solvent effects in determining this regioselectivity. For instance, the $[MeCHNO_2]^-$ + Me_3O^+ reaction in dichloromethane yields exclusively the O-methylated product [251], as well as the $[XC_6H_4CHNO_2]^-$ + MeOBs reaction in 80:20 DMF:water (v/v) [63]. Thus, comparing the former reaction with $[MeCHNO_2]^-$ + MeI in the gas-phase arises interesting questions regarding if the change in regioselectivity is due to the alkylating agent (Me_3O^+ × MeI) and/or the solvent effects.

In addition, B3LYP/6-31+G(d) calculations for the $[XC_6H_4CHNO_2]^-$ + MeCl reactions in the gas-phase give activation enthalpies (with respect to the separated reactants) for O-methylation *ca*. 2 kcal/mol (8 kJ/mol) smaller than the corresponding C-methylation, which were used to corroborate the experimental regioselectivity towards the O-methylation. Therefore, the comparison with the $[MeCHNO_2]^-$ + MeI reaction suggests that exchange of an alkyl by an aryl group in the nitronate changes the regioselectivity or the choice of the computational method (B3LYP × MP2 or 6-31+G(d) × aug-cc-pVDZ) determines the selectivity. It is noteworthy that *E*/*Z* stereochemistry of the double bond in the O-methylated products (MeCH=N(O)OMe and $XC_6H_4CH=N(O)OMe$) was not determined for the alkylnitronate [63], whereas the *Z*-isomer was inferred from the relative stability calculated with the B3LYP/6-31+G* method [63]. However, if the stereoselectivity is kinetically then this assignment may be incorrect and more detailed experimental and computational analyses are warranted.

Exploring these reactions computationally in the gas-phase and solution could be very rewarding by establishing the origin (alkyl or aryl groups in the nitronate, solvent effects, alkylating agent, etc.) of their regio- and stereo-selectivity and thus providing guidelines for designing, for instance, organocatalysts, axillary chiral agent, and blocking species to the nitro group.

5.2 [XC$_6$H$_4$CHNO$_2$]$^-$ + MeCl reactions

The reactions of substituted arylnitronates [XC$_6$H$_4$CHNO$_2$]$^-$ (X = *p*-MeO, *p*-Me, *m*-Me, H, *p*-Cl, *m*-F, *m*-Cl, *p*-CF$_3$, *m*-NO$_2$) with MeOBs (methyl *p*-bromobenzenesulfonate) were investigated experimentally in three solvent systems: DMF, 80% (v/v) aqueous DMF, and 90% (v/v) aqueous MeOH [63]. The experimental results show that the O-methylation is preferred because no C-methylated product was detected in ^{1}H NMR. For the [HC$_6$H$_4$CHNO$_2$]$^-$ nitronate, the highest *Z:E* ratio of 6.7:1.0 was obtained in DMF with a conversion of 94.7% after 50 minutes of reaction. The *Z:E* ratio was determined by ^{1}H-NMR assuming the stereoisomer *Z* was preferred because it was calculated by B3LYP/6-31+G* to be 18.9 kcal/mol (79.0 kJ/mol) more stable than the respective *E*-isomer, in the gas-phase. Very similar results were observed for the substituted arylnitronates [XC$_6$H$_4$CHNO$_2$]$^-$ with X = *p*-MeO, *p*-Me, *m*-Me, *p*-Cl, *m*-F, *m*-Cl, *p*-CF$_3$, *m*-NO$_2$. In addition, experimental kinetics show that the reactions in DMF are *ca*. five times faster than that in aqueous DMF that may be due to the stabilizing solvent effects of the ionic and polar reactants in aqueous DMF. However, it seems that the nature of solvent does not change the C/O selectivity.
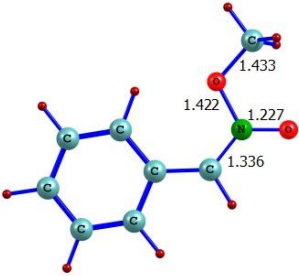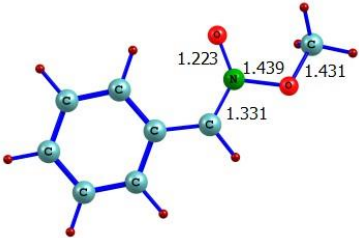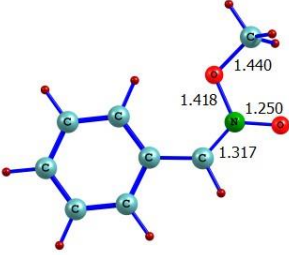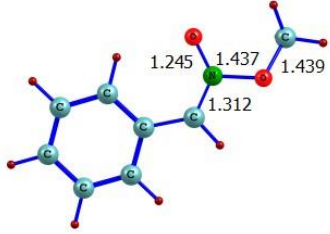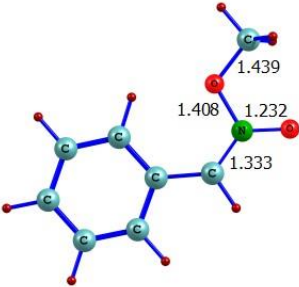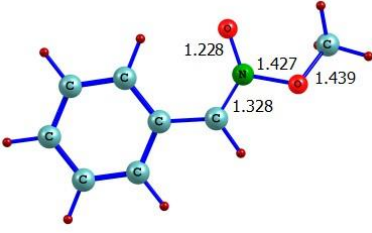
The reactions of substituted arylnitronates [XC$_6$H$_4$CHNO$_2$]$^-$ with MeCl and with MeOSO$_2$Me as methylating agents were investigated with B3LYP/6-31+G* in the gas-phase. The calculations showed kinetics preference of O-methylation pathways because the activation energy barriers for this pathway are 2-4 kcal mol^{-1} (4-7 kJ/mol) lower than the respective C-methylation [63]. However, the C-methylation is calculated to be thermodynamically preferred because the C-methylated products are 13-15 kcal mol^{-1} (54-63 kJ/mol) more stable than the respective O-methylated products [63]. It is important to emphasize that the calculated kinetics preference of O-methylation was performed in the gas-phase, while the experimentally observed selectivity was in solution. Moreover, comparison with our previous calculations for the [MeCHNO$_2$]$^-$ + MeI reactions in the gas-phase where C-methylation were calculated as kinetics and thermodynamics preferred pathway, arises concerns about the reliability of the B3LYP/6-31+G* method.

Thus, given the limitations of the B3LYP/6-31+G* method regarding thermokinetics of S$_N$2 reactions [63], we have investigated the reactions between nitronates [XC$_6$H$_4$CHNO$_2$]$^-$ (X = *p*-MeO, H, *p*-NO$_2$) with MeCl using more accurate methods such as MP2/6-311+G(d,p) and

B2PLYP/6-311+G(d,p). B2PLYP method was used based on its excellent performance in the assessments for the X^- + CH_3ONO_2 (X = OH, F, CH_2CN) reactions in the gas-phase [233].

Initially, the relative stability of Z and E stereoisomers for the product of O-methylation of $[HC_6H_4CHNO_2]^-$, namely, Z-$C_6H_5CH=N(O)OMe$ and E-$C_6H_5CH=N(O)OMe$ was determined with different quantum chemical methods. The structures and relative energies are presented in Table 5.1.

Table 5.1 Calculated structures and relative energies of Z and E stereoisomers in DMF.

Method	Z-$C_6H_5CH=N(O)OMe$	E-$C_6H_5CH=N(O)OMe$	$\Delta G^{a)}$ (kJ/mol)
B3LYP[b]			−10.2 Gas-phase: −16.9
B2PLYP[c]			−13.8
MP2[d]			−53.1

a) $\Delta G = G(E/\text{isomer}) - G(Z/\text{isomer})$, b) B3LYP/6-31+G(d), c) B2PLYP/6-311+G(d,p), d) MP2/6-311+G(d,p).

For the B3LYP/6-31+G(d) gas-phase calculations, we find that the *E*-isomer ($E_{tot} = -515.376832$ E_h) is 15.5 kJ/mol more stable than the *Z*-isomer ($E_{tot} = -515.3709245$ E_h), whereas in ref. [63] it is stated "B3LYP/6-31+G* calculations showed that the *Z*-isomer is 18.9 kcal/mol more stable than the *E*-isomer." Indeed, the structure of the *Z*-isomer presented in the Supporting Information file of ref. [63] is a minimum; however, the electronic total energy (-515.200874 E_h) was not reproduced. Because the larger stability of the *Z*-isomer was used to assign the *Z:E* ratio and stereoselectivity, this assignment as well as the stereoselectivity need to be revisited and revised. In DMF solution, all methods indicated that the product with *E* stereochemistry is the most stable, particularly, for the MP2/6-311+G(d,p).

Regarding the regioselectivity of the methylation of arylnitronates, Figure 5.1 presents the transition state structures of C-methylation and O-methylation pathways of the $[XC_6H_4CHNO_2]^-$ + CH_3Cl reaction in the gas-phase and in solution. The figure does not show any significant difference in the geometry of transition states in the two phases.

TSC (solution phase)   TSC (gas-phase)

TSO(*E*) (solution phase)   TSO(*E*) (gas-phase)
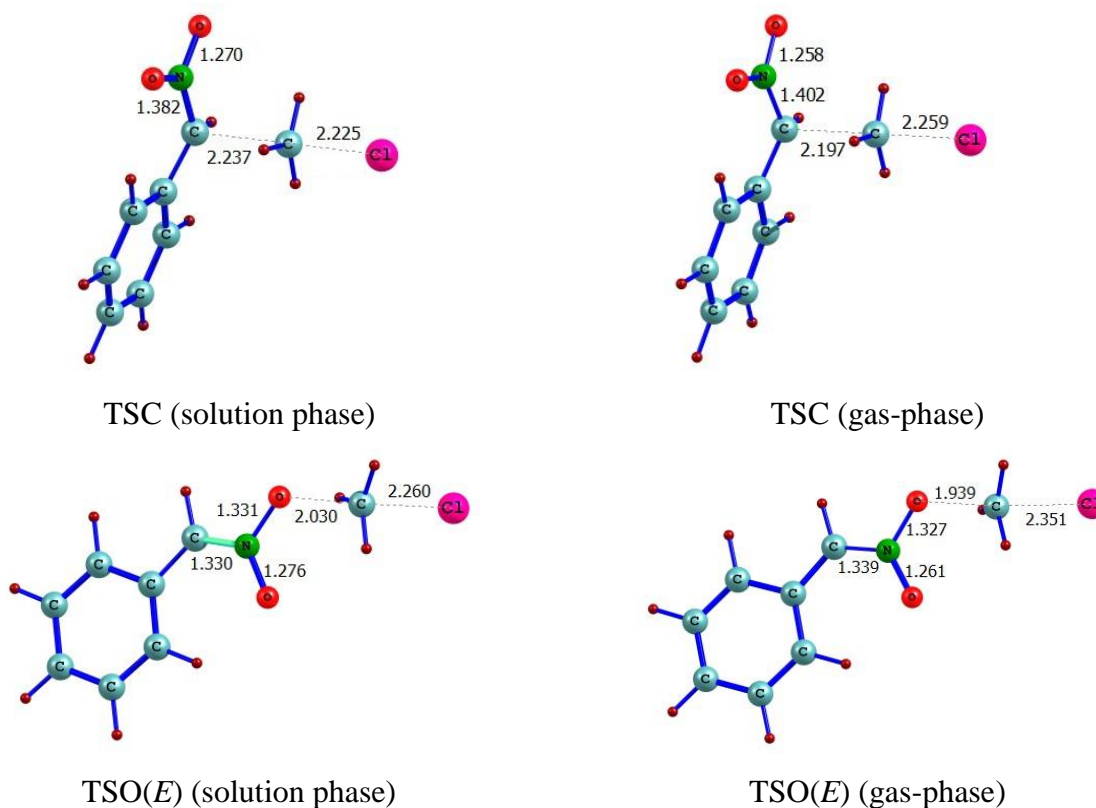
Figure 5.1 Transition state structures for C-methylation and O-methylation pathways of $[XC_6H_4CHNO_2]^-$ (X = H) + CH_3Cl in the gas-phase and in DMF.

It can be observed that the transition state involved in C-methylation (TS@C) in DMF is an earlier transition state, as it resembles more the reactants, than the gas-phase transition state, because it appears more like the products and hence a characteristic of late transition state. A similar trend was observed for the transition states involved in the O-methylation pathway. The differences between the C–C and C–O forming bonds in DMF and gas-phase are 0.04 and 0.09 Å for C- and O-methylation, whereas this difference for the C–Cl breaking bond is –0.03 and –0.09 Å. This shows that the O-methylation pathway is more affected by the solvent, which may be responsible for changing the regioselectivity. In fact, these results are very interesting, because they suggest that the regioselectivity may be controlled by changing the solvent (polarity, protic, etc.).

The free energy of activation and of reactions found for the studied reactions are presented in Table 5.2, while the potential energy profiles in the gas-phase and in DMF are depicted in Figure 5.2.

Table 5.2 Calculated activation and reaction free energies (kJ mol^{-1}) for the reactions [XC$_6$H$_4$CHNO$_2$]$^-$ + CH$_3$Cl (X = H, p-MeO, p-NO$_2$) at the B2PLYP/6-311+G(d,p) level. The values in parenthesis are those calculated in gas-phase. The barrier heights are calculated relative to the separated reactants.

X	C-methylation		O-methylation (E)		O-methylation (Z)	
	$\Delta^{\ddagger}G$	$\Delta_r G$	$\Delta^{\ddagger}G$	$\Delta_r G$	$\Delta^{\ddagger}G$	$\Delta_r G$
H	103.3 (74.1)	–137.7 (–60.7)	102.1 (70.7)	–47.7 (23.4)	107.5 (75.7)	–33.9 (39.3)
p-MeO	102.5 (74.9)	–143.5 (–69.9)	97.9 (68.2)	–54.0 (14.6)	103.3 (72.8)	–37.7 (32.2)
p-NO$_2$	114.6 (104.6)	–111.3 (13.8)	112.1 (100.8)	–26.8 (90.8)	115.9 (108.4)	–11.3 (101.7)
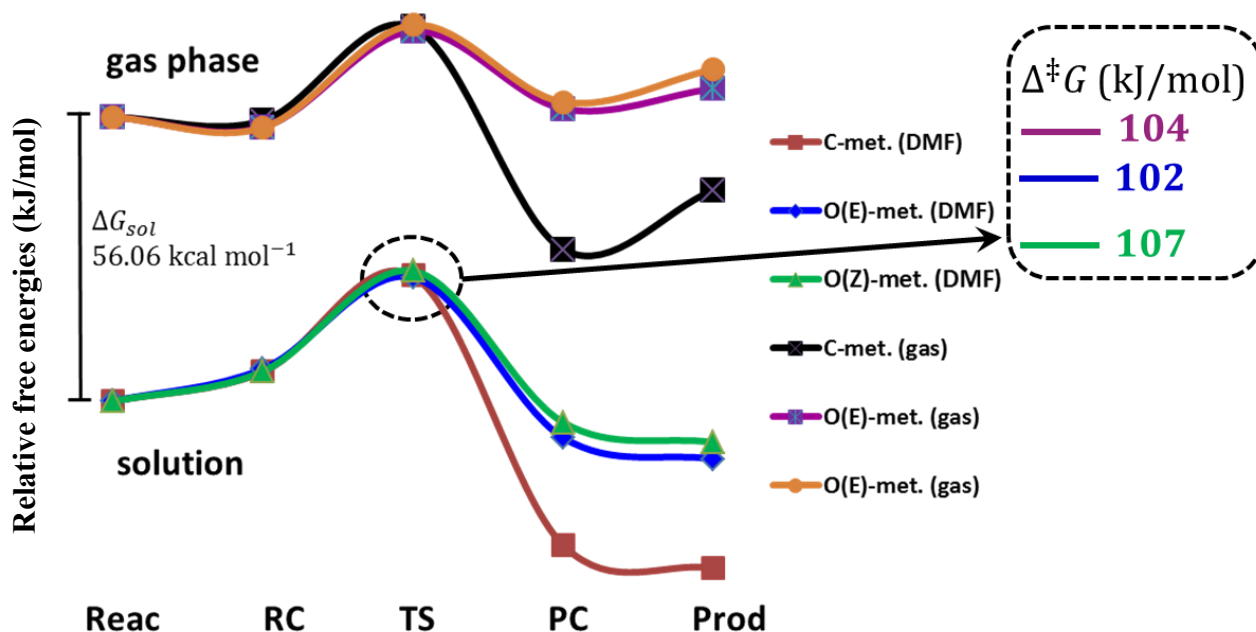
Figure 5.2. The potential energy profiles for the reaction pathways of $[XC_6H_4CHNO_2]^- + CH_3Cl$ (X = H) in the gas-phase and in DMF.

It can be observed from Table 5.2 and Figure 5.2 that the reactions in DMF are exothermic; however, in gas phase the exothermicity decreases and, in fact, the O-methylation pathways are calculated to be endothermic. In addition, from Table 5.2, we observe that the methylation of nitronates $[XC_6H_4CHNO_2]^-$ (X = H, *p*-MeO, *p*-NO$_2$) by MeCl in the gas-phase and in DMF shows a slight regioselectivity towards O-methylation for the *E*-stereoisomer. However, considering that the methylating reagent used in the experiments was methyl *p*-bromobenzenesulfonate (MeOBS), which is much more reactive than MeCl, it should thus be expected an increase the calculated selectivity, improving the agreement with the experimental observations. Indeed, such calculations are in progress and constitute one of the perspectives of this research.

Regarding the substituent effects, we observe from Table 5.2 that electron-withdrawing groups increase the activation energy, namely, $\Delta^\ddagger G = 97.9 < 102.1 < 112.1$ kJ/mol for X = *p*-MeO, H and *p*-NO$_2$, respectively, for O-methylation and *E*-isomer. This is consistent with the experimental observations where the rate constant ($k_{obs} \times 10^{-3}$ s^{-1}) is 2.00 ± 0.08, 1.24 ± 0.05 and

0.30 ± 0.006 for X = *p*-MeO, H and *p*-NO$_2$, respectively, at 25 °C in DMF with MeOBs [63]. This trend is also consistent with the σ values (electron donating or withdrawing ability) of these substituents, namely, σ = –0.12, 0.0 and 0.91 for *p*-MeO, H and *p*-NO$_2$, respectively [242]. Indeed, this electron-donating/withdrawing effect can be correlated to the Mulliken atomic charges of the central carbon and the oxygen atoms of the –NO$_2$ group in the nitronate [XC$_6$H$_4$CHNO$_2$]$^-$ as presented in Table 5.3.

Table 5.3 Mulliken atomic charges at the central carbon and the oxygen atoms of the –NO$_2$ group in the nitronate [XC$_6$H$_4$CHNO$_2$]$^-$.[a]

| X	C1	O3	O4
p-MeO	–0.323	–0.283	–0.422
H	–0.624	–0.292	–0.403
p-NO$_2$	–0.357	–0.202	–0.337

[a] atomic labels
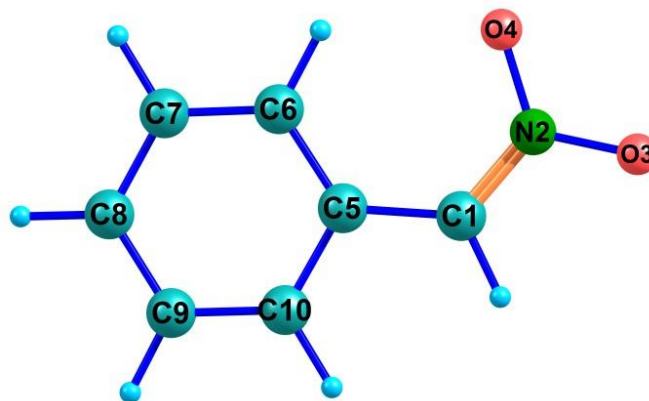
Figure 5.3 Atomic labeling of the nucleophile [XC$_6$H$_4$CHNO$_2$]$^-$ (X = H).

Notice that the methylation at O3 and O4 will lead to the *E*- and *Z*-stereoisomer, respectively. It can be observed from Table 5.3 that the Mulliken atomic charges at O3 and O4 increase (become

less negative) as the substituent becomes more electron-withdrawing, in a similar trend of increasing reaction rates. It is noteworthy that despite the limitations of the Mulliken atomic charges they do correlate quite well with the calculated activation energies for the O-methylations and with the observed trends of the experimental reaction rates upon the substituents.

5.3 $[MeCHNO_2]^-$ + Me_3O^+ reactions

Another evidence of the preference of O-methylation in solution arises from the methylation of nitronate $[MeCHNO_2]^-$ with trimethyloxonium [251]. Notice that stereochemistry of this reaction was not determined and only an *E:Z* ratio of 1:5 or 5:1 was obtained from ^{1}H NMR. Therefore, we have investigated this reaction regiochemistry (C- and O-methylation) and stereochemistry (*E* and *Z*) by quantum chemical methods in the gas-phase and in dichloromethane. The calculated potential energy profiles at B2PLYP/6-311+G(d,p) level in the gas-phase and in dichloromethane are presented in Figure 5.4.
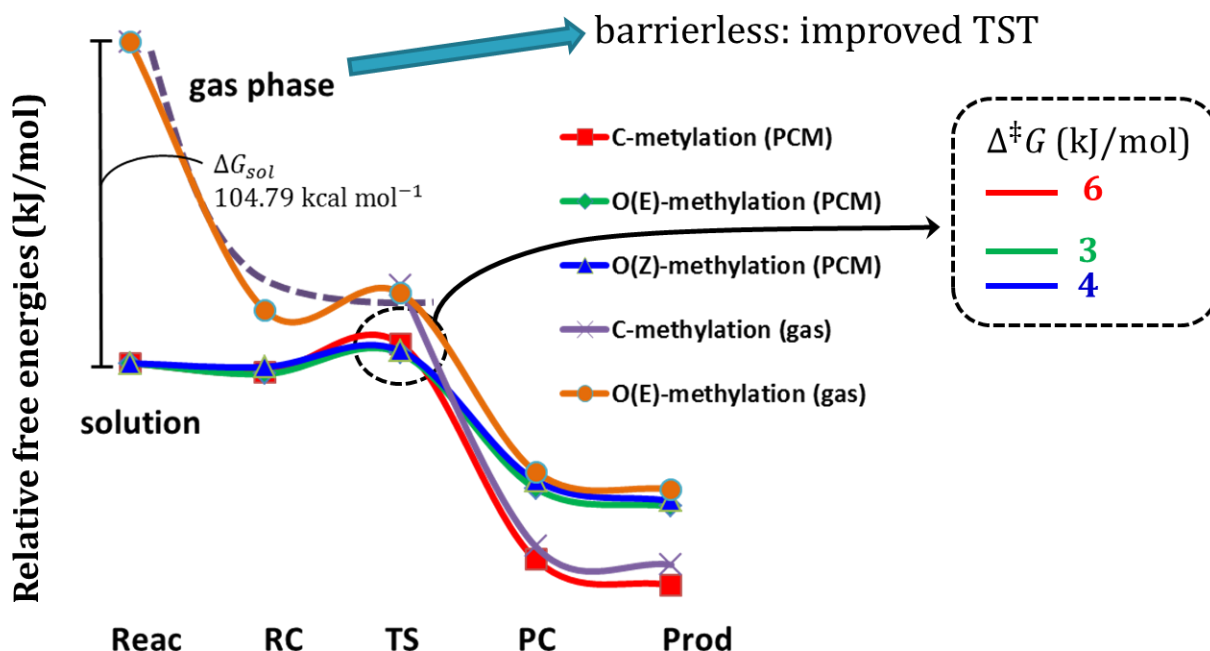
Figure 5.4. The potential energy profiles for the reaction pathway of $[MeCHNO_2]^- + Me_3O^+$ reactions calculated at B2PLYP/6-311+G(d,p) level in the gas-phase and in dichloromethane (DCM).

The calculated activation and reaction free-energies of $[MeCHNO_2]^- + Me_3O^+$ pathways in the gas-phase and in dichloromethane and of $[MeCHNO_2]^- + MeI$ in the gas-phase are presented in Table 5.4.

Table 5.4 Calculated activation and reaction free energies (kJ mol^{-1}) for $[MeCHNO_2]^- + Me_3O^+$ (oxonium) and + MeI reactions in the gas-phase and solution (dichloromethane) relative to separated reactants at the different theoretical levels.

	C-methylation		O-methylation (*E*)		O-methylation (*Z*)	
	$\Delta^\ddagger G$	$\Delta_r G$	$\Delta^\ddagger G$	$\Delta_r G$	$\Delta^\ddagger G$	$\Delta_r G$
$[MeCHNO_2]^- + Me_3O^+$ (oxonium) in dichloromethane						
B2PLYP[a]	26.4	-303.8	14.7	-195.8	16.9	-188.3
$[MeCHNO_2]^- + Me_3O^+$ (oxonium) in the gas-phase						
B2PLYP[a]	-332.3	-713.8	-342.8	-610.9	n.a.[f]	-606.3
$[MeCHNO_2]^- + MeI$ in the gas-phase						
B2PLYP[b]	32.6	-182.8	30.1	-84.1	35.6	-77.0
MP2[c]	34.7	-195.4	40.2	-79.1	44.4	-72.8
MP2/TZ[d]	23.8	-193.3	41.4	-79.9	46.4	-71.5
$[MeCHNO_2]^- + MeI$ in dichloromethane						
SP-MP2/TZ[e]	17.2	-209.6	41.8	-85.8	46.0	-77.8

[a] B2PLYP/6-311+G(d,p). [b] B2PLYP/6-31+G(d) for CHNS atoms and LANL2DZdp for I atom. [c] MP2/6-31+G(d) for CHNS atoms and LANL2DZdp for I atom. [d] MP2/aug-cc-pVTZ-PP. [e] Single-point calculations in dichloromethane. [f] Not available at the moment.
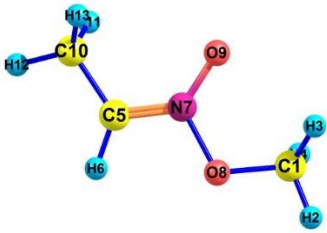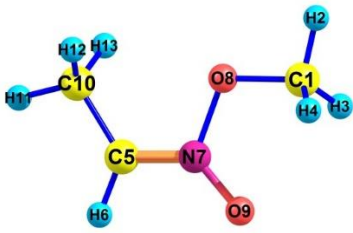
From Figure 5.4 and Table 5.4, B2PLYP/6-311+G(d,p) calculations for the methylation of $[MeCHNO_2]^-$ by Me_3O^+ yield a smaller activation energy for the O-methylation as compared to C-methylation in dichloromethane, which is supported by the experimental regioselectivity [251]

In addition, the results in Table 5.4 suggest that the origin of the regioselectivity of alkylation of nitronates in solution needs to be revisited [63], where the solvent effects, the nitronate and the alkylation agent may play decisive roles, which could provide new design strategies for controlling these reactions.

It is clear from the Table 5.4 and Figure 5.4 that smaller barrier is calculated at the B2PLYP/6-311+G(d,p) level for the $[MeCHNO_2]^- + Me_3O^+$ reaction in dichloromethane for O-methylation, whereas in the gas-phase practically there is no regioselectivity, because the transition states for the C- and O-methylation are almost degenerated. Thus, the calculated regioselectivity towards the O-methylation in solution is mainly due to the solvent effects. For the reactions in the gas-phase, at the B2PLYP/6-311+G(d,p) level, when the methylating reagent is changed from Me_3O^+ to MeI the reaction changes from no regioselectivity to slight preference towards the O-methylated product. However, this regioselectivity reverses towards the C-methylation when the calculations are performed with the MP2 method. Therefore, systematic and benchmark studies are needed to establish a reliable methodology for these reactions in the gas-phase and in solution. The reactant complexes for $[MeCHNO_2]^- + Me_3O^+$ reaction in gas-phase were not found as the two reactants react directly without forming a reactant complex.

Regarding the stereoselectivity of the $[MeCHNO_2]^- + Me_3O^+$ methylation reaction, the experimental ^1H NMR spectrum of MeCH=N(O)OMe show two peaks at δ 5.91 and 6.25 with a peak area ratio of 1:5 [251], measured in MeCH=N(O)OMe liquid. However, it could not be determined which *E* or *Z* stereoisomer was dominant. We thus used the WP04/aug-cc-pVTZ//MP2/aug-cc-pVTZ [252] method to calculate NMR chemical shifts and indirect spin-spin couplings of both isomers. The calculated chemical shifts of ^1H in the CH group are shown in Table 5.5 and compared to the experimental values.

Table 5.5 Calculated chemical shifts of ^{1}H in the CH group (H6) of the O-methylated product MeCH=N(O)OMe in the gas-phase and DMSO at the WP04/aug-cc-pVTZ//MP2/aug-cc-pVTZ level.

Chemical shift with respect to TMS		
	E-isomer	*Z*-isomer
Gas-phase	6.12	5.47
DMSO	6.43	5.79
Experimental[a)]	6.25 (area 5)	5.91 (area 1)

a) NMR measurement in neat MeCH=N(O)OMe liquid.

From Table 5.5 we can clearly assign the ^{1}H NMR peak with larger area (δ 6.25) to the *E* stereoisomer. This assigned stereochemistry is consistent with the smaller activation energy of the O-methylation leading to *E*-isomer product compared to either C-methylation or *Z*-isomer at the B2PLYP/6-311+G(d,p) level for the $[MeCHNO_2]^-$ + Me_3O^+ reaction in dichloromethane presented in Table 5.4.

Conclusion

Methylation reactions of $[MeCHNO_2]^-$ by Me_3O^+ (oxonium) and of arylnitronates $[XC_6H_4CHNO_2]^-$ (X = H, *p*-MeO, *p*-NO$_2$) by MeCl were investigated with quantum chemical methods in the gas-phase and in solution in order to determine the effects of the solvent, of the substituents in the nitronates, and of the alkylating agent. The results show regioselectivity towards O-methylation in the gas-phase and more significantly in solution (dichloromethane), which is in line with the experimental observation. In addition, it shows that the regioselectivity is highly dependent upon the reactivity of the alkylating agent. Solvent effects are also relevant

and usually change the regioselectivity towards O-methylation. The ^{1}H NMR assignment assisted by quantum chemical calculations suggest that *E*-stereoisomer product of the O-methylation of $[MeCHNO_2]^-$ by Me_3O^+ in dichloromethane is preferred. The calculations for $[XC_6H_4CHNO_2]^-$ + MeCl (X = H, *p*-MeO, *p*-NO$_2$) reactions in DMF show a slight regioselectivity towards O-methylation. However, considering that the methylating reagent used in the experiments was methyl *p*-bromobenzenesulfonate (MeOBS), which is much more reactive than MeCl, it should be expected an increase of the calculated selectivity. The calculations with methylating reagent MeOBS are in progress.

Chapter 6

Assessments of DFT Functionals and MP2 Method to Describe the Gas-Phase [$R^1R^2CNO_2$]$^-$ + CH_3I Reactions

6.1 Introduction

The design of organocatalysts and new reaction media for organic reactions require accurate and detailed knowledge of the mechanism [253, 254]. For instance, the alkylation of nitronates $[R^1R^2CNO_2]^-$ (R^1, R^2 = H, alkyl, aryl) can yield C-alkylated ($R^1R^2R^3CNO_2$) and O-alkylated ($R^1R^2C=N(O)OR^3$) products [53, 57]. The control of the regioselectivity (C- or O-alkylation) is essential to make this reaction viable for organic synthesis. In addition, C-alkylated products can be chiral, whereas O-alkylated products can present stereochemistry E and Z at the C=N double bond. Thus, developing new reaction media (solvent mixtures, alkylating agents, temperature, etc.) and (organo)catalysts for these reactions is relevant for expanding their scope of applications as well as controlling the different regio-, stereo-, and enatio-selectivity. These developments and design can be guided and aided by computational methods, specially, quantum chemistry approaches that may incorporate solvent effects and describe properly intermolecular interactions [253, 254]. Given the diversity of methods and models it is does relevant to ascertain their reliability for describing the alkylation of nitronates. To simplify the model, usually these reactions are studied in the gas-phase [71].

However, the regioselectivity could not be determined experimentally and high-level *ab initio* methods combined with RRKM theory and numerical method were employed to investigate the $[R^1R^2CNO_2]^- + CH_3I$ reactions in the gas-phase with $R^1 = R^2 = H$ (**1**), $R^1 = CH_3$ and $R^2 = H$ (**2**), $R^1 = R^2 = CH_3$ (**3**); and $R^1 + R^2 = c\text{-}(CH_2)_2$ (**4**) [255]. This approach has a high computational demand and is not practical for quasi-classical trajectory calculations [35] or for modeling larger systems including solvent and (organo)catalysts [253, 254]. Therefore, less demanding methods should be employed, however, their reliability and accuracy need to be ascertained in order to provide adequate and appropriated results either for describing dynamical effects or for modeling more complex systems.

Calculating energies of chemical processes with an accuracy of 1 kcal mol^{-1} (*ca.* 4 kJ mol^{-1}) or less (0.1–0.2 kcal mol^{-1} or 0.4–0.8 kJ mol^{-1} for relative energy of conformers) remains a challenge in computational thermochemistry and kinetics [256]. Chemical selectivities depend upon the differences in the activation energies of two or more competitive pathways such as the C- and O-alkylation regioselectivity of nitronates [255]. Therefore, accurate calculations of activation energies are important for establishing the reaction mechanisms, reactivities and selectivities as well as quantitative kinetics with transition state theory (TST) its generalizations and improvements, as well as the Rice-Ramsperger-Kassel-Marcus

(RRKM) theory. However, at the same time, the methods applied should not require large computational demand, because the scope of the reaction and of the mechanism usually requires extensive studies involving different substrates (*e.g.* steric and electronic effects) and in many cases, environment (mainly solvent) and dynamics effects. Thus, the highly accurate and computationally expensive *ab initio* wavefunction based methods are usually limited to small systems or models.

Over the past few decades Kohn-Sham (KS) formalism based on density functional theory (DFT) [182], especially global hybrid-DFT approaches [257–261] that include Hartree-Fock exchange energy contribution has become a very popular electronic structure tool for understanding and rationalize reaction mechanisms and selectivity due to their cost efficiency and accuracy [262]. In fact, the importance of these methods in computational chemistry (*e.g.*, thermochemistry and thermochemical kinetics) can hardly be overemphasized. However, there is a very large number of choices of DFT functionals with different accuracies, which immediately leads to the problem of selecting the most suitable functional(s) for a particular study (properties and systems). For instance, only a few KS-DFT methods have been shown to be appropriate to describe bimolecular nucleophilic displacement (S_N2) reactions [263–268]. On the other hand, the role of basis sets combined with effective core potential (ECP) cannot be ignored. A particular combination of a functional and an ECP/basis set determines the performance of such a computational model [269]. Therefore, care must be exercised when choosing basis sets and ECPs (in case of heavy atoms) for a particular functional. Indeed, we were unable to find systematic and consistent studies about the performance of wavefunction based MP2 method and DFT functionals combined with different ECP/basis sets to describe the methylation reactions.

Benchmarking was first performed by Pople and co-workers during the developments the G1, G2/97, G3/99 and G3/05 test sets focusing the atomization energies, electron affinities and ionization potentials [270–274]. Trulhar and co-workers later extended the idea by including other physical-chemistry properties such as reaction energies, barrier heights and non-covalent interactions [275–278]. Indeed, benchmarking is an important technique to evaluate the performance of quantum chemical methods and aid in the choice of the most appropriate methodology.

Several studies have shown disagreements between experimental reaction selectivities and the predictions based on the calculated barriers combined with statistical theories. These

disagreements were usually ascribed to the inaccurate prediction of the barriers and rarely to inadequacies of statistical approaches to those particular reactions [40, 279, 280]. However, more recently, the comparisons between experimental results and those obtained from direct dynamics simulations have identified some limitations of statistical approaches [35, 281, 282]. On the other hand, the energetics can now be calculated using highly accurate methods with complete basis set limit (CBS) approaches. Such discrepancies can, therefore, fairly be related to the limitations of statistical theories for those reactions [283–285].

Thus, the main goal of the present work is to perform a benchmark study for a variety of hybrid-DFT functionals and MP2 method with different ECPs/basis sets using CCSD(T)/CBS results to describe the $[R^1R^2CNO_2]^- + CH_3I$ reactions in the gas phase, where $R^1 = R^2 = H$ (**1**), $R^1 = CH_3$ and $R^2 = H$ (**2**), $R^1 = R^2 = CH_3$ (**3**); and $R^1 + R^2 = c\text{-}(CH_2)_2$ (**4**), as illustrated in Scheme 1. These reactions were selected because as mentioned earlier they show regioselectivity ($S_N2@C$ or C-alkylation and $S_N2@O$ or O-alkylation) and for asymmetric nitronates, such as, $[CH_3CHNO_2]^-$, the O-alkylation yields Z and E stereoisomers as shown in Scheme 6.1.
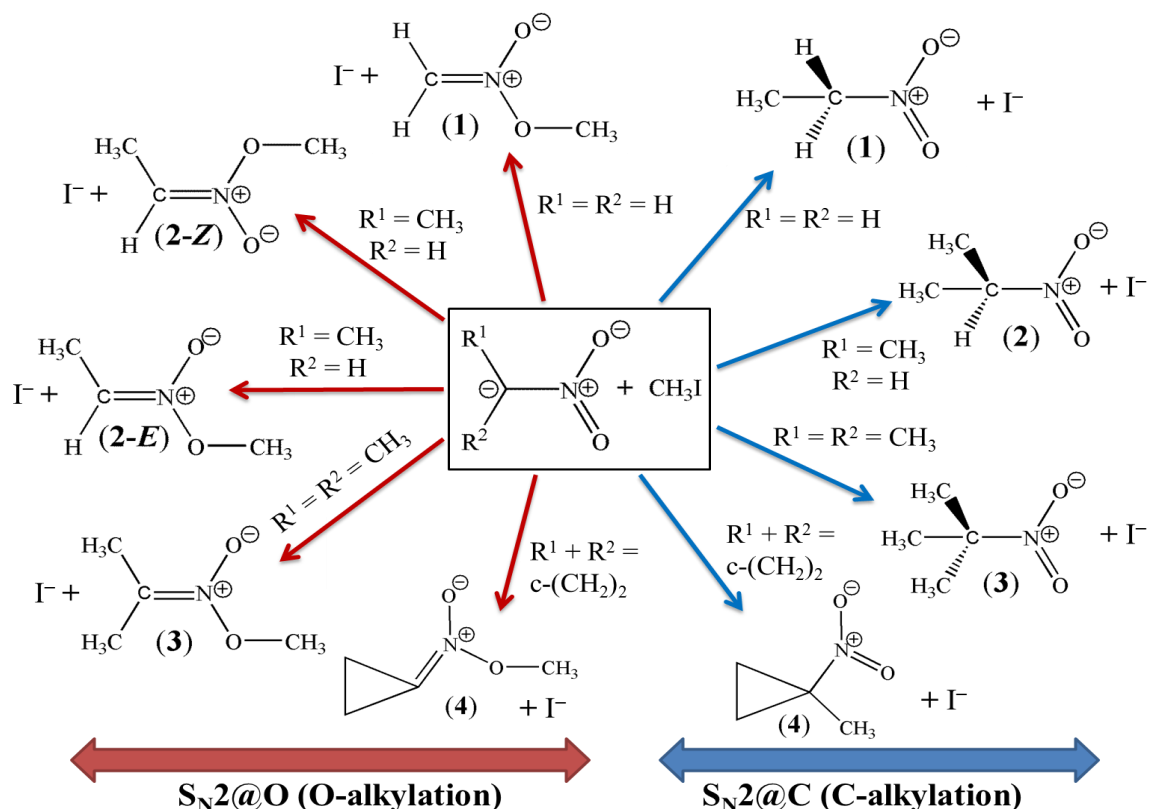
Scheme 6.1 Reaction channels for the alkyl-nitronates $[R^1R^2CNO_2]^-$, where $R^1 = R^2 = H$ (**1**), $R^1 = CH_3$ and $R^2 = H$ (**2**), $R^1 = R^2 = CH_3$ (**3**); and $R^1 + R^2 = c\text{-}(CH_2)_2$ (**4**), with iodomethane (CH_3I). For asymmetric nitronates such as **2**, the O-alkylation yields Z and E stereoisomers.

The selectivity of the S_N2 reactions involving different centers in the substrate, for instance, X^- + CH_3ONO_2 (X = OH, F, CH_2CN) yielding $S_N2@C$, $S_N2@N$ and $E2_{CO}$ products, has already been benchmarked [35]. However, different S_N2 pathways at centers in the nucleophile, such as, $[R^1R^2CNO_2]^-$ + MeI (Scheme 1), have not been studied systematically and used to ascertain the performance of molecular electronic structure methods.

Therefore, we tested several different combinations of hybrid-DFT functionals or MP2 and ECPs/basis sets (Table 6.1) through comparisons with CCSD(T)/CBS(D,T)//MP2/aug-cc-pVTZ reference results for all the reaction pathways illustrated in Scheme 6.1. The performance of these models was evaluated by calculating five statistical parameters comparing relative energies and structural properties. We found very few combinations (method + ECP/basis set) that provided accurate results, however, they all yielded the C-methylation pathway as the preferred one.

6.2 Methodology and Computational Details

A total of 23 different combinations of hybrid-DFT functionals or MP2 method and ECP/basis sets, described in Table 1, were assessed to describe the methylation of nitronates $[R^1R^2CNO_2]^-$ by CH_3I (Scheme 1) in terms of potential energy profiles (PEPs) and structures. More specifically, the following relative energies were determined and used in the assessments: i) the available energy ($\Delta_{RC}E$) to the reactant complex calculated as the energy difference between the reactant complex and the separated reactants; ii) the activation energy ($\Delta^{\ddagger}E$) determined as the difference between the transition state and the corresponding reactant complex energies, and iii) the reaction energy (Δ_rE) obtained as the difference between the energies of separated products and separated reactants. These relative energies were corrected by the corresponding zero-point vibrational energy (ZPE) contributions. Assessments of molecular structures were performed by the geometric parameters of the main stationary structures (reactant complexes and transition states) determined as the differences between the three rotational constants of the reference structure and that obtained with the method under assessment.

Table 6.1. List of methods (MP2 or DFT functionals and ECP/basis sets) assessed.

LAN[a]	DZ[b]	TZ[c]	CBS [286]
MP2 [170]	MP2	MP2	MP2/CBS(D,T)
		MP2 (SP)	MP2/CBS(T,Q)
		MP2/QZ (SP)[d]	
B2PLYP [258]	B2PLYP	B2PLYP (SP)	
mPW2PLYP [257]	mPW2PLYP	mPW2PLYP (SP)	
		B2GPPLYP [259] (SP)	
M06-2X [277]	M06-2X	M06-2X (SP)	
B3LYP [260, 261]	B3LYP	B3LYP (SP)	
	CCSD(T)[287] (SP)	CCSD(T) (SP)	CCSD(T)/CBS(D,T)

[a] 6-31+G(d) for C, H, N, O and LANL2DZdp/ECP ECP for I atom [288, 289]. [b] aug-cc-pVDZ for C, H, N, O and aug-cc-pVDZ-PP for I atom [211, 212]. [c] aug-cc-pVTZ for C, H, N, O and aug-cc-pVTZ-PP for I atom [213]. [d] SP-MP2/aug-cc-pVQZ-PP, namely aug-cc-pVQZ for C, H, N, O and aug-cc-pVQZ-PP for I atom [214].

Structural and vibrational frequency calculations were performed with second-order Møller-Plesset perturbation theory (MP2) method [170] using the aug-cc-pVTZ-PP basis set [213], MP2/TZ, which provided the ZPE corrections. The stationary structures for all reaction pathways were characterized by their force constants and the transition states by their intrinsic reaction coordinates (IRCs) [290] that ascertained the connection between the proper reactant and product complexes. Using the MP2/TZ structures, CCSD(T) single-point energy calculations were performed with aug-cc-pVXZ-PP (X = D and T) basis sets, which were employed in the extrapolation procedure to complete basis set (CBS) limit, CBS(D,T) [286] with an optimized two-point model [291, 292]. These CCSD(T)/CBS energies were used as benchmark values to test the methods listed in Table 1. All the calculations were performed with the Gaussian09 program [209] employing its default criteria.

The statistical parameters MUE, MSE, MRE and CI were determined as,

$$\text{MUE} = \frac{1}{n}\sum_{i=1}^{n}|d_i| \qquad\qquad \text{MSE} = \frac{1}{n}\sum_{i=1}^{n}d_i$$

$$\text{MRE (\%)} = \frac{100}{n} \sum_{i=1}^{n} \frac{d_i}{a_i} \qquad S_d = \sqrt{\frac{\sum_{i=1}^{n}(d_i - \text{MSE})^2}{n-1}}$$

$$\text{CI} = \text{MSE} \pm t_{\alpha/2} \frac{S_d}{\sqrt{n}}$$

where $d_i = a_i - b_i$, and a_i and b_i are the properties (relative energies or moment of inertia) of the ith stationary structure calculated at the CCSD(T)/CBS level and with the methods under assessment, respectively. S_d is the standard deviation in these differences d_i, $t_{\alpha/2}$ is the critical t-value obtained from t-table for the two tails with $n-1$ degress of freedom, and $\alpha = 0.01$ and 0.05 is the statistical significance of 99% and 95% confidence of interval, respectively [293]. The BW [256] parameter simply counts the number of times that the method provided the best and the worst results within the set of methods under assessment.

6.3 Results and Discussion

The results are presented and discussed in three parts: comparisons of calculated reaction profiles, structural accuracy and relative energy assessment. Usually, the mean unsigned error (MUE) and the mean signed error (MSE) are employed in assessments of quantum chemical methods, however, a recent benchmark study [233] suggested that the method can be better assessed through the use of MSE and MUE descriptors with the best and worst (BW) criterion and confidence interval (CI). Such a combination of criteria takes into account accuracy as well as robustness of the method. In addition, because the activation energies of the reactions in Scheme 1 span a reasonably large range, namely, 3.2 to 12.7 kcal mol^{-1} (13.4 to 53.1 kJ mol^{-1}) at CCSD(T)/CBS level, which strongly affect the selectivity, the mean relative error (MRE) was also taken into consideration in the present assessment.

6.3.1 Comparisons of calculated reaction energy profiles

The reaction energy profiles calculated with the reference method (CCSD(T)/CBS(D,T)//MP2/aug-cc-pVTZ-PP) and other selected methods for the methylation of alkyl-nitronates are depicted in Figures 6.1 through 6.4. The nucleophilic displacements can occur at the carbon (C-methylation or $S_N2@C$) or at oxygen (O-methylation or $S_N2@O$) atoms of the nitronates. Their reaction profiles display the typical double-well/single barrier behavior of S_N2-type reactions in the gas phase. These reactions

form reactant ion-dipole complexes that are more stable than the separated reactants, which were taken as zero energy in each reaction profile. The reactant complexes formed at the carbon (RC@C) and at the oxygen (RC@O) atoms are activated and cross the barrier associated with their respective transition states (TS@C and TS@O) to yield the corresponding product ion-dipole complexes (PC@C and PC@O), which dissociate to give separated products.

The O-methylation of $[CH_3HCNO_2]^-$ (**2**) can occur via two different pathways TS@O (*E*) and TS@O (*Z*) to form isomers *E* and *Z*,(see Scheme 1), because the two oxygen atoms are not symmetric, and thus should be treated separately.

All the reactions are found to be highly exothermic with the C-methylations being *ca*. 104 kJ mol^{-1} more exothermic than the O-methylations, expect for **4**, where the exothermicity difference is 182 kJ mol^{-1} calculated at CCSD(T)/CBS//MP2/TZ level. The larger exothermicities of the C-methylation pathways is mainly due to bond energy differences of the C- and O-methylated products. These larger exothermicities of the C-methylated products have a profound impact in the kinetics, because they lead transition states *ca*. 15 kJ mol^{-1} more stable than the O-methylation pathways, in accordance to the Bell-Evans-Polanyi principle [240–242]. The results obtained with the wavefunction based methods MP2/TZ, MP2/TZ (SP), MP2/QZ (SP), MP2/CBS(D,T), MP2/CBS(T,Q), CCSD(T)/DZ (SP) and CCSD(T)/TZ (SP) are nearly identical and are in very close agreement with the reference method, while the DFT functionals B3LYP and B2PLYP show the largest deviation from the reference method, as can be visualized in Figures 6.1–6.4.
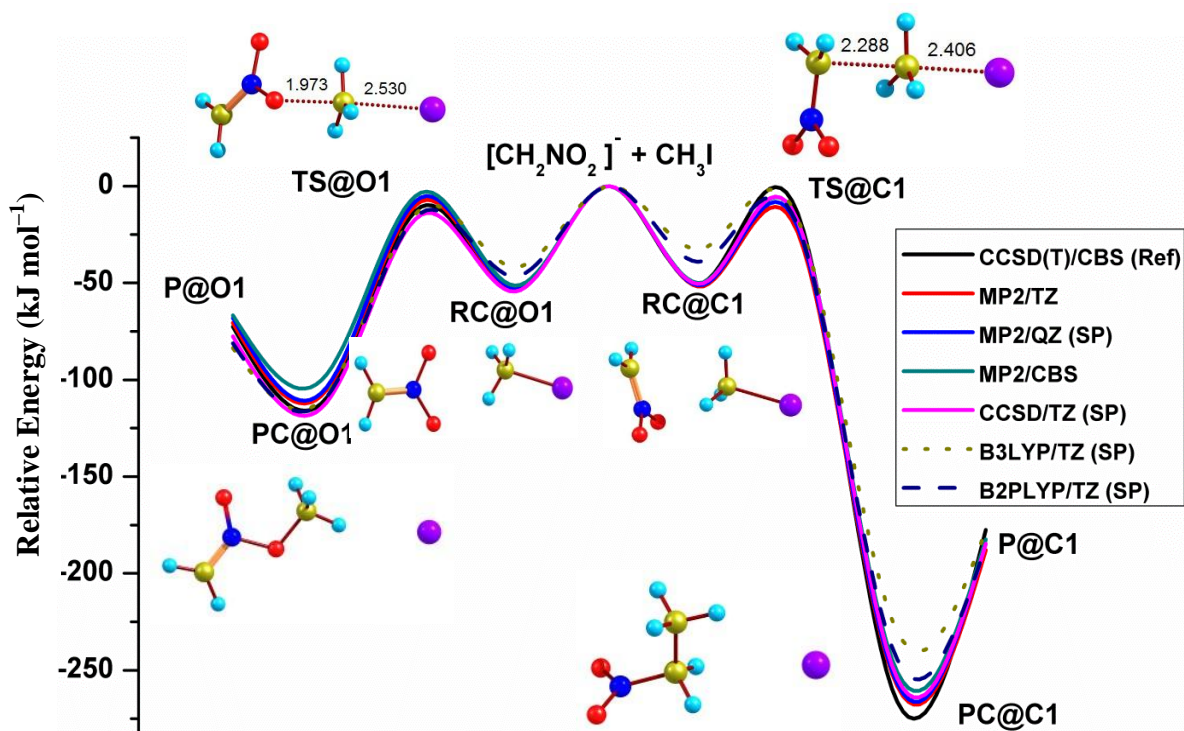
Figure 6.1. Energy profiles and selected structures (at the MP2/TZ level) of the $[CH_2NO_2]^-$ (**1**) + CH$_3$I reaction in the gas phase. The pathways through the oxygen (O-methylation or S$_N$2@O) and the carbon (C-methylation or S$_N$2@C) atoms of the nucleophile (nitronate) were considered. The calculations are single-point energies with selected methods and the reference CCSD(T)/CBS(D,T). Energies (in kJ/mol) include the zero-point vibrational corrections and distances in 10^{-10} m.
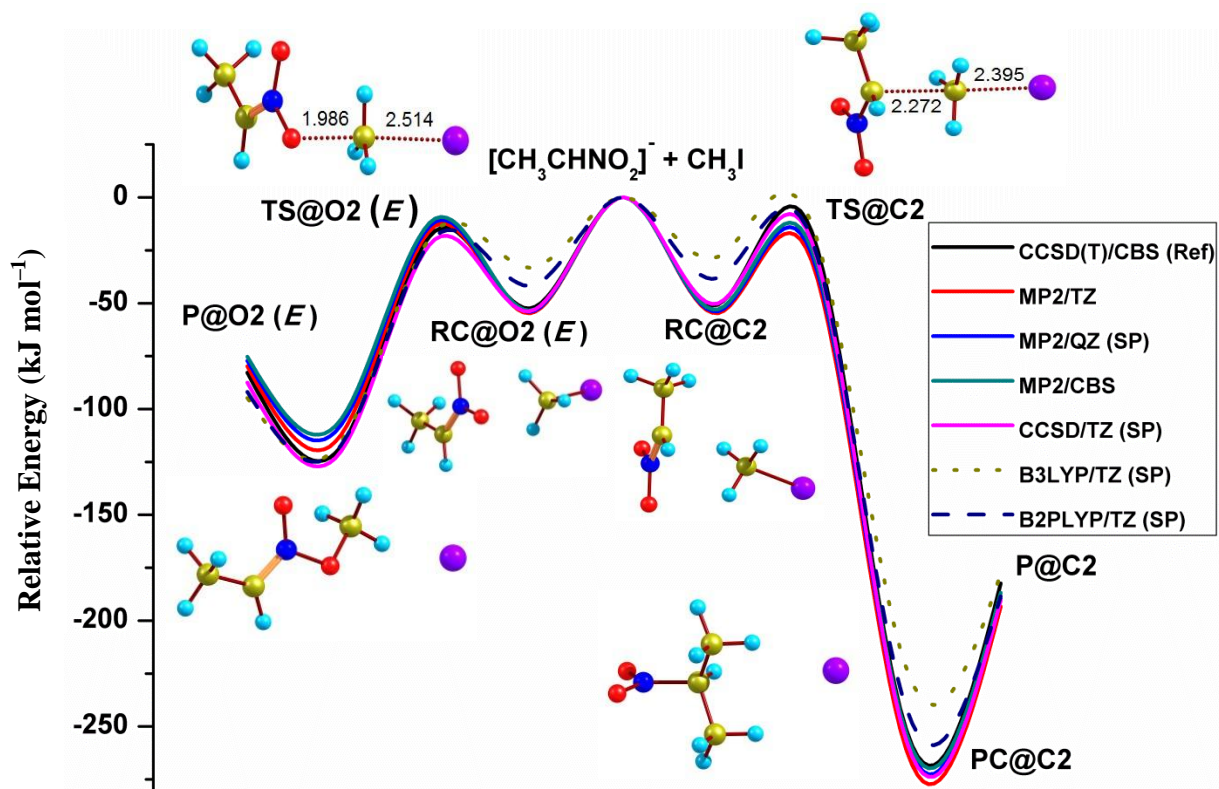
Figure 6.2. Same as Figure 6.1 for the $[CH_3CHNO_2]^-$ (**2**) + CH_3I reaction. The pathway yielding the *Z* stereoisomer, $S_N2@O2$ (*Z*), in O-methylation was omitted for clarity.
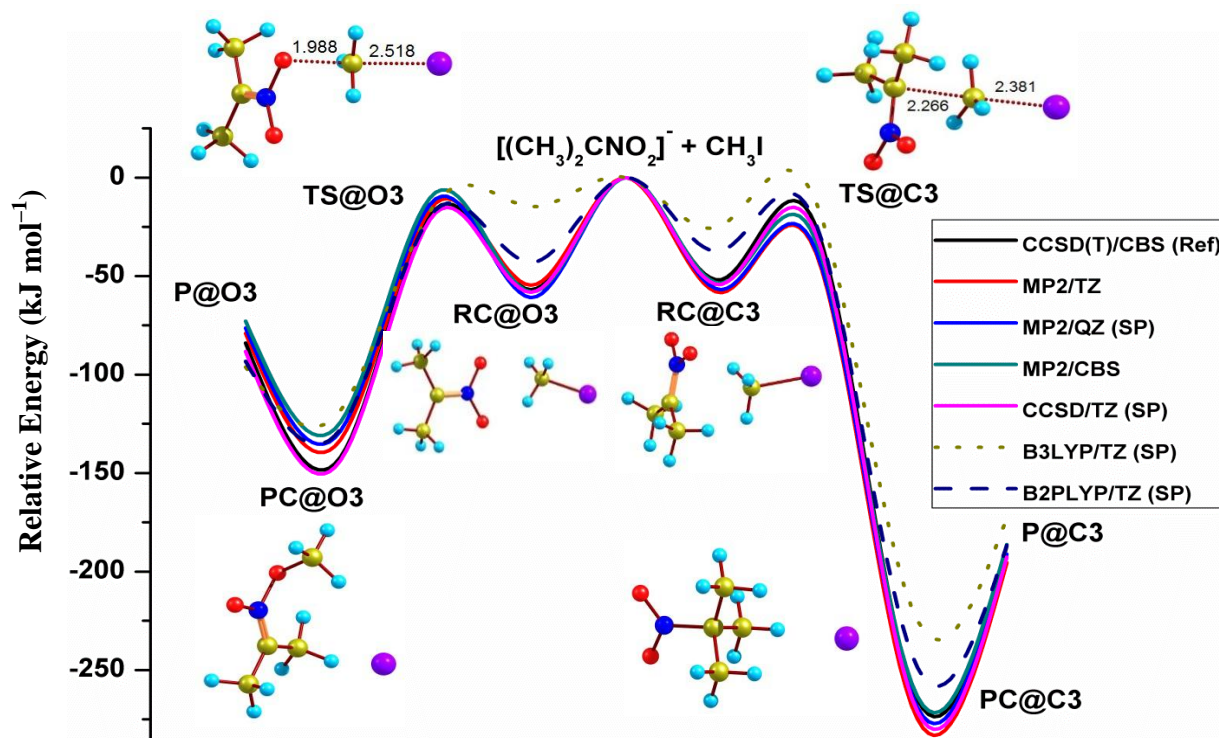
Figure 6.3. Same as Figure 6.1 for the $[(CH_3)_2CNO_2]^-$ (**3**) + CH_3I reaction.
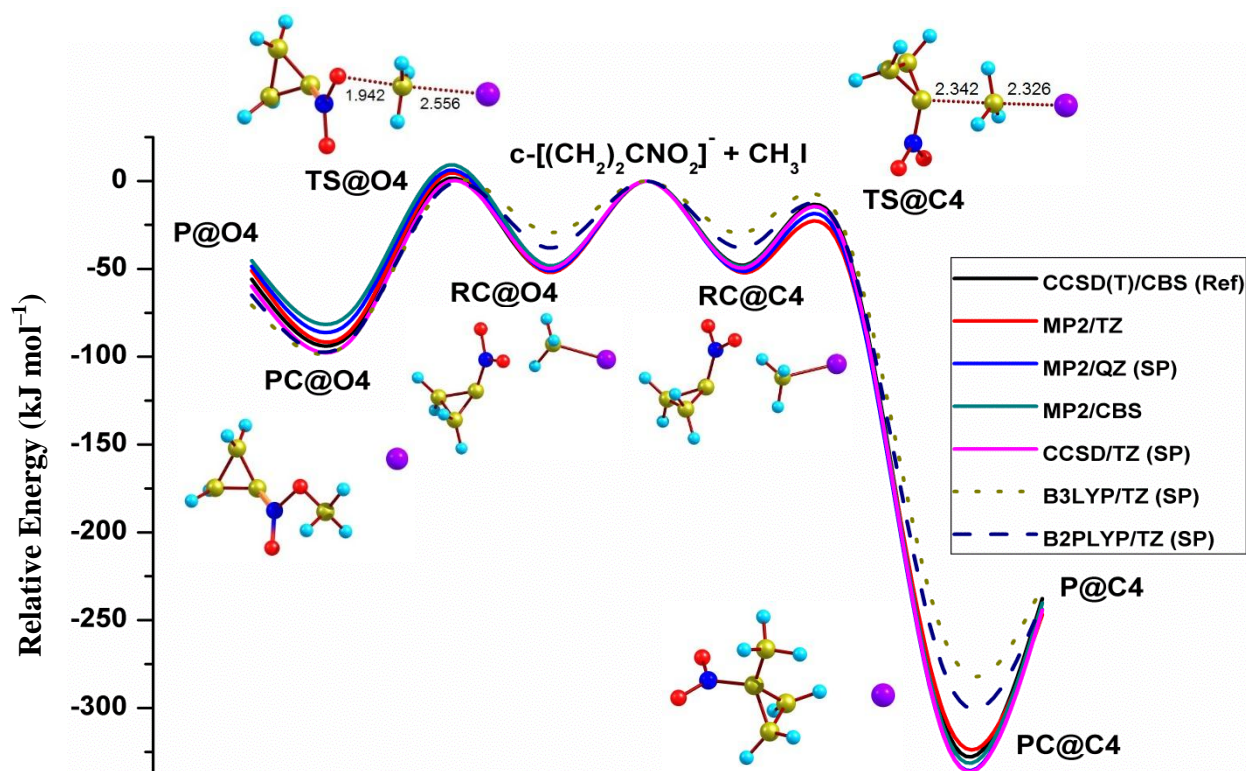
Figure 6.4. Same as Figure 6.1 for the $[c\text{-}(CH_2)_2CNO_2]^-$ (**4**) + CH_3I reaction.

We observed that the activation energies of the reaction pathway through the carbon atom decrease more strongly than the O-methylation with the increase of the basis set size. This behavior is probably due to the $S_N2@C$ reactions (C-methylation) involve a change of hybridization from sp^2 to sp^3 at the carbon atom, which requires larger structural and electronic rearrangements and should be more susceptible to the quality of the basis set employed, for instance, aug-cc-pVDZ-PP versus LANL2DZdp basis sets. In contrast, the $S_N2@O$ pathways do not involve such large changes and hence both basis sets gives almost the same $\Delta^{\ddagger}E$ values.

6.3.2 Structural assessment

Because the C-and O-methylation pathways involve very distinct structural (and electronic) rearrangements and the reactant complexes are intermolecular ion-dipole species the structural assessment of the transition states (TSs) and reactant complexes (RCs) becomes necessary to ascertain the proper description of the kinetics and regioselectivity. This structural assessment was performed by comparing the rotational constants (*A*, *B*, *C*) of the TSs and RCs calculated with different basis sets and taking the MP2/TZ values as references.

The rotational constants are sensitive criteria for comparing structures obtained by different methods, while keeping the compactness of the analysis. The mean relative errors, MRE (%), in the rotational constants of RCs and TSs are depicted in Figures 6.5 and 6.6, respectively.

For the RCs, MP2 method and M06-2X functional performed very well, where the MP2/DZ method provides the lowest 0.9% MRE, while the B3LYP/DZ approach showed the worst MRE (12.95%). Noteworthy that most methods systematically underestimate the rotational constant A and overestimate the values of B and C. These errors in the three rotational constants arise from the different relative orientations of iodomethane (CH_3I) towards the nucleophile, $[R^1R^2CNO_2]^-$, in the RCs, $[R^1R^2CNO_2 \cdots CH_3I]^-$, calculated by the DFT methods, because these RCs are ion-dipole bounded species. For instance, in RC@C1 the iodomethane migrates to change its orientation towards the oxygens during the geometry optimization with the B3LYP/DZ method.
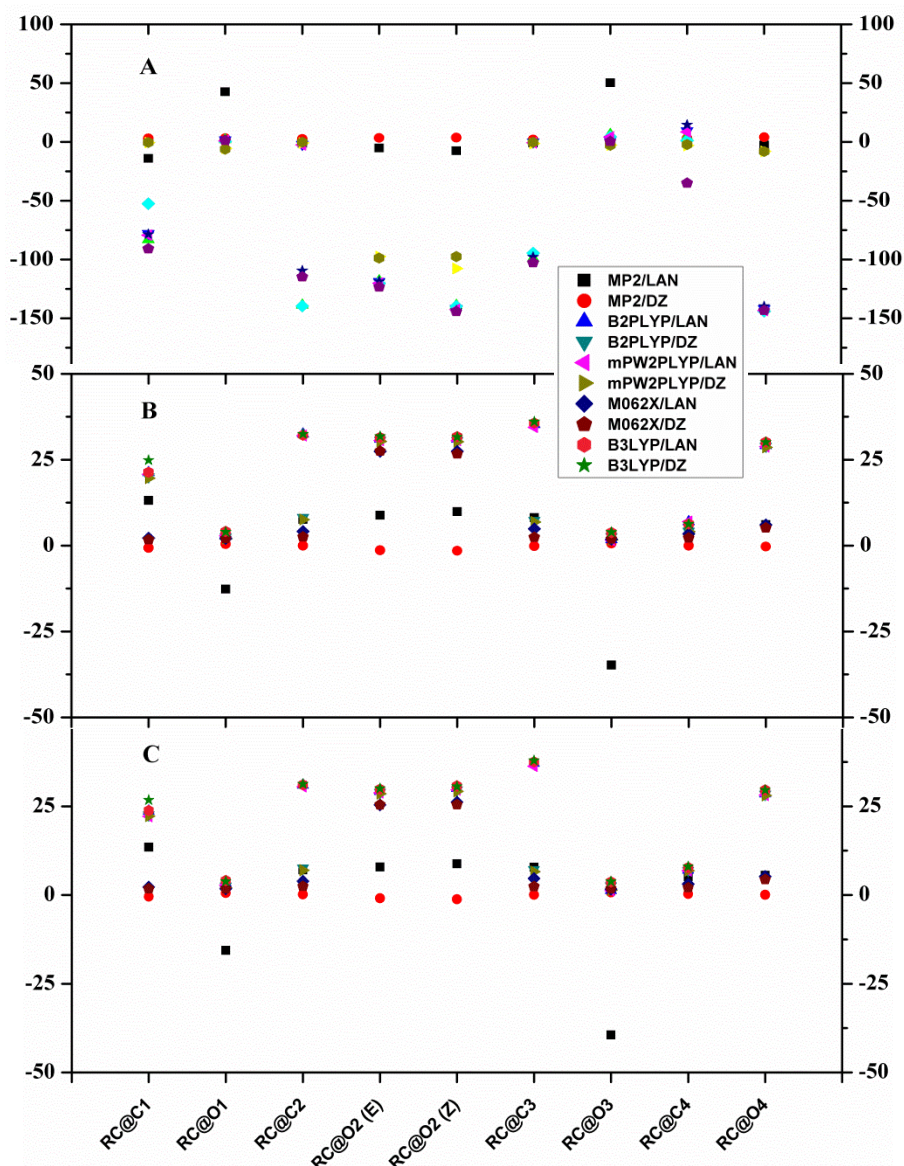
Figure 6.5. Relative error (%) deviations for the rotational constants of the reactant complexes (RCs) computed at the MP2/LAN (black squares), MP2/DZ (red circles), B2PLYP/LAN (blue triangles), B2PLYP/DZ (cadet blue triangles), mPW2PLYP/LAN (pink triangles), mPW2PLYP/DZ (olive triangles), M06-2X/LAN (dark blue squares), M06-2X/DZ (brown pentagons), B3LYP/LAN (red hexagons) and B3LYP/DZ (green stars) levels.
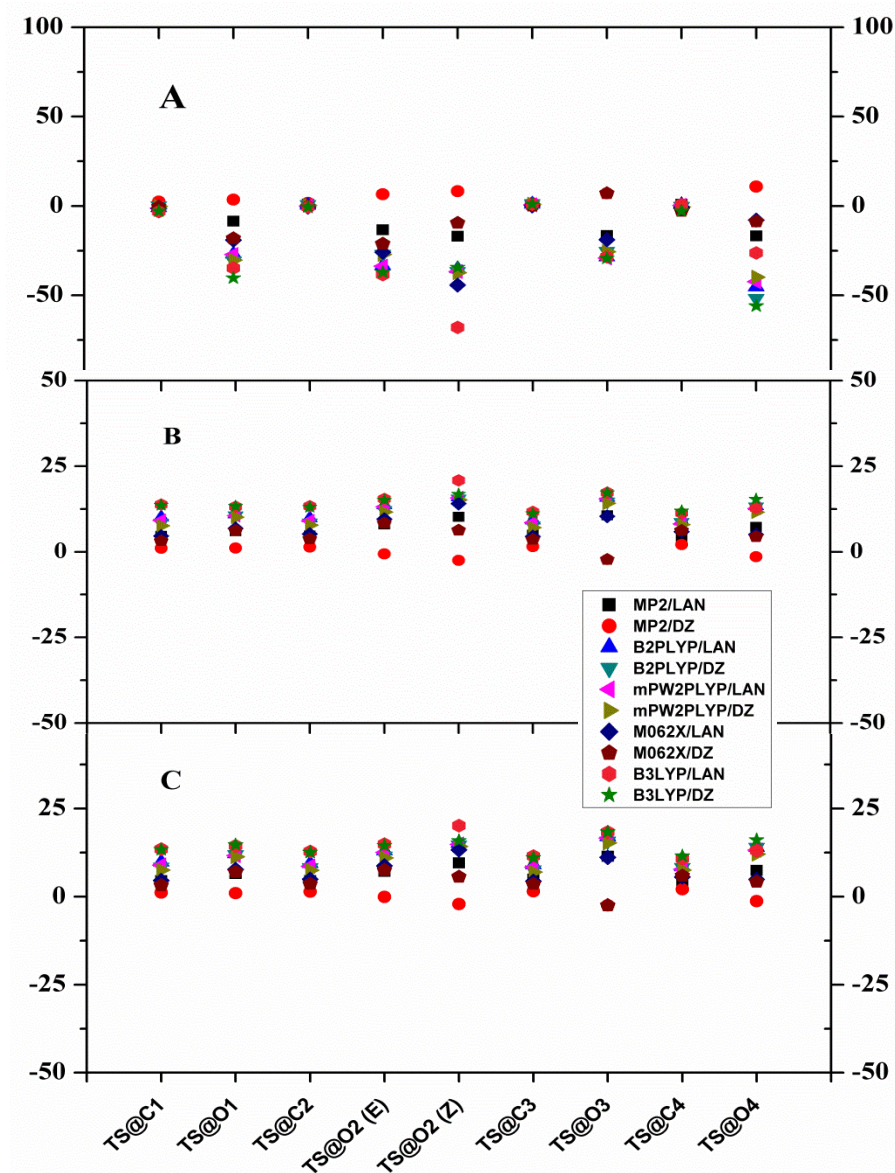
Figure 6.6 Same as Figure 6.5 for the transition states (TSs).

6.3.3 Relative energy assessment

To simplify the analysis, the assessed methods were divided into i) combinations of LAN, DZ and TZ basis sets with DFT functionals and MP2 for which molecular structures were determined (first set), and ii) those combinations for which single-point energy calculations were performed at MP2/TZ structures (second set). Tables 2 and 3 present the mean unsigned error (MUE) and percent mean relative error (% MRE) for energy available ($\Delta_{RC}E$) to the reactant complex, the activation energy barrier ($\Delta^{\ddagger}E$) and the energy of the reaction ($\Delta_{r}E$) for

the first and second sets of assessed methods for all reaction pathways, respectively. In these tables, "Overall" represents the mean values of the errors and "CI (99%)" is the confidence interval for the mean signed errors.

Usually, MUE values smaller than 2-3 kcal mol^{-1} are taken as a reasonable threshold to evaluate the performance of a method [294–297] and we will consider the lower limit (2 kcal mol^{-1}) as the cutoff value for labeling a method as accurate. Therefore, from Table 2, only the MP2/TZ method can be considered accurate, because its overall MUE value (1.20 kcal mol^{-1}) is below this threshold, while all the other combinations provided overall MUE values above it. It is noteworthy that the energy of reaction $\Delta_r E$ is the main source of these large MUE values and if it is not taken into consideration the results obtained with the M06-2X functional would be considered accurate. In fact, this would be relevant for studying the kinetics, because it depends essentially upon the activation energy and the energy available to the reactant complex. Indeed, it can be observed that the MUE's for the energy available to the reactant complexes ($\Delta_{RC} E$) are considered accurate ($<$ 2.0 kcal mol^{-1}) for all methods except B3LYP/LAN. However, taking into consideration the reaction energy, M06-2X/DZ and mPW2PLYP/DZ methods show the worst overall MUE values. Unlike recent benchmarks of DFT functional [233], double-hybrid B2PLYP and mPW2PLYP with medium size basis sets (aug-cc-pVDZ-PP) provided the worst results for activation energies. It can also be observed that the LAN basis sets (6-31+G(d) for C, H, N, O and LANL2DZdp/ECP ECP for I atom) unexpectedly shows overall a better performance than the DZ basis sets (aug-cc-pVDZ-PP), whereas quantitative agreements are obtained only with extended TZ basis sets (aug-cc-pVTZ-PP).

Mean relative errors (MRE %) are useful criteria to determine systematic errors such as under- or overestimations and an accurate method should provide small values of both MUE and MRE. MP/TZ method has a very small overall percent MRE, which combined with the MUE makes this method the most accurate. Whereas M06-2X functional also provides very small overall MRE values, however, these values for separated properties ($\Delta_{RC} E$, $\Delta^{\ddagger} E$, $\Delta_r E$) are relatively large and error cancelations are observed in the overall values. Noteworthy that the M06-2X functional is the most accurate, because the remaining global-hybrid and double-hybrid functionals calculate the activation energies with large MRE (*ca*. 9% to 14%) yielding overall MRE larger than 1.5%. In addition, it is observed that all methods, but MP/TZ, overestimate the energy of the reaction ($\Delta_r E$), which may be an indication of the importance

of more flexible and extended basis sets to describe the thermochemistry of these reactions. In contrast, all methods in Table 6.2 underestimate the activation energy ($\Delta^{\ddagger}E$), suggesting that correlation effects, in addition to the basis sets, are important for providing accurate kinetics properties.

Table 6.2. MUE (kcal mol^{-1}) and MRE (%, in parentheses) in the available energy ($\Delta_{RC}E$) to the reactant complex, in the activation energy ($\Delta^{\ddagger}E$) and in the reaction energy ($\Delta_{r}E$) of all reaction pathways in Scheme 1 for the first set of methods that include optimized structures. The CI (kcal mol^{-1}) for the MSE considering all reaction pathways is also included.

Method	$\Delta_{RC}E$	$\Delta^{\ddagger}E$	$\Delta_{r}E$	Overall	CI (99%)
MP2/LAN	0.40 (-0.05)	1.19 (3.82)	4.70 (-3.77)	2.10 (0.00)	(1.29; 3.41)
MP2/DZ	1.40 (-2.75)	2.12 (7.19)	4.38 (-3.18)	2.63 (0.42)	(1.74; 3.99)
MP2/TZ	0.80 (-1.34)	1.45 (1.61)	1.51 (0.15)	1.25 (0.14)	(0.0; 1.46)
B2PLYP/LAN	1.14 (2.18)	3.40 (9.93)	3.75 (-3.87)	2.76 (2.75)	(3.08; 3.95)
B2PLYP/DZ	1.15 (2.12)	4.79 (14.20)	4.23 (-4.09)	3.39 (4.08)	(4.11; 5.07)
mPW2PLYP/LAN	0.60 (0.88)	3.03 (8.47)	4.42 (-4.47)	2.68 (1.63)	(2.92; 4.07)
mPW2PLYP/DZ	0.94 (1.33)	4.62 (13.52)	4.99 (-4.82)	3.52 (3.34)	(4.30; 5.19)
B3LYP/LAN	2.58 (4.97)	4.25 (12.42)	3.20 (-3.79)	3.34 (4.53)	(4.02; 5.36)
B3LYP/DZ	1.55 (2.93)	3.14 (12.77)	3.22 (-3.91)	2.64 (3.93)	(3.97; 6.25)
M06-2X/LAN	0.45 (0.25)	1.81 (5.34)	5.57 (-5.64)	2.61 (-0.02)	(1.40; 2.91)
M06-2X/DZ	0.59 (-0.45)	3.21 (9.55)	8.07 (-8.18)	3.96 (0.31)	(2.39; 3.55)

Table 6.3 presents the MUE, MRE (%) and the CI for the MSE calculated for all reaction pathways with the second set of methods that assess energy only using the MP2/TZ structures. The MUE and MRE values are improved with respect to the first set (Table 6.2), most likely due to improvements on the basis sets employed. As expected, the CCSD(T)/TZ method presents the lowest overall MUE and MRE values because it is the closest to the reference method, while the global-hybrid M06-2X functional does outperform the double-hybrid functionals and is practically at the 2 kcal mol^{-1} threshold for MUE. This is an assessment quite different from that obtained for the X^{-} + CH$_3$ONO$_2$ (X = OH, F, CH$_2$CN)

reaction pathways [233]. For the available energy to reactant complex, all methods with the extended TZ basis sets provided accurate results (MUE < 2 kcal mol^{-1}) except the all the double-hybrid B2PLYP and B2GPPLYP and the global-hybrid B3LYP functionals. The performance of all methods degrades for the activation energy and the energy of reaction, especially the M06-2X accuracy for $\Delta_r E$ values that strongly affects the overall MUE. Still, the M06-2X remains the most accurate within the DFT functionals, while with MP2/TZ method is the least computational demanding that can be considered accurate.

A systematic trend can be observed for the calculated MRE(%) values where all DFT functionals underestimate $\Delta_{RC} E$ and $\Delta^{\ddagger} E$, except B2GPPLYP for $\Delta_{RC} E$, while they all overestimate $\Delta_r E$. Again, M06-2X presents the lowest MRE amongst the DFT functional, except for B2GPPLYP that despite having large absolute values of MRE provided the lowest overall value due to error cancelations. Still, the MP2/TZ method is the most reliable of the least demanding wavefunction-based methods.

Table 6.3. MUE (kcal mol^{-1}) and MRE (%, in parentheses) in energy available ($\Delta_{RC} E$) to the reactant complex, the activation energy barrier ($\Delta^{\ddagger} E$) and the energy of the reaction ($\Delta_r E$) of the four reactions for the second set of tested functional. The CI (kcal mol^{-1}) for the MSE considering all reaction pathways is also included.

Method (SP)	$\Delta_{RC} E$	$\Delta^{\ddagger} E$	$\Delta_r E$	Overall	CI (99%)
MP2/DZ	1.27 (-2.49)	2.28 (7.66)	5.26 (-4.10)	2.94 (0.36)	(2.07; 4.47)
MP2/TZ	0.68 (-1.03)	1.28 (3.67)	1.51 (0.15)	1.16 (0.93)	(0.06; 1.42)
MP2/QZ	0.57 (-0.68)	1.23 (3.65)	1.49 (0.82)	1.10 (1.26)	(-0.33; 1.01)
MP2/CBS(D,T)	0.57 (-0.60)	1.40 (4.00)	1.41 (1.76)	1.13 (1.72)	(-0.83; 0.75)
MP2/CBS(T,Q)	0.51 (-0.04)	1.17 (3.28)	1.46 (1.43)	1.05 (1.56)	(-0.69; 0.71)
B2PLYP/TZ	2.65 (5.12)	3.14 (9.47)	1.61 (-1.86)	2.47 (4.24)	(2.11; 3.15)
mPW2PLYP/TZ	2.00 (3.88)	2.79 (8.29)	2.33 (-2.54)	2.37 (3.21)	(2.29; 2.98)
B2GPPLYP/TZ	2.13 (-4.09)	2.58 (8.25)	4.51 (-4.06)	3.07 (0.03)	(2.48; 3.94)
B3LYP/TZ	4.65 (9.00)	4.12 (12.29)	2.31 (-1.92)	3.69 (6.46)	(3.45; 4.67)
M06-2X/TZ	0.78 (1.50)	1.39 (3.65)	3.94 (-4.47)	2.04 (0.23)	(0.50; 1.97)
CCSD(T)/DZ	1.16 (-2.25)	2.50 (7.26)	4.78 (-4.18)	2.81 (0.28)	(2.56; 3.96)
CCSD(T)/TZ	0.32 (-0.27)	0.68 (1.82)	1.31 (-1.18)	0.77 (0.12)	(0.68; 1.10)

To ascertain the robustness as well as to corroborate the accuracy provided by the MUE and MRE descriptors, the BW parameters were employed [256] and the results are depicted in Figure 6.7. The analysis of BW descriptors shows that the MP2/TZ method is robust, in addition to being accurate. While, most hybrid-DFT functionals show more number of "worst" than "best" results, except M06-2X and mPW2PLYP functionals with LAN basis sets. Thus, the BW criterion suggests that the hybrid-DFT functionals assessed are not robust for the reactions under study. However, the results regarding the robustness of M06-2X/LAN and mPW2PLYP/LAN methods are not consistent with their corresponding MUE and MRE values, which suggest that the BW is a rough criterion and should be supplemented with other statistical parameters.
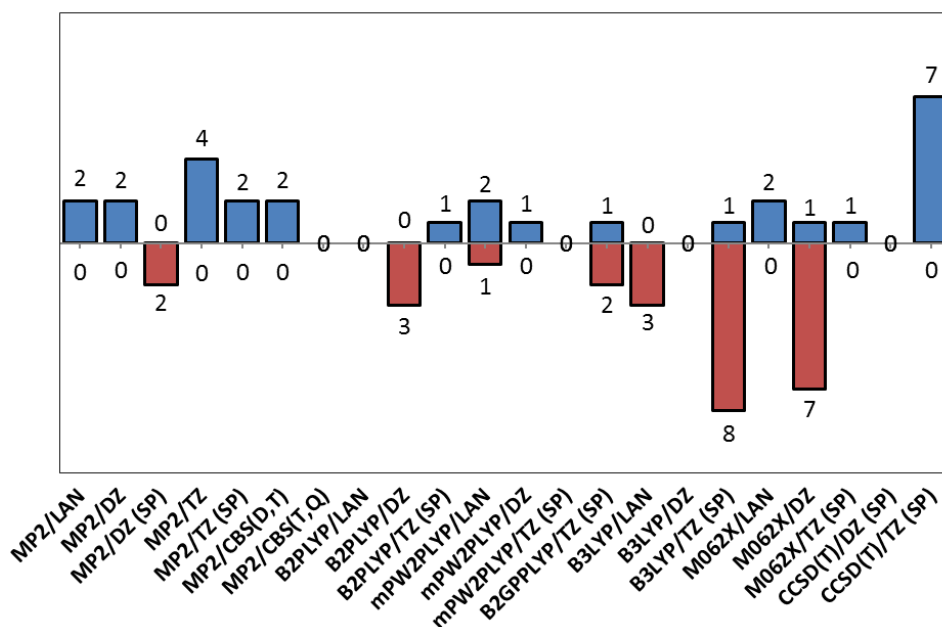
Figure 6.7. BW values obtained from the unsigned errors (see text for details) for all methods. The upper (lower) bars represent the number of times that the method is considered the best (the worst).

Indeed, the CI for the MSE is an additional statistical criterion that should provide a proper evaluation of the robustness combined with the accuracy provided by the MUE results. The ± 2 kcal mol^{-1} limits for CI were chosen to be consistent with the cutoff value employed for the MUE values. For the first set of tested methods (Table 6.2), MP2/TZ is the only method

that yields MUE value below the threshold and CI values within the chosen limits, while all the other methods provided CI values outside the limits. These results show the importance of the basis sets when obtaining structures and energetics of a reaction profile. The MP2/LAN method has overall MUE (2.10 kcal mol^{-1}) and MRE (0.0%) values that can be considered as a very good method, however, it lacks robustness because it has one of the CI values larger than the limit.

For the second set of tested methods (Table 6.3), the CI analysis shows that wavefunction-based methods are the most accurate and robust, except when employed with DZ basis sets, with emphasis in the MP2/TZ method for being then the least expensive. Within the hybrid-DFT functionals, the M06-2X/TZ method can be considered accurate (overall MUE *ca*. 2.0 kcal mol^{-1} and MRE = 0.23%) as well as robust because it has CI values (0.50; 1.97) within the chosen limits.

On the other hand, the range of the CI, given by the difference between the CI values, and its closeness to zero can also be used as an additional criterion to refine the CI results in comparison to the other statistical parameters. Thus, from Tables 6.2 and 6.3 it can be observed that the CCSD(T)/TZ method is the most accurate (lowest overall MUE values) and robust, because of its CI values (0.68; 1.10) have the same sign and provide a very small CI size (0.42 kcal mol^{-1}). Therefore, it can be stated that the CCSD(T)/TZ method is the only methods that predicts 99% of the values within 0.5 kcal mol^{-1} from the reference. The MP2/TZ method also has CI values with the same sign, however, its CI size is slightly larger (1.32 kcal mol^{-1}), so it predicts 99% of the values within 1.5 kcal mol^{-1} from the reference. This same analysis applies to the M06-2X/TZ method, which presents slightly larger CI values (0.50; 1.97). The remaining DFT based methods cannot be considered neither accurate nor robust.

In a more technical note, we noticed that the results obtained with CBS(D,T) and CBS(T,Q) extrapolation schemes at the MP2 level provided essentially the results, which should validate the CCSD(T)/CBS results extrapolated with the CBS(D,T) scheme.

Conclusion

Combined statistical quantities such as mean signed error (MSE), mean unsigned error (MUE), percent mean relative error (MRE%), BW criterion and confidence interval (CI) for MSE were employed to assess the accuracy and robustness of wavefunction (MP2 and CCSD(T)) and hybrid-DFT (B2PLYP, mPW2PLYP, B2GPPLYP, B3LYP, M06-2X) based methods with different basis sets (LANL2DZdp and aug-cc-pVXZ-PP, X = D, T, Q). Structural and relative energy assessments of all reaction pathways (C- and O-methylation) involved in the gas-phase $[R^1R^2CNO_2]^-$ + CH_3I reactions ($R^1 = R^2 = H$, $R^1 = H$ and $R^2 = CH_3$, $R^1 = R^2 = CH_3$, $R^1 + R^2 = c\text{-}(CH_2)_2$) were performed. The rotational constants were used in the structural assessment, whereas the accuracy and robustness in the relative energies were ascertain by the activation energy ($\Delta^{\ddagger}E$), the available energy to the reactant complexes ($\Delta_{RC}E$) and the energy of reaction ($\Delta_{r}E$). The DFT based methods provided structures for the reactant complexes systematically larger than the reference method because these are ion-dipole loosely bounded species. The calculated structures of the transition states show the same trend. Regarding the relative energies of the reaction profiles, MP2/TZ was the most accurate and robust method with the least computational demand within the wavefunction based methods. Whereas the M06-2X/TZ method is most accurate and robust approach within the global- and double-hybrid DFT functionals tested, and it practically reached the threshold of 2 kcal mol^{-1} for MUE and CI limits. For kinetics ($\Delta_{RC}E$ and $\Delta^{\ddagger}E$) this method reaches chemical accuracy (MUE < 1.4 kcal mol^{-1}) and could thus be used for dynamics simulations, however, for organocatalyst designs it may need validation to describe intermolecular interactions. These results should be contrasted with the better performance of the double-hybrid DFT functionals observed for the gas-phase X^- + CH_3ONO_2 (X = OH, F, CH_2CN) reaction pathways.

Chapter 6

Conclusions and Perspectives

Conclusions

The reaction mechanisms, selectivity and regioselectivity of methylation of nitronates $[R^1R^2CNO_2]^-$ by CH_3I in the gas-phase, where $R^1 = R^2 = H$ (**1**), $R^1 = CH_3$ and $R^2 = H$ (**2**), $R^1 = R^2 = CH_3$ (**3**); and $R^1 + R^2 = c\text{-}(CH_2)_2$ (**4**), were investigated by high-level *ab initio* MP2/CBS method combined with ADO and RRKM theories and kinetics simulations. The reaction through the carbon (C-methylation) is preferred over the reaction through the oxygen atoms (O-methylation) in these series of reactions. The regioselectivity towards the C-alkylation is explained by the much larger exothermicity of this reaction channel compared to the O-alkylation. The trend of the total rate constant for the four reactions (**4** $\gg$ **3** > **2** > **1**) was found to be in excellent agreement with the experimental trend. The increase of reactivity upon the increase of crowdedness of the central carbon atom is explained by differences of sp^3 character at this atom and the decrease of the vibrational frequency associated with pyramidalization around this carbon atom. Despite the quasi-quantitative agreement, dynamics effects may be still important to provide quantitative values of the rate constants in the gas-phase.

In order to ascertain the reliability of the used methods for similar molecular modeling, an assessment of hybrid-DFT functionals and MP2 method for these reactions was performed using the statistical quantities such as the mean signed error (MSE), the mean unsigned error (MUE), the percent mean relative error (% MRE), best and worse (BW), and the confidence interval (CI) against the CCSD(T)/CBS//MP2/aug-cc-pVTZ reference method. The available energies to the reactant complexes were described quite well by all methods; however, only the MP2/aug-cc-pVTZ-PP method provided values within 2 kcal/mol (8.4 kJ/mol) from the reference method for activation energies and reaction energies. Amongst the DFT methods, the global-hybrid M06-2X functional produced the best overall results including BW and CI. Thus, unlike previous assessments of DFT functionals for describing S_N2 reactions, the double-hybrid functionals were outperformed by the global-hybrid M06-2X functional for energy and structures involved in

these methylation reactions of nitronates. Whereas the MP2/aug-cc-pVTZ was the most accurate and nearly provided results with chemical accuracy.

Because the applications of these alkylation reactions in synthesis are performed in solution with several distinct alkylating agents, we have also investigated the methylation reactions of [MeCHNO$_2$]$^-$ (**2**) by Me$_3$O$^+$ (oxonium) and of arylnitronates [XC$_6$H$_4$CHNO$_2$]$^-$ (X = H, *p*-MeO, *p*-NO$_2$) by MeCl in the gas-phase and in solution. The results show regioselectivity towards O-methylation in the gas-phase and more significantly in solution (dichloromethane), which is in line with the experimental observation. The calculated trend of the reactivity with the substituent in the arylnitronates [XC$_6$H$_4$CHNO$_2$]$^-$ is also in agreement with the experimental rate constants in DMF. These overall results suggest that the regioselectivity can be controlled by the alkylating agent (MeOBS, MeI, Me$_3$O$^+$) and by the solvent (polarity, protic/aprotic), however, the results are dependent upon the quantum method and possibly on the solvent model employed.

Most of the original hypotheses regarding the reactivity and selectivity in the gas-phase were supported by the results and interpretations, which may be useful for designing new reaction media, catalysts, and chiral auxiliary as well as to aid regio- and stereo-selectivity characterization.

Perspectives

1)   [XC$_6$H$_4$CHNO$_2$]$^-$ (X = H, *p*-MeO, *p*-NO$_2$) + MeOBS.

Calculations using MeCl as alkylating agent for the [XC$_6$H$_4$CHNO$_2$]$^-$ (X = H, *p*-MeO, *p*-NO$_2$) in solution phase provide results slightly favoring the O-methylation; whereas the experiments shows strong preference of O-methylation pathway. However, since the methylating reagent MeOBS (methyl *p*-bromobenzenesulfonate) was used in the experiments, which is much more reactive than MeCl, calculations using MeOBS make one of the perspective of the study.

2)   Design of organocatalysts, axillary chiral agents and blocking species to the nitro group.

The very distinct hydrogen-bonding properties of the –CH and –NO$_2$ groups in [R^{1}R^{2}CNO$_2$]$^-$ nitronates can be explored to design blocking species for either site. For instance, hydrogen-bonding donors such as ethylene glycol HOCH$_2$CH$_2$OH may interact strongly with the –NO$_2$ group blocking it towards O-alkylations. Thus, the regioselectivity towards the formation of C–C bond (C-alkylation) could be favored and chiral products [R^{1}R^{2}CR^{3}NO$_2$] may be formed with the proper alkylating agent. If the blocking species is chiral, it could act as a chiral auxiliary and induces enantiomeric excess leading to enantiomeric selective alkylations. In addition, this chiral blocking species could also be designed to act as catalysts by selectively stabilizing the transition state of the C-alkylation pathway relative to the reactants.

3)   Solvent effects on [R^{1}R^{2}CHNO$_2$]$^-$(solv) + CH$_3$I(solv)

The C- and O-alkylation pathways were dependent upon the solvent, which may be controlled by its polarity and ability to form hydrogen bond. Thus, for non-specific interaction solvent, the effects of the polarity could be investigated and explored promptly with PCM (polarizable continuum model) methods. For solvent that forms hydrogen bonds a discrete-continuum solvent model could be used in detailed investigations. Comparisons with the reaction pathways in the gas-phase could provide information about intrinsic reactivity of these species and aid designing of new reaction media.

4)   Testing SRP models

For studying the dynamics of methylation reactions in the gas-phase and in solution, quantitative results require thousands of trajectories, which is very demanding. A viable alternative is to adjust the parameters of semiempirical methods using specific reaction parameterization (SRP) approach taking the reference energies and structures from the high-level *ab initio* methods.

The SRP model will be tested by recalculating the reactants, products, and transition state structures, reaction barriers and reaction energies with the RM1-SRP method, as well as the IRC for each reaction pathways and compare with the M06-2X results used as reference.

If this validation shows the RM1-SRP method to be inadequate, we intend to modify the scoring (response) function by using relative values or weight factors to increase the relevance of the transition states and the reactant complexes. Additional points (structures along the IRC) may be included in the response function and/or additional properties such as the energy gradients (forces) on each atom at selected structures.

Additional validation involves: i) RRKM rate calculations with the reference and SRP methods and ii) comparisons of dynamical trajectories obtained by the reference method (M06-2X) and RM1-SRP method starting at the same initial conditions.

References

[1]   D. K. Bohme, L. B. Young, J. Am. Chem. Soc., 1970, 92, 7354.

[2]   L. B. Young, E. Lee-Ruff, D. K. Bohme, Chem. Commun., 1973, 35.

[3]   D. K. Bohme, G. I. Mackay, J. D. Payzant, J. Am. Chem. Soc., 1974, 96, 4027.

[4]   K. Tanaka, G. I. MacKay, J. D. Payzant, D. K. Bohme, Can. J. Chem., 1976, 54, 1643.

[5]   C. A. Lieder, J. I. Brauman, J. Am. Chem. Soc., 1974, 96, 4028.

[6]   J. I. Brauman, W. N. Olmstead, C. A. Lieder, J. Am. Chem. Soc., 1974, 96, 4030.

[7]   C. A. Lieder, J. I. Brauman, Int. J. Mass Spectrom. Ion. Phys., 1975, 16, 307.

[8]   E. E. Ferguson, F. C. Fehsenfeld, A. L. Schmeltekopf, Adv. At. Mol. Phys., 1969, 5, 1.

[9]   N. G. Adams, D. Smith, J. M. Farrar, W.H. Sanders (Eds.), Techniques for the study of ion molecule reactions, Wiley, New York, 1988, 165.

[10]   M. B. Comisarov, A. G. Marshall, Chem. Phys. Lett., 1974, 25, 282.

[11]   M. B. Comisarov, A. G. Marshall, Chem. Phys. Lett., 1974, 26, 489.

[12]   A. G. Marshall, C. L. Hendrickson, G. S. Jackson, Mass Spectrom. Rev., 1998, 17, 1.

[13]   J. P. Briggs, R. Yamdagni, P. Kebarle, J. Am. Chem. Soc., 1972, 94, 5128.

[14]   P. Kebarle, J. M. Farrar, W. H. Sanders (Eds.), Techniques for the study of ion molecule reactions, Wiley, New York, 1988, 221.

[15]   M. Meot-Ner, L. W. Sieck, J. Am. Chem. Soc., 1991, 113, 4448.

[16]   M. Arshadi, P. Kebarle, J. Phys. Chem., 1970, 74, 1483.

[17]   M. Arshadi, R. Yamdagni, P. Kebarle, J. Phys. Chem., 1970, 74, 1475.

[18]   V. F. DeTuri, P. A. Hintz, K. M. Ervin, J. Phys. Chem. A, 1997, 101, 5969.

[19]   R. C. Dunbar, T. B. McMahon, D. Thoelmann, D. S. Tonner, D. R. Salahub, D. Wei, J. Am. Chem. Soc., 1995, 117, 12819.

[20]   M. Sena, J. M. Riveros, J. Phys. Chem. A, 1997, 101, 4384.

[21]   D. L. King, D. A. Dixon, D. R. Herschbach, J. Am. Chem. Soc., 1974, 96, 3328.

[22]   G. E. Davico, J. Phys. Chem. A, 2006, 110, 13112.

[23]   W.-P. Hu, D. G. Truhlar, J. Am. Chem. Soc., 1994, 116, 7797.

[24]   K. Ohta, K. Morokuma, J. Phys. Chem., 1985, 89, 5845.

[25]   H. Tachikawa, J. Phys. Chem. A, 2001, 105, 1260.

[26]   S. S. Glad, F. Jensen, J. Phys. Chem., 1996, 100, 16892.

[27]   M. C. Lind, S.L. Garrison, J. M. Becnel, J. Phys. Chem., A, 2010, 114, 4641.

[28]   J. H. Sullivan J. Chem. Phys., 1967, 46, 73.

[29]   M. R. Wright, Introduction to chemical kinetics, John Wiley & Sons, Oberlin, OH, 2004.

[30]   J. L. Gleave. E. D. Hughes, C. K. Ingold, J. Chem. Soc., 1935, 236.

[31]   T. W. G. Solomon, Organic Chemistry, 6th ed., Wiley, Cape Girardeau, MO, 1996, p. 233.

[32]   J. Mikosch, S. Trippel, C. Eichhorn, R. Otto, U. Lourderaj, J. X. Zhang, W. L. Hase, M. Weidemüller, R. Wester, Science, 2008, 319, 183.

[33]   C. Drahl, Chem. & Eng. News, 2008, 86, 9.

[34]   J. I. Brauman, Science, 2008, 319, 168.

[35]   M. A. F. Souza, T. C. Correra, J. M. Riveros, R. L. Longo, J. Am. Chem. Soc., 2012, 134, 19004.

[36]   T. Su, M. T. Bowers, Gas Phase Ion Chemistry, Vol. 1, Academic Press, New York, 1979, p. 83.

[37]   T. Su, M. T. Bowers, Inter. J. Mass Spectrom. Ion Phys., 1973, 12, 347.

[38]   P. Valtazanos, K. Ruedenberg, Theor. Chim. Acta, 1986, 69, 281.

[39]   R. M. Minyaev, D. J. Wales, Chem. Phys. Lett., 1994, 218, 413.

[40]   B. Carpenter, Annu. Rev. Phys. Chem., 2005, 56, 57.

[41]   A. E. Litovitz, I. Keresztes, B. K. Carpenter, J. Am. Chem. Soc., 2008, 130, 12085.

[42]   J. D. Rynbrandtand, B. S. Rabinovitch, J. Phys. Chem., 1971, 75, 2164.

[43]   J. F. Meagher, K. J. Chao, J. R. Barker, B. S. Rabinovitch, J. Phys. Chem., 1974, 78, 2535.

[44]   D. J. Mann, W. L. Hase, J. Am. Chem. Soc., 2002, 124, 3208.

[45]   L. Sun, W. L. Hase, K. Song, J. Am. Chem. Soc., 2001, 123, 5753.

[46]   W. L. Hase, Acc. Chem. Res., 1998, 31, 659.

[47]   T. Uzer, Phys. Rep., 1991, 199, 73.

[48]   Z. Shi, R. J. Boyd, J. Am. Chem. Soc., 1990, 112, 6789.

[49]   J. M. Riveros, M. Sena, G. H. Guedes, L. A. Xavier, R. Slepetys, Pure Appl. Chem., 1998, 70, 1969.

[50]   J. M. Gonzales, R. S. Cox III, S. T. Brown, W. D. Allen, H. F. Schaefer III, J. Phys. Chem. A, 2001, 105, 11327.

[51]   L. Sun, K. Song, W. L. Hase, Science, 2002, 296, 875.

[52]   S. J. Blanksby, G. B. Ellison, B. V. Bierbaum, S. Kato, J. Am. Chem. Soc., 2002, 124, 3196.

[53]   E. Breuer, H. G. Aurich, A. Nielsen, in Nitrones, Nitronates and Nitroxides: The Chemistry of Functional Groups, (Eds.: S. Patai, Z. Rappoport), Jonn Wiley & Sons, New York, 1989, Chapter 3.

[54]   O. Noboro, in The Nitro Group in Organic Synthesis, Wiley-VCH, New York, 2001.

[55]   G. Rosini, in Comprehensive Organic Synthesis, Vol. 2, B. M. Trost (Ed.), Pergamon, New York, 1991.

[56]   H. Fever, A. T. Nielsen, in Nitro Compounds, Recent Advances in Synthesis and Chemistry, VCH, Weinheim, 1990.

[57]   S. L. Ioffe, N. D. Zelinsky, in Nitrile Oxides, Nitrones and Nitronates in Organic Synthesis: Novel Strategies in Synthesis, H. Feuer (Ed.), 2nd edition, Chapter 3, Nitronates, 2008, 435.

[58]   L. Kurti, B. Czako, in Strategic Applications of Named Reactions in Organic Synthesis, Elsevier Academic Press, Burlington, MA, 2005.

[59]   S. E. Denmark, J. J. Cottell, in Synthetic Applications of 1,3-Dipolar Cycloaddition Chemistry Toward Heterocycles and Natural Products, Vol. 59, A. Padwa, W. H. Pearson (Eds.), John Wiley & Sons, Inc., New York, Chapter 2 Nitronates, 2002, p 83.

[60]   K. B. G. Torssell, in Nitrile Oxides, Nitrones, and Nitronates in Organic Syntheis, VCH Publishers, New York, 1988.

[61]   B. Lecea, A. Arrieta, I. Morao, F. P. Cossio, Chem. Eur. J., 1997, 3, 20.

[62]   B. R. Linton, M. Scott, A. D. Hamilton, Chem. Eur. J., 2000, 6, 2449.

[63]   T. Sakata, N. Seki, K. Yomogida, H. Yamagishi, A. Otsuki, C. Inoh, H. Yamataka, J. Org. Chem., 2012, 77, 10738.

[64]   J. M. Garver, Y.-r. Fang, N. Eyet, S. M. Villano, V. M. Bierbaum, K. C. Westaway, J. Am. Chem. Soc., 2010, 132, 3808.

[65]   J. Chandrasekhar, S. F. Smith, W. L. Jorgensen, J. Am. Chem. Soc., 1985, 107, 154.

[66]   D. K. Bohme, G. I. Mackay, J. Am. Chem. Soc., 1981, 103, 978.

[67]   D. K. Bohme, A. B. Rakshit, G. L. Mackay, J. Am. Chem. Soc., 1982, 104, 1100.

[68]   J. I. Brauman, L. K. Blair, J. Am. Chem. Soc., 1970, 92, 5986.

[69]   R. W. Taft, Prog. Phys. Org. Chem., 1983, 14, 247.

[70]   W. N. Olmstead, J. I. Brauman, J. Am. Chem. Soc., 1977, 99, 4219.

[71]   S. Kato, K. E. Carrigan, C. H. DePuy, V. M. Bierbaum, Eur. J. Mass Spectrom., 2004, 10, 225

[72]   J. E. Bartmess , J. A. Scott , R. T. McIver Jr. J. Am. Chem. Soc., 1979, 101, 6046.

[73]   D. K. Bohme, G. I. Mackay, J. Am. Chem. Soc., 1981, 103, 978.

[74]   D. K. Bohme, A. B. Rakshit, G. L. Mackay, J. Am. Chem. Soc., 1982, 104, 1100.

[75]   W. N. Olmstead, J. I. Brauman, J. Am. Chem. Soc. 1977, 99, 4219.

[76]   J. I. Brauman, L. K. Blair, J. Am. Chem. Soc. 1970, 92, 5986.

[77]   R. H. Bathgate, E. A. Moelwyn-Hughes, J. Chem. Soc., 1959, 2642.

[78]   C. D. Ritchie, G. A. Chappell, J. Am. Chem. Soc., 1970, 92, 1819.

[79]   A. Dedieu, A. Veillard, Chem. Phys. Lett., 1970, 5, 328; J. Am. Chem. Soc., 1972, 94, 6730.

[80]   H. B. Schlegel, K. Mislow, F. Bernardi, A. Bottoni, Theor. Chim. Acta, 1977, 44, 245.

[81]   S. Wolfe, D. J. Mitchell, H. B. Schlegel, J. Am. Chem. Soc., 1981, 103, 7692.

[82]   S. S. Shaik, H. B. Schlegel, S. Wolfe, Chem. Commun., 1988, 1322.

[83]   J. Chandrasekhar , S. F. Smith , W. L. Jorgensen, J. Am. Chem. Soc., 1985, 107, 154.

[84]   C. H. DePuy, J. Org. Chem. 2002, 67, 2393.

[85]   J. Chandrasekhar, S. F. Smith, W. L. Jorgensen, J. Am. Chem. Soc., 1984, 106, 3049.

[86]   C. J. Cramer, D. G. Truhlar, Chem. Rev., 1999, 99, 2161.

[87]   R. A. Morris, A. A. Viggiano, T. M. Miller, J. V. Seeley, S. T. Arnold, J. F. Paulson, J. M. Van Doren, J. Phys. Chem., 1996, 100, 10641.

[88]   P. O. Staneke, G. Groothuis, S. Ingemann, N. M. M. Nibbering, J. Phys. Org. Chem., 1996, 9, 471.

[89]   G. N. Sastry, S. Shaik, J. Am. Chem. Soc., 1998, 120, 2131.1111

[90]   B. Sirjean, R. Fournet, Phys. Chem. Chem. Phys., 2013, 15, 596.

[91]   A. K. Paul, S. Kolakkandy, S. Pratihar, W. L. Hase, in Reaction Rate Constant Computations: Theories and Applications, Royal Society of Chemistry 2013, p 494.

[92]   M. H. Almatarneh, M. Altarawneh, R. A. Poirier, I. A. Saraireh, J. Comput. Sci., 2014, 5, 568.

[93]   H. Wang, L. Zhu, W. L. Hase, J. Phys. Chem., 1994, 98, 1608.

[94]   H. Wang, W. L. Hase, J. Am. Chem. Soc., 1995, 117, 9347.

[95]   W. L. Hase, Y. J. Cho, J. Chem. Phys., 1993, 98, 8626.

[96]   W. L. Hase, Science, 1994, 266, 998.

[97]   J. K. Laerdahl, E. Uggerud, Int. J. Mass Spectrom., 2002, 214, 277.

[98]   H. Wang, G. H. Peslherbe, W. L. Hase, J. Am. Chem. Soc., 1994, 116, 9644.

[99]   G. H. Peslherbe, H. Wang, W. L. Hase, J. Am. Chem. Soc., 1996, 118, 2257.

[100]   H. Wang, W. L. Hase, Chem. Phys., 1996, 212, 247.

[101]   H. Wang, W. L. Hase, J. Am. Chem. Soc., 1997, 119, 3093.

[102]   H. Wang, W. L. Hase, Int. J. Mass Spectrom., 1997, 167/168, 573.

[103]   H. Wang, E. M. Goldfield, W. L. Hase, J. Chem. Soc., Faraday Trans., 1997, 93, 737.

[104]   D. J. Mann, W. J. Hase, J. Phys. Chem. A, 1998, 102, 6208.

[105]   T. Su, H. Wang, W. L. Hase, J. Phys. Chem. A, 1998, 102, 9819.

[106]   W. L. Hase, H. Wang, G. H. Peslherbe, N. G. Adams, L. M. Babock (Eds.), Advances in Gas-Phase Ion Chemistry, Vol.3, JAI Press, Greenwich, CT, 1998, 125.

[107]   G. Li, W. L. Hase, J. Am. Chem. Soc., 1999, 121, 7124.

[108]   S. R. Vande Linde, W. L. Hase, J. Phys. Chem., 1990, 94, 6148.

[109]   D. G. Truhlar, A. D Isaacson, R.T Skodje, B.C. Garrett, Phys. Chem., 1982, 86, 2252.

[110]   D. G. Truhlar, and B.C. Garrett, Acc. Chem. Res., 1980, 13, 440.

[111]   D. G. Truhlar, and A. Kuppermann, J. Am. Chem. Soc., 1971, 93, 1840.

[112]   S.N. Rai, and D.G. Truhlar, J. Chem. Phys., 1983, 79, 6046.

[113]   D. G. Truhlar, J. Comput. Chem., 1991, 12, 266.

[114]   B. C. Garrett, and D. G. Truhlar, J. Phys. Chem., 1980, 84, 805.

[115]   D. G. Truhlar, B. C. Garrett, S. J. Klippenstein, J. Phys. Chem., 1996, 100, 12771.

[116]   K. Laidler, C. King, J. Phys. Chem., 1983, 87, 2657.

[117]   K. Laidler, C. King, Chem. Intell., 1998, 4, 39.

[118]   IUPAC, Compendium of Chemical Terminology, 2nd ed. (the "Gold Book"), 1997. Online corrected version: transition state theory, 2006.

[119] L. Arnaut, S. Formosinho, H. Burrows, Chemical Kinetics; From Molecular Structure to Chemical Reactivity, Coimbra, 2007.

[120] S. K. Upadhyay, Chemical kinetics and reaction dynamics, Springer, New York, 2007.

[121] P. L. Houston, Chemical kinetics and reaction dynamics, Dover, New York, 2012.

[122] C. J. Cramer, Essential of computational chemistry: theory and model, 2nd ed., John Wiley & Sons, Chichester, 2004.

[123] Keith J. Laidler, Chemical Kinetics, 3rd ed., Harper & Row, New York, 2004.

[124] D. A. McQuarrie, J. D. Simon, Physical chemistry: A molecular approach, University Science Books, Sausalito, CA, 1997.

[125] D. G. Truhlar, A. Kuppermann, J. Am. Chem. Soc., 1971, 93, 1840.

[126] B. C. Garrett, D. G. Truhlar, R. S. Grev, A. W. Magnuson, J. Phys. Chem., 1980, 84, 1730.

[127] P. R. Schreiner, H. P. Reisenauer, D. Ley, D. Gerbig, C.-H. Wu, W. D. Allen, Science, 2011, 332, 1300.

[128] D. G. Truhlar, B. C. Garrett, Acc. Chem. Res., 1980, 13, 440.

[129] D. G. Truhlar, B. C. Garrett, Annu. Rev. Phys. Chem., 1984, 35, 159.

[130] D. G. Truhlar, B. C. Garrett, S. J. Klippenstein, J. Phys. Chem., 1996, 100, 12771.

[131] A. Fernandez-Ramos, J. A. Miller, S. J. Klippenstein, D. G. Truhlar, Chem. Rev., 2006, 106, 4518.

[132] W. L. Hase, in Unimolecular reaction dynamics theory and experiments, T. Baer, W. L. Hase (Eds.), Oxford University Press, New York, 1996.

[133] J. W. Moore, R. G. Pearson, Kinetics and Mechanism, John Wiley & Sons, New York, 1988.

[134] O. K. Rice, H.C. Ramsperger, J. Am. Chem. Soc., 1927, 49, 1617.

[135] O. K. Rice, H. C. Ramsperger, J. Am. Chem. Soc., 1927, 50 , 617.

[136] L. S. Kassel, J. Phys. Chem., 1928, 32, 225.

[137] L. S. Kassel, J. Phys. Chem., 1928, 32, 1065.

[138] N. E. Henriksen, F. Y. Hansen, in Theories of molecular reaction dynamics: The microscopic foundation of chemical kinetics, Oxford University Press Inc., New York, 2008.

[139] R. A. Marcus, J. Chem. Phys., 1952, 20, 364.

[140] G. M. Wieder, R. A. Marcus, J. Chem. Phys., 1962, 37, 1835.

[141] K. A. Holbrook, M. J. Pilling, S. H. Robertson, Unimolecular reactions, 2nd ed., John Wiley & Sons, New York, 1996.

[142] T. Uzer, J. T. Hynes, W. P. Reinhardt, J. Chem. Phys., 1986, 85, 5791.

[143] R. Schinke, Photodissociation dynamics, Cambridge University Press, Cambridge, 1993.

[144] N. E. Henriksen, Adv. Chem. Phys., 1995, 91, 433.

[145] E. R. Lovejoy, S. K. Kim, C. B. Moore, Science, 1992, 256, 1541.

[146] S. K. Kim, E. R. Lovejoy, C. B. Moore, J. Chem. Phys., 1995, 102, 3202.

[147] A. H. Zewail, Femtochemistry, Vols 1, 2, World Scientific, Singapore, 1994.

[148] P. Langevin, Ann. Chim. Phys., 1905, 5, 245.

[149] G. Giomousis, D. P. Stevenson, J. Chem. Phys., 29, 1958, 294.

[150] W. J. Chesnavich, T. Su, M. T. Bowers, J. Chem. Phys., 1980, 72, 2641.

[151] T. Su, J. Chem. Phys., 1985, 82, 2164.

[152] T. Su, J. Chem. Phys., 1994, 100, 4703.

[153] T. Su, M. T. Bowers, J. Chem. Phys., 1973, 58, 3027.

[154] T. Su, M. T. Bowers, J. Am. Chem. Soc., 1973, 95, 1370.

[155] M. T. Bowers, T. Su, V. G. Amcich, J. Chem. Phys., 1973, 58, 5175.

[156] L. Bass, T. Su, W. J. Chesnavich, M. T. Bowers, Chem. Phys. Lett., 1975, 34, 119.

[157] M. T. Bowers and T. Su, in Interactions between ions and molecules, P. Ausloos (Ed.), Plenum, New York, 1975, 163.

[158] R. S. Hemsworth. J. D. Payzant, H. I. Schiff, D. K. Bohme, Chem. Phys. Lett., 1974, 26, 417.

[159] D. K. Bohme, in Interactions between ions and molecules, P. Ausloos (Ed.), Plenum, New York, 1975, 489.

[160] G. I. Mackay, L. D. Betowski, J. D. Payzant, H. I. Schiff, and D. K. Bohme, J. Phys. Chem., 1976, 80, 2919.

[161] T. Su and M. T. Bowers, J. Chem. Phys., 1974, 60, 4897.

[162] T. Su and M. T. Bowers, J. Am. Chem. Soc., 1973, 95, 7609.

[163] T. Su, E. C. F. Su, and M. T. Bowers; J. Chem. Phys., 1978, 69, 2243.

[164] T. Helgaker, J. Olsen, P. Jorgensen, Molecular electronic-structure theory, John Wiley & Sons, New York, 2013.

[165] M. J. S. Dewar, E. G. Zoebisch, E. F. Healy and J. J. P. Stewart, J. Am. Chem. Soc., 1985, 107, 3908.

[166] J. J. P. Stewart, J. Comput. Chem., 1989, 10, 209.

[167] M. J. S. Dewar and W. J. Thiel, J. Am. Chem. Soc., 1977, 99, 4899.

[168] P. Atkins, R. Friedman, Molecular quantum mechanics, Oxford University Press, Oxford, 2005.

[169] P. Atkins, J. Paula, R. Friedman, Quanta, matter, and change: A molecular approach to physical chemistry, W. H. Freeman and Company, New York, 2009.

[170] C. Møller and M. S. Plesset, Phys. Rev., 1934, 46, 618.

[171] J. Cizek, J. Chem. Phys., 1966, 45, 4256.

[172] M. Head-Gordon, J. A. Pople, J. M. Frisch, Chem. Phys. Lett., 1988, 153, 503.

[173] J. A. Pople, R. Seeger, R. Krishnan, Int. J. Quant. Chem., 1977, 12, 149.

[174] J. A. Pople, J. S. Binkley, R. Seeger, Int. J. Quant. Chem., 1976, 10, 1.

[175] R. Krishnan, J. A. Pople, Int. J. Quant. Chem., 1978, 14, 91.

[176] R. Krishnan, J. A. Pople, E. S. Replogle, M. Head-Gordon, J. Phys. Chem. 1990, 94, 5579.

[177] T. H. Dunning, J. Chem. Phys., 1989, 90, 1007.

[178] W. J. Hehre, L. Radom, P. V. R. Schleyer and J. A. Pople, Ab Initio molecular orbital Theory, Wiley, New York, 1986.

[179] R. F. W. Bader, Atoms in molecules, Oxford, New York, 1990.

[180] P. Hohenburg and W. Kohn, Phys. Rev., 1964, 136B, 864.

[181] W. Kohn and L. J. Sham, Phys. Rev., 1965, 140, A1133.

[182] A. D. Becke, J. Chem. Phys., 2014, 140, 18A301.

[183] P. R. T. Schipper, O. V. Gritsenko, S. J. A. van Gisbergen, E. J. Baerends, J. Chem. Phys., 2000, 112, 1344.

[184] D. Cremer, Mol. Phys., 2001, 99, 1899.

[185] J. Li, L. Noodleman, D. A. Case, E. I. Solomon, A. B. P. Lever (Eds.), Inorganic Electronic Structure and Spectroscopy, John Wiley & Sons Inc., New York, 1999.

[186] J. Tomasi, B. Mennucci, R. Cammi, Chem. Rev., 2005, 105, 2999.

[187] F. Jensen in Introduction to computational chemistry. John Wiley & Sons, New York, 2007.

[188]   A. Warshel, M. Levitt, J. Mol. Biol., 1976, 103, 227.

[189]   J. W. Ponder, C. Wu, P. Ren, V. S. Pande, J. D. Chodera, M. J. Schnieders, I. Haque, D. L. Mobley, D. S. Lambrecht, R. A. DiStasio, Jr., M. Head-Gordon, G. N. I. Clark, M. E. Johnson, T. Head-Gordon, J. Phys. Chem. B, 2010, 114, 2549.

[190]   G. Monard. J. L. Rivail, in Handbook of Computational Chemistry, J. Leszczynski (Ed.), Solvent Effects in Quantum Chemistry, Springer, Netherlands, 2012, pp. 561-571.

[191]   H. Hu, W. Yang, J. Mol. Struct. THEOCHEM, (2009). 898, 17.

[192]   S.C.L. Kamerlin, M. Haranczyk, A. Warshel, ChemPhysChem., 2009, 10, 1125.

[193]   T. Kerdcharoen, K. Morokuma, Chem. Phys. Lett., 2002, 355, 257.

[194]   T. Kerdcharoen, K. Morokuma, J. Chem. Phys, 2003, 118, 8856.

[195]   R. Skyner, J. L. McDonagh, C. R. Groom, T. van Mourik, J. B. O. Mitchell, Phys. Chem. Chem. Phys., 2015, 17, 6174.

[196]   B. Roux, T. Simonson, Biophys. Chem., 1999, 78, 1.

[197]   B. Lee, F.M. Richards, J. Mol. Biol., 1971, 55, 379.

[198]   F. Fogolari, A. Brigo, H. Molinari, J. Mol. Recognit., 2002, 15, 379.

[199]   A. Onufriev, D. Bashford, D. A. Case, J. Comp. Chem., 2002, 23, 1297.

[200]   A. Ben-Naim, Y. J. Marcus, Chem. Phys., 1984, 81, 2016.

[201]   V. Barone, M. Cossi, J. Tomasi, J. Chem. Phys., 1997, 107, 3210.

[202]   R. C. Weast, in Handbook of Chemistry and Physics, Cleveland, OH, 1981.

[203]   A. Bondi, J. Chem. Phys. 1964, 68, 441.

[204]   J. D. Thompson, C. J. Cramer, D. G. Truhlar, J. Phys. Chem. A, 2004, 108, 6532.

[205]   L. Rohschneider, Anal. Chem. 1973, 45, 1241.

[206]   J. R. Pliego Jr., J. M. Riveros, Phys. Chem. Chem. Phys., 2002, 4, 1622.

[207]   Y. Takano, K. N. Houk, J. Chem. Theory Comput., 2005, 1, 70.

[208]   B. Mennucci, R. Cammi, in Continuum Solvation Models in Chemical Physics: From Theory to Applications, John Wiley & Sons, Chichester, 2007.

[209]   Gaussian 09, Revision D.01, M. J. Frisch, G. W. Trucks, H. B. Schlegel, G. E. Scuseria, M. A. Robb, J. R. Cheeseman, G. Scalmani, V. Barone, B. Mennucci, G. A. Petersson, H. Nakatsuji, M. Caricato, X. Li, H. P. Hratchian, A. F. Izmaylov, J. Bloino, G. Zheng, J. L. Sonnenberg, M. Hada, M. Ehara, K. Toyota, R. Fukuda, J. Hasegawa, M. Ishida, T. Nakajima, Y. Honda, O. Kitao, H. Nakai, T. Vreven, J. A. Montgomery, Jr., J. E. Peralta,

F. Ogliaro, M. Bearpark, J. J. Heyd, E. Brothers, K. N. Kudin, V. N. Staroverov, R. Kobayashi, J. Normand, K. Raghavachari, A. Rendell, J. C. Burant, S. S. Iyengar, J. Tomasi, M. Cossi, N. Rega, J. M. Millam, M. Klene, J. E. Knox, J. B. Cross, V. Bakken, C. Adamo, J. Jaramillo, R. Gomperts, R. E. Stratmann, O. Yazyev, A. J. Austin, R. Cammi, C. Pomelli, J. W. Ochterski, R. L. Martin, K. Morokuma, V. G. Zakrzewski, G. A. Voth, P. Salvador, J. J. Dannenberg, S. Dapprich, A. D. Daniels, Ö. Farkas, J. B. Foresman, J. V. Ortiz, J. Cioslowski, and D. J. Fox, Gaussian, Inc., Wallingford CT, 2009.

[210]   T. Helgaker, P. Jørgensen, J. Olsen, in Molecular Electronic-Structure Theory, John Wiley & Sons, New York, 2000.

[211]   T. H. Dunning Jr., J. Chem. Phys., 1989, 90, 1007.

[212]   R. A. Kendall, T. H. Dunning Jr., R. J. Harrison, J. Chem. Phys., 1992, 96, 6796.

[213]   D. E. Woon, T. H. Dunning Jr., J. Chem. Phys., 1993, 98, 1358.

[214]   D. E. Woon, T. H. Dunning Jr., J. Chem. Phys., 1994, 100, 2975.

[215]   D. G. Truhlar, Chem. Phys. Lett., 1998, 294, 45.

[216]   A. Halkier, T. Helgaker, P. Jørgensen, W. Klopper, H. Koch, J. Olsen, A. K. Wilson, Chem. Phys. Lett., 1998, 286, 243.

[217]   K. K. Irikura, in Essential Statistical Thermodynamics in Computational Thermochemistry. Prediction and Estimation of Molecular Thermodynamics, edited by K. K. Irikura and D. J. Frurip, American Chemical Society, Washington, DC, 1998, p 402.

[218]   M. J. Frisch, A. B. Nielsen, A. J. Holder, Gauss View Users Manual, Gaussian Inc., Pittsburgh, PA, 2000.

[219]   http://www.chemcraftprog.com.

[220]   K. A. Holbrook, M. J. Pilling, and S. H. Robertson, Unimolecular reactions, second edition, Wiley, Chichester, 1996.

[221]   N. A. Pradie, H. V. Linnert, SuperRRKM, version 1.0, University of São Paulo, São Paulo, Brazil, 2009.

[222]   T. Beyer, D. F. Swinehart, Commun. Assoc., 1973, 16, 379.

[223]   S. E. Stein, B. S. Rabinovitch, J. Chem. Phys., 1973, 58, 2438.

[224]   W. H. Press, B. P. Flannery, S. A. Teoukolsky, W. T. Vetterling, Numerical Recipes – The Art of Scientific Computing, Cambridge University Press, 1990.

[225] J. Xie, J. Zhang, W. L. Hase, Int. J. Mass Spectrom., 2015, 378, 14.

[226] J. Liu, Z. Geng, Y. Wang, D. Wang, Y. Liu, Comp. Theor. Chem., 2013, 1012, 27.

[227] S. J. Gronert, Am. Chem. Soc., 1991, 113, 6041.

[228] G. N. Merrill, S. Gronert, S. R. Kass, J. Phys. Chem. A, 1997, 101, 208.

[229] A. P. Bento, M. Solà, F. M. Bickelhaupt, J. Chem. Theory Comput., 2008, 4, 929.

[230] A. Pabis, P. Paluch, J. Szala, P. Paneth, J. Chem. Theory Comput., 2009, 5, 33.

[231] Y. Zhao, D. G. Truhlar, J. Chem. Theory Comput., 2010, 6, 1104.

[232] P. Manikandan, J. Zhang, W. L. Hase, J. Phys. Chem. A, 2012, 116, 3061.

[233] Y. G. Proenza, M. A. F. de Souza, E. Ventura, S. A. do Monte, R. L. Longo, Phys. Chem. Chem. Phys., 2014, 16, 26769.

[234] M. Bodenbinder, S. E. Ulic, H. Willner, J. Phys. Chem., 1994, 98, 6441.

[235] P. Maksyutenko, L. G. Muzangwa, B. M. Jones, R. I. Kaiser, Phys. Chem. Chem. Phys., 2015, 17, 7514.

[236] P. D. Mallinson, J. Mol. Spectr., 1975, 55, 94.

[237] M.N. Glukhovtsev, A. Pross, L. Radom, J. Am. Chem. Soc. 1996, 118, 6273.

[238] M. L. Chabinyc, S. L. Craig, C. K. Regan, J. I. Brauman, Science, 1998, 279, 1882.

[239] G. S. Hammond, J. Am. Chem. Soc., 1955, 77, 334.

[240] R. P. Bell, Proc. R. Soc. London, Ser. A, 1936, 154, 414.

[241] M. G. Evans, M. Polanyi, J. Chem. Soc., Faraday Trans., 1936, 32, 1333.

[242] E. V. Anslyn, D. A. Dougherty, in Modern Physical Organic Chemistry, University Science, Sausalito, CA, 2006.

[243] J. E. House, Inorganic chemistry, Academic Press, New York, 2008, p. 130.

[244] E. R. Lovejoy, S. K. Kim, C. B. Moore, Science, 1992, 256, 1541.

[245] S. I. Ionov, H. F. Davis, K. Mikhaylichenko, L. Lalachovic, R. A. Beaudet, C. Wittig, J. Chem. Phys., 1994, 109, 4809.

[246] G. H. Leu, C. L. Huang, S. H. Lee, Y. C. Lee and I. C. Chen, J. Chem. Phys., 1998, 109, 9340.

[247] I. W. M. Smith, Nature, 1992, 358, 279.

[248] R. Marcus, Science, 1992, 256, 1523.

[249] V. M. Bierbaum, C. H. DePuy, R. H. Shapiro, J. H. Stewart, J. Am. Chem. Soc., 1976, 98, 4229.

[250] F. Weinhold, C. R. Landis, Discovering chemistry with natural bond orbitals, John Wiley & Sons, New Jersey, 2012.

[251] N. Kornblum, R. A. Brown, J. Am. Chem. Soc., 1964, 86, 2681.

[252] K. W. Wiitala, T. R. Hoye, C. J. Cramer, Chem. Theory. Comput., 2006, 2 , 1085.

[253] P. H.-Y. Cheong, C. Y. Legault, J. M. Um, N. Çelebi-Ölçüm, K. N. Houk, Chem. Rev., 2011, 111, 5042.

[254] G. Jindal, H. K. Kisan, Raghavan B. Sunoj, ACS Catalysis, 2015, 5, 480.

[255] A. Mahmood, E. S. Teixeira, R. L. Longo, J. Org. Chem., 2015, 80, 8198.

[256] L. Goerigk, S. Grimme, Phys. Chem. Chem. Phys., 2011, 13, 6670

[257] T. Schwabe, S. Grimme, Phys. Chem. Chem. Phys. 2006, 8, 4398

[258] S. Grimme, J. Chem. Phys. 2006, 124, 034108.

[259] A. Karton, A. Tarnopolsky, J.-F. Lamère, G. C. Schatz, J. M. L. Martin, J. Phys. Chem. A 2008, 112, 12868.

[260] A. D. Becke, J. Chem. Phys. 1993, 98, 5648.

[261] C. Lee, W. Yang, R. G. Parr, Phys Rev. B 1988, 37, 785

[262] A. J. Cohen, P. Mori-Sánchez, W. Yang, Chem. Rev., 2012,112, 289

[263] B. S. Jursic, J. Mol. Str. (Theochem), I997, 417, 89.

[264] B. S. Jursic, J. Mol. Str. (Theochem) 2000, 497, 65.

[265] Y. Ren, J. L. Wolk, S. Hoz, Int. J. Mass Spectrom., 2003, 225, 167.

[266] Y. Ren, J. L. Wolk, S. Hoz, Int. J. Mass Spectrom., 2002, 221, 59.

[267] P. Kolandaivel, D. U. Maheswari, L. Senthilkumar, Comp. Theor. Chem., 2013, 1004, 56.

[268] Q. S. Li, X. D. Xu, S. Zhang, Chem. Phys. Lett., 2004, 384, 20.

[269] X. Xu, D. G. Truhlar, J. Chem. Theory Comput. 2012, 8, 80.

[270] J. A. Pople, M. Head-Gordon, D. J. Fox, K. Raghavachari, L. A. Curtiss, J. Chem. Phys., 1989, 90, 5622.

[271] L. A. Curtiss, K. Raghavachari, P. C. Redfern, J. A. Pople, J. Chem. Phys., 1997, 106, 1063.

[272] L. A. Curtiss, K. Raghavachari, P. C. Redfern, J. A. Pople,J. Chem. Phys., 2000, 112, 7374.

[273] L. A. Curtiss, P. C. Redfern, K. Raghavachari, J. Chem. Phys., 2005, 123, 124107.

[274]   B. J. Lynch, D. G. Truhlar, J. Phys. Chem. A, 2003, 107, 8996.

[275]   Y. Zhao, D. G. Truhlar, J. Phys. Chem. A, 2006, 110, 10478.

[276]   Y. Zhao, D. G. Truhlar, J. Phys. Chem. C, 2008, 112, 6860.

[277]   Y. Zhao, D. G. Truhlar, Theor. Chem. Acc., 2008, 120, 215.

[278]   Y. Zhao, D. G. Truhlar, J. Chem. Theor. Comput., 2009, 5, 324.

[279]   U. Lourderaj, W. L. Hase, J. Phys. Chem. A, 2009, 113, 2236.

[280]   L. M. M. Quijano, D. A. Singleton, J. Am. Chem. Soc., 2011, 133, 13824.

[281]   M. Paranjothy, R. Sun, Y. Zhuang, W. L. Hase, J. Comput. Mol. Sci., 2013, 3, 296.

[282]   T. C. Correra, J. M. Riveros, J. Phys. Chem. A, 2010, 114, 11910.

[283]   J. Rehbein, B. K. Carpenter, Phys. Chem. Chem. Phys., 2011, 13, 20906.

[284]   J. M. Bowman, B. C. Shepler, Annu. Rev. Phys. Chem., 2011, 62, 531.

[285]   B. K. Carpenter, Chem. Rev., 2013, 113, 7265.

[286]   A. Halkier, T. Helgaker, P. Jorgensen, W. Klopper, H. Koch, J. Olsen, A. K. Wilson, Chem. Phys. Lett., 1998, 286, 243.

[287]   K. Raghavachari, G. W. Trucks, J. A. Pople, M. Head-Gordon, Chem. Phys. Lett. 1989, 157, 479.

[288]   T. H. Dunning Jr., P. J. Hay, H. F. Schaefer III (Ed.), Modern Theoretical Chemistry, vol. 3 Plenum, New York (1976), pp. 1–28.

[289]   P. J. Hay, W. R. Wadt J. Chem. Phys., 82 (1985), pp. 270–283.

[290]   K. Fukui, Acc. Chem. Res., 1981, 14, 363.

[291]   D. G. Truhlar, Chem. Phys. Lett., 1998, 294.

[292]   S. B. Huh, J. S. Lee, J. Chem. Phys., 2003, 118, 3035.

[293]   G. W. Snedecor, W. G. Cochran, Statistical Methods, Iowa State University Press., Ames, 1989.

[294]   Y. Zhao, N. G. García, D. G. Truhlar, J. Phys. Chem. A, 2005, 109, 2012.

[295]   A. P. Bento, M. Solá, F. M. Bickelhaupt, J. Chem. Theory Comput., 2008, 4, 929.

[296]   M. Swart, M. Solá, F. M. Bickelhaupt, J. Chem. Theory Comput., 2010, 6, 3145.

[297]   Y. Zhao, D. G. Truhlar, J. Chem. Theory Comput., 2010, 6, 1104.

Appendix A: Supplementary Results

Table A1. Experimental and calculated (unscaled) vibrational frequencies for CH_3NO_2 at different theoretical levels.

Exp[a]	Exp[b]	MP2[c]			B2PLYP[c]		mPW2PLYP[c]	
		LAN	DZ	TZ	LAN	DZ	LAN	DZ
475		484.80	478.78	480.76	480.24	476.36	485.73	480.80
603		591.36	594.77	603.97	597.49	600.77	605.52	608.81
657	663	665.55	667.66	672.83	658.63	658.85	666.87	667.19
918		937.69	938.32	940.64	922.63	923.26	935.84	936.72
1096	1106	1152.78	1116.35	1127.82	1134.72	1110.23	1144.01	1117.79
1131		1166.91	1132.80	1147.62	1157.56	1132.55	1166.41	1140.83
1380	1378	1423.71	1405.08	1411.47	1406.16	1395.42	1431.71	1409.60
1397		1464.68	1420.52	1430.60	1451.26	1415.50	1460.85	1435.40
1410		1519.07	1465.55	1492.24	1503.42	1454.51	1510.72	1461.42
1434	1423	1524.27	1475.70	1500.87	1514.16	1467.86	1521.28	1475.24
1583	1572	1783.73	1760.34	1744.17	1629.54	1617.01	1656.51	1642.42
2974	2963	3141.69	3112.48	3115.74	3128.74	3101.38	3139.31	3115.67
3045	3041	3250.68	3225.68	3222.68	3227.49	3205.23	3237.97	3219.24
3080	3073	3276.36	3253.62	3249.35	3256.56	3235.61	3267.61	3250.59

[a] M. Bodenbinder , S. E. Ulic , H. Willner J. Phys. Chem., 1994, 98, 6441. [b] P. Mutenko, L. G. Muzangw, B. M. Jones, R. I. Kaiser, Phys. Chem. Chem. Phys., 2015, 17, 7514. [c] LAN = LanL2DZ, DZ = aug-cc-pVDZ, TZ = aug-cc-pVTZ

Table A2. Experimental and computed enthalpy of deprotonation of nitroalkanes, $R_1R_2CHNO_2(g) \rightarrow [R_1R_2CNO_2]^-(g) + H^+(g)$ at 298 K using different theoretical levels. All values in kJ/mol.

Nitroalkane	Exp	MP2[a]		B2PLYP[a]		mPW2PLYP[a]	
		LAN	DZ	LAN	DZ	LAN	DZ
$[H_2CHNO_2]$	1491	1479.3	1485.0	1475.2	1475.2	1473.6	1474.0
$[CH_3CH_2NO_2]$	1489	1477.2	1481.3	1474.4	1475.3	1473.0	1474.5
$[(CH_3)_2CHNO_2]$	1490	1478.0	1481.7	1476.1	1476.4	1475.1	1475.8
$[c\text{-}(CH_2)_2CHNO_2]$	1534	1506.9	1509.8	1502.2	1503.8	1502.5	1504.4

[a] LAN = LanL2DZ, DZ = aug-cc-pVDZ.

Table A3. C–I bond distance (Å) calculated at different theoretical levels

| Bond	Exp[b]	MP2[a]			B2PLYP[a]		mPW2PLYP[a]	
		LAN	DZ	TZ	LAN	DZ	LAN	DZ
C–I	2.136	2.142	2.149	2.117	2.153	2.166	2.149	2.162

[a] LAN = LanL2DZ, DZ = aug-cc-pVDZ-pp, TZ=aug-cc-pVTZ-pp

[b] P. D. Mallinson, J. Mol. Spectr., 1975, 55, 94.

Table A4. The product distribution for each pathway of $[R_1R_2CNO_2]^- + CH_3I$ S_N2 reactions at different available energies in the RRKM calculations. E is the minimum available energy and $(E + E_T)$, where E_T is the classical thermal energy, that is, $E_T = N_{at}\times(3/2)RT$ with N_{at} being the number of atoms.[a]

Product ratio	MP2/DZ		MP2/TZ		MP2/QZ		CBS (D,T)	
	$k_{34}=k_{43}=0$	$k_{34}\cong k_{43}$	$k_{34}=k_{43}=0$	$k_{34}\cong k_{43}$	$k_{34}=k_{43}=0$	$k_{34}\cong k_{43}$	$k_{34}=k_{43}=0$	$k_{34}\cong k_{43}$
$S_N2@C1 : S_N2@O1$	53:47	96:04	58:42	96:04	60:40	95:05	65:35	100:0
$S_N2@C2 : S_N2@O2$ (Z)	71:29	100:0	60:40	99:01	62:38	98:02	65:35	100:0
$S_N2@C2 : S_N2@O2$ (E)	56:44	99:01	67:33	99:01	69:31	98:02	74:26	100:0
$S_N2@C3 : S_N2@O3$	66:34	100:0	89:09	100:0	89:06	100:0	95:05	100:0
$S_N2@C4 : S_N2@O4$	90:10	100:0	96:03	100:0	97:03	100:0	98:02	100:0

[a] DZ = aug-cc-pVDZ, TZ = aug-cc-pVTZ, QZ = aug-cc-pVQZ
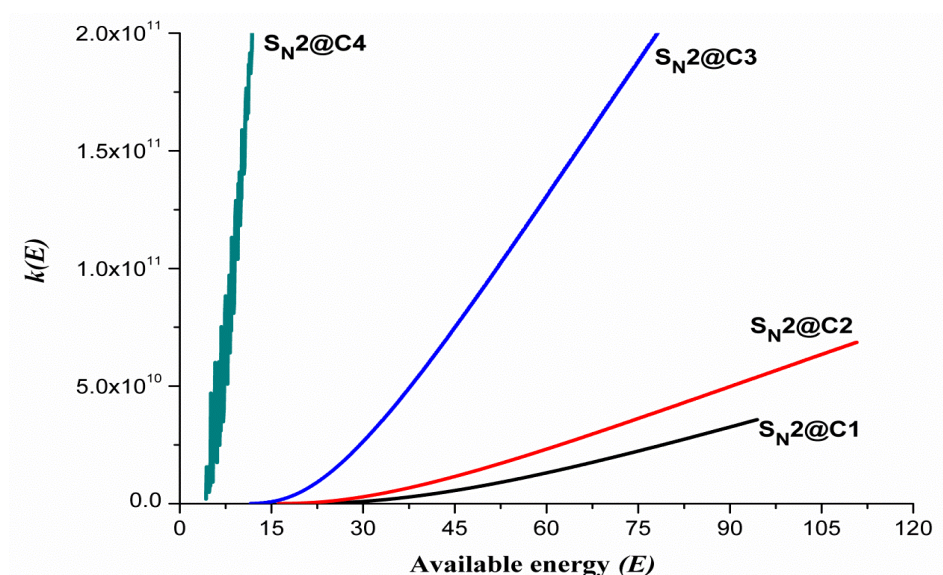
Figure A1. Microcanonical rate constants k (s^{-1}) for the C-methalylation (S$_N$2@C) of deprotonated nitromethane (**1**), nitroethane (**2**), 2-nitropropane (**3**), nitrocyclopropane (**4**) by iodomethane (CH$_3$I) calculated using the RRKM theory as a function of the at available energy $E = E_0 + E_T$ (in kJ/mol) to the reactant complexes. Quantum chemical calculations at the MP2/CBS//MP2/aug-cc-pVDZ.
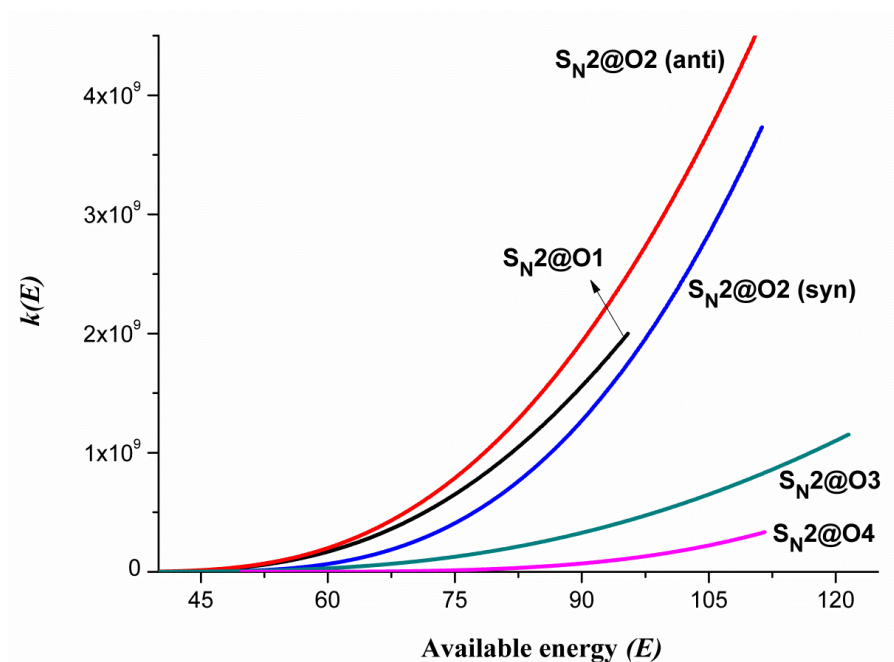
**Figure A2.** Same as Figure A1 for the O-methalylation (S$_N$2@O).
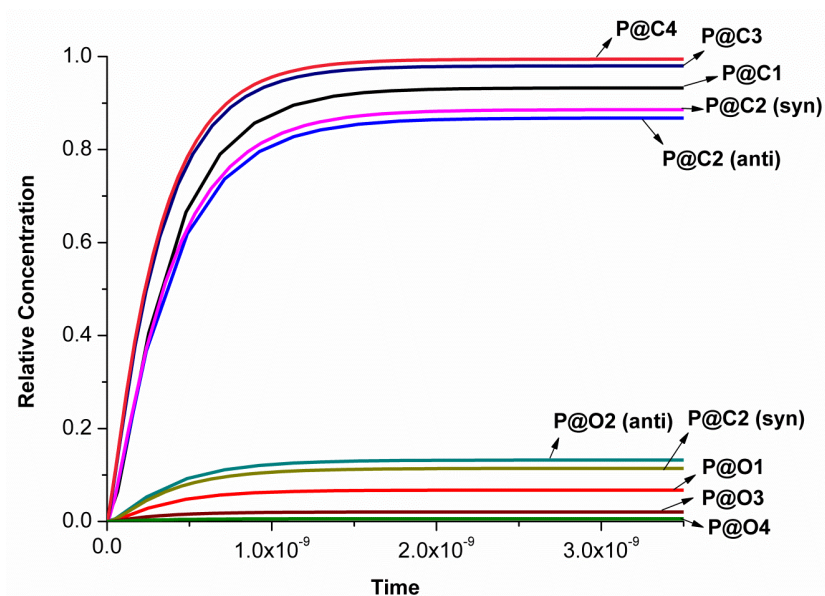
Figure A3. Relative concentration of the products of alkylnitronates with iodomethane at the minimum available energy (E) plus half of the classical thermal energy ($\frac{1}{2} \times N \times 3/2RT$ with N being the number of atoms). Quantum chemical calculations at MP2/aug-cc-pVDZ.
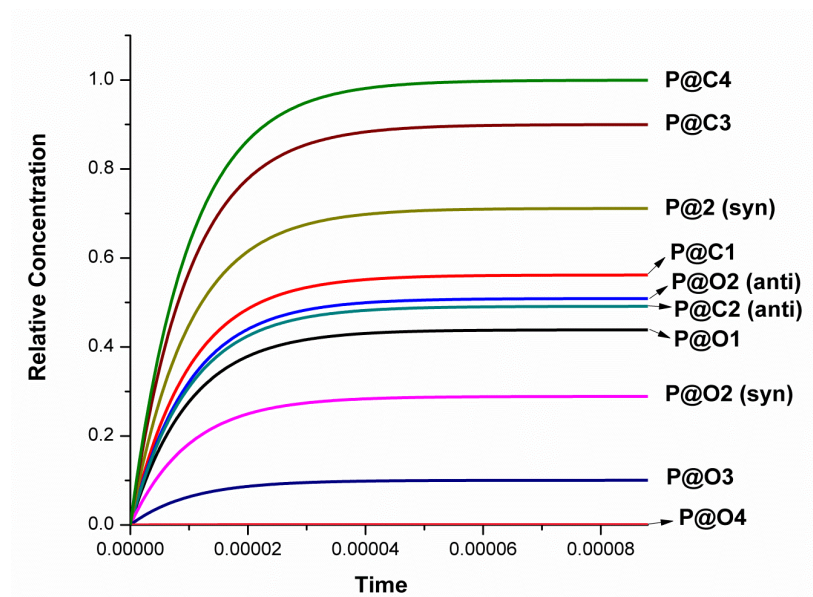
Figure A4. Relative concentration of the products of alkylnitronates with iodomethane at the minimum available energy (E) plus the classical thermal energy ($N \times 3/2RT$ with N being the number of atoms). Quantum chemical calculations at MP2/aug-cc-pVDZ.
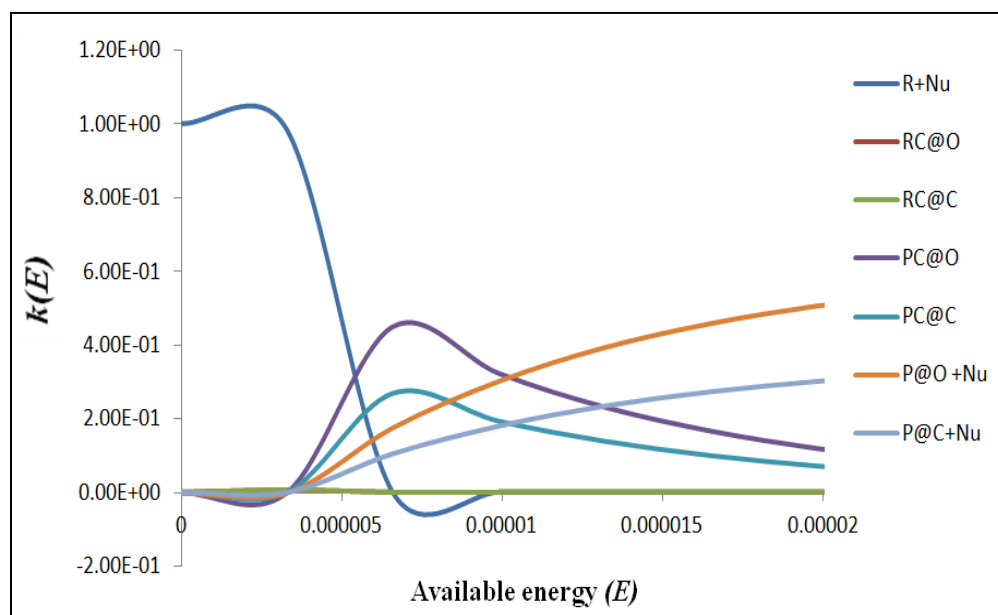
Figure A5. Temporal evolution of concentration of reactants, intermediates and the products for reaction **2** (*anti*) at $E + E_T$.